Fall 2010

Slowing and switching of light in semiconductor quantum wells

Murat Yildirim
University of Iowa

SLOWING AND SWITCHING OF LIGHT IN SEMICONDUCTOR QUANTUM WELLS

by
Murat Yildirim

An Abstract

Of a thesis submitted in partial fulfillment
of the requirements for the Doctor of
Philosophy degree in Physics in
the Graduate College of
The University of Iowa

December 2010

Thesis Supervisor: Professor John Prineas

ABSTRACT

After light became a part of the telecommunication system, the manipulation of light, especially the control of the speed of light, became a focus of research. By using the different approaches of the interaction between light and matter, there have been many successful attempts to slow down the speed of light, even to several meters per second. In the first part of my thesis, I studied pulse propagation in absorptive media (GaAs/AlGaAs multiple quantum well structures-MQWs) to gain insight into the linear interaction between matter and light. Systematic and fundamental measurements of pulse propagation in GaAs/AlGaAs multiple quantum well structures will be presented. These measurements are simulated by treating MQWs as a slab. These measurements and simulations will be compared while using a newly introduced general formalism.

In the second part of my thesis, I will present another aspect of manipulating light: all–optical switching. Eric Gansen demonstrated all-optical switching in GaAs/AlGaAs MQWs at cryogenic temperatures. I will demonstrate that the same design of all-optical switch, which is based on polarized virtual carriers, can work without any serious loss of performance at near-room temperatures.

Another material used in all-optical switches is Bragg-spaced-quantum-well structures (BSQWs) which are grown by molecular beam epitaxy. The growth of BSQW is challenging because of the associated unusually long growth times. In the last part of this dissertation, I will discuss the challenges involved in MBE growth of 210 period long GaAs/InGaAs BSQWs. By presenting basic characterization measurements of the

successful and unsuccessful attempts of BSQW growths, I will demonstrate the challenges of BSQW growth and how they can be addressed.

Abstract Approved: _____
Thesis Supervisor

_____
Title and Department

_____
Date

SLOWING AND SWITCHING OF LIGHT IN SEMICONDUCTOR QUANTUM WELLS

by
Murat Yildirim

A thesis submitted in partial fulfillment
of the requirements for the Doctor of
Philosophy degree in Physics in
the Graduate College of
The University of Iowa

December 2010

Thesis Supervisor: Professor John Prineas

Graduate College
The University of Iowa
Iowa City, Iowa

CERTIFICATE OF APPROVAL

PH.D. THESIS

This is to certify that the Ph.D. thesis of

Murat Yildirim

has been approved by the Examining Committee for the thesis requirement
for the Doctor of Philosophy degree in Physics at the December 2010 graduation.

Thesis Committee: _____
John P. Prineas, Thesis Supervisor

_____
Thomas F. Boggess

_____
Craig Pryor

_____
David R. Andersen

_____
Christopher M. Cheatum

To Sabahat, Yagmur Ela, and Eymen.

TABLE OF CONTENTS

LIST OF FIGURES

CHAPTER 1: INTRODUCTION

Today, most of the world's long-distance voice and data traffic is carried over optical-fiber cables as optical signals. There are two significant reasons for why fiber optic cables are replacing old copper wires: attenuation and bandwidth. The most advanced coaxial cable system was put into use in mid 70's and was capable of a bandwidth of 274 Mb/s, but the repeater separation of these cables was only a kilometer [1]. Therefore the price of high-speed coaxial copper cables is the need to regenerate or strengthen the signal every kilometer which makes the system expensive to operate [1]. On the other hand, there are commercially available fiber optic cables with bandwidths of 2.5 Gb/s – 10 Gb/s, and it is possible to design fiber cables without repeaters for more than 100 kilometers [2]. Technologies like wavelength-division multiplexing (WDM) can further increase the rate of data transfer in fiber-optic cables. WDM is a technology enabling the transmission of multiple optical signals by using different colors (wavelengths) of light on a single fiber. Modern WDM systems can acquire a bandwidth of more than 1 Tb/s [1,2].

On the other hand, fiber-optic communication systems are not all-optical yet. They still rely on electronic components. Every time an optical signal needs to be processed or rerouted, it must first be converted from an optical to an electrical signal. After conversion and processing, the electrical signals are converted back to optical signals. These O-E-O (optical-electrical-optical) conversions are required at every connection point, or node, due to a lack of optical counterparts to the electronic processors or routers. Eliminating these conversions will reduce the number of electronic

parts in the communication system resulting in potential lower costs and faster communication.

Subluminal propagation of light pulses is one of the research foci addressing these needs of the fiber-optic communication systems [3]. Continuously tunable delay lines and optical buffers are potential applications of these studies [4,5,6]. An optical buffer is a key component needed to store optical signals when two optical data packets arrive at the same time, as in Fig. 1.1a, or in the case that a data packet arrives when the processor is still busy. It stores or delays a packet of data containing thousands of bits (1 bit = temporal width of an optical pulse) until the processor is ready again.

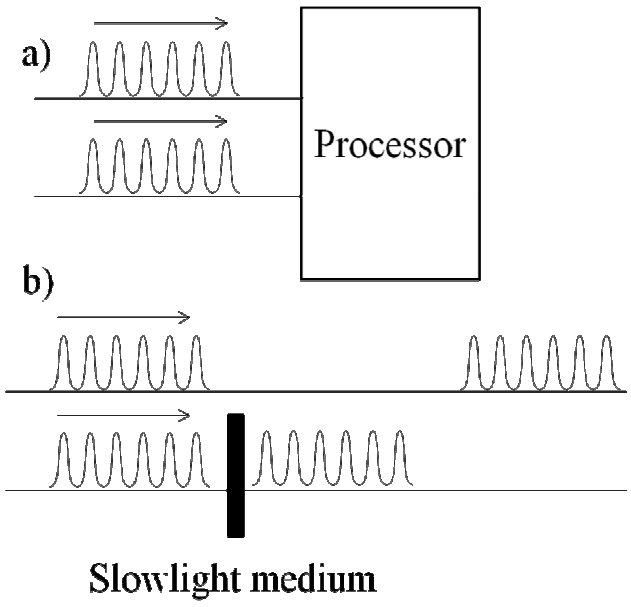

Figure 1.1 Schematic of a slow light medium delays a packet of data. a) When two data packets arrive at a processor, one needs to be either delayed or stopped and stored. b) A tunable slow light medium with high index can increase system performance.

A slow light medium is defined as a medium with a very large group index compared to the index of refraction, and it can be continuously tunable without moving mechanical parts [7,8] as shown in Fig. 1.1b. Therefore, slow light media are natural candidates for optical buffers and delay lines. Various methods have been used to obtain ultraslow group velocities in slow light media: Electromagnetically induced transparency [5,9-13] coherent population oscillations [14-18], stimulated Brillouin scattering [19-21], stimulated Raman scattering [22-24], etc.

At the same time, the theoretical investigation of a wave packet's propagation in a resonant medium is a classical text book problem [25]. Sommerfeld and Brillouin addressed pulse propagation in absorptive medium which can be marked as the starting point of the slow light studies nearly a century ago [26]. An extensive amount of theoretical work has been done on the subject after Sommerfeld and Brillouin [27-37]. These studies [27-33] focused on determining the propagation speed of the wave packet's envelope and when the group velocity is a valid way to describe the speed of the envelope through a resonant medium. In later theoretical work, superluminal propagation (fast-light) of the envelope and the meaning of superluminal propagation in terms of data transfer has been discussed [34-37].

Studying light propagation near a strong absorption resonance and related index change is a basic way to test theoretical work. However, because of strong absorption the experimental investigation of a wave packet's propagation through a medium near resonance has become possible only with the invention of lasers. There are two famous experimental studies of pulse propagation near a strong absorption resonance in semiconductors. First, the wave propagation near the 1s exciton resonance in bulk

gallium arsenide (GaAs) has been investigated by Ulbrich and Fehrenbach [38]. When they tuned over the resonance, they observed only subluminal propagation (slow light). Later, Chu and Wong [39] studied a different semiconductor, nitrogen-doped gallium phosphide (GaP:N), performing similar experiments. Chu et. al. observed a considerable amount of superluminal propagation (fast light) in addition to subluminal propagation in contrast to Ulbrich and Fehrenbach.

In a more recent study [40], Sarkar et al. studied pulse propagation near GaAs/AlGaAs multiple quantum well (MQW) absorption resonance. For GaAs/AlGaAs MQW structures, Sarkar et al. tuned the probe pulse over the absorption resonance of the GaAs/AlGaAs MQWs and measured the time delay and group velocity. A 2-bit delay was observed. Similar to Ulbrich et. al and in contrast to the results of Chu [39] et. al, they observed very little superluminal propagation when compared to subluminal propagation[40,41].

In chapter 2, some concepts related to light propagation in absorptive media, such as dispersion and group velocity, will be discussed. Also a discussion of Lorentz oscillator model is included to simply describe light-matter interaction. The experimental studies [38-41] will be revisited again to compare and contrast them to the theoretical work. In Chapter 3, pulse propagation near absorption resonance of GaAs/AlGaAs MQW structures will be studied and discussed for the following reasons. First, the problem of wave packet propagation near an absorption resonance has the fundamental importance. Second, there is a dearth of experimental studies near single absorption resonances in semiconductors such as GaAs/AlGaAs MQW structures.

Similar to optical buffers and delay lines, fast all-optical switches can reduce the need for O-E-O conversions. MQW structures can also be implemented as switching materials [42-45] in all-optical switching schemes. These optical switches may be sufficiently compact to be integrated with current fiber-optic technology. An application for an optical switch can be found in WDM schemes. The switch can act as a temporal filter for long pulses in time. By cross-correlating the long signal pulse with a temporally short control pulse, one can acquire a copy of the signal stream with the same bit rate and shorter individual bits. In Chapter 4, a previously demonstrated all-optical switch in our group will be discussed. The virtues of virtual (near, but below resonant) excitation over resonant excitation will also be reviewed. In Chapter 5, we will look for ways to improve the all-optical switch based on virtual excitation of spin-polarized carrier population.

The quantum well resonance is a source not only of the large spectral dispersion needed for slowing light, but also of unwanted absorption which causes pulse attenuation and distortion. Stacking MQWs with Bragg periodicity presents us with a rather interesting option to change linear and nonlinear properties quantum wells e.g. occurrence of photonic bandgap, increasing the reflection etc. By using these properties, there are schemes proposed for stopping, storing, and releasing light pulses using Bragg-spaced quantum well (BSQW) structures [46,47]. At the same time BSQW's have the potential of producing tunable slow light delays by changing the detuning between Bragg and 1s hh (heavy hole) exciton frequency [48].

However, relatively few experimental studies have been conducted with BSQW structures. One reason for the lack of experimental work is that BSQW structures are very challenging to fabricate. In Chapter 6, first, we will introduce the molecular beam

epitaxial (MBE) growth technique and BSQW structures. Then, we will discuss the challenges of MBE growth of BSQW structures. Lastly, some of the experimental and theoretical studies of BSQW structures will be discussed [44,46-50].

Lastly, this work will be concluded by suggesting ways to continue and improve this study in Chapter 7.

CHAPTER 2: OVERVIEW FOR PULSE PROPAGATION IN ABSORPTIVE MEDIA

2.1 Background and important concepts about pulse propagation in absorptive media

Some of the important concepts required to understand light propagation in absorptive media, such as dispersion and group velocity, will be discussed in this chapter. Since the 1s exciton heavy hole (hh) absorptive resonance can be approximated as a Lorentz oscillator, a brief discussion of the Lorentz oscillator model is included to help acquire a basic picture of light-matter interaction. Some of the basic concepts of multiple quantum wells (MQWs) will be discussed to identify the material employed to conduct measurements of wave-packet propagation in highly-absorptive media. The hh absorption resonance and other basics of semiconductors are discussed in Appendix A.

2.1.1 Dispersion, dispersion relation, phase and group velocity

Dispersion can be defined as the variation of the speed of a wave in a medium with its frequency. Dispersion occurs due to the frequency dependent response of the medium. A familiar example is that of white light passing through a prism. The speed for waves of red light is greater than that of blue light inside the prism. As the light enters the prism from the air, the refraction, governed by Snell's law ($\sin i / \sin r = n = c / v$), dictates that the angle of refraction will be different for red and blue light waves, where i is angle of incidence, r is angle of refraction, c is the speed of light in air, and v is the speed of light inside the prism. They will therefore become spatially separated. If, in a certain medium, the velocity of the wave depends on the frequency of the wave, then the medium is called *dispersive*. If the refractive index of the medium decreases with

increasing wavelength λ, the medium is said to have *normal dispersion*. On the other hand, if the index increases with increasing wavelength, the medium has *anomalous dispersion*. It is common to refer to the dependence of frequency (ω) on wave number (k) as the *dispersion relation*.

For a monochromatic, harmonic, plane wave of the form $y = A\cos(\omega t - kx)$, *phase velocity* refers to the velocity that any given phase or feature of the wave (for example, the crest) will travel. It is defined as $v = \lambda/T$ or $v = \omega/k$ where λ is the wavelength, T is the period, ω is the circular frequency and k is the wave number. The specific relation between ω and k determines the phase velocity of the wave. When a wave or a pulse travels through a medium, its phase velocity will be equal to the velocity of light in vacuum (c) divided by the index of refraction of the medium (n), namely $v = c/n$.

For a wave packet (e.g. superimposed sinusoidal waves of different frequencies) in a dispersive medium, each frequency will travel with its own phase velocity which may or may not be the same as the other frequencies. In a vacuum (the only truly non-dispersive medium) $v = \omega/k$ will be equal to velocity of light in vacuum (c) for all frequencies. In most cases, "the velocity of light" refers to the phase velocity.

The velocity of the envelope consisting of different frequencies of the wave packet is called *the group velocity*. For a pulse with a frequency spectrum centered around a central frequency $\omega_0 (= ck_0)$, and propagating through a source-free, nonconductive medium, the group velocity of the wave packet defined as:

$$v_g^{-1} = \left(\frac{\partial \mathrm{Re}(k)}{\partial \omega} \right)_{\omega=\omega_0} = \left(\frac{\partial (k_0 n(\omega))}{\partial \omega} \right)_{\omega=\omega_0}. \tag{2.1}$$

where k is the wave number which equals to $k(\omega) = k_r(\omega) + ik_i(\omega) = k_0 n(\omega) + i\alpha(\omega)/2$ and $\alpha(\omega)$ is the absorbance. The Taylor expansion of $k(\omega)$ around ω_0 can be written as:

$$k(\omega) = k_0 + (\omega - \omega_0)\frac{dk}{d\omega}|_{\omega=\omega_0} + \frac{1}{2}(\omega - \omega_0)^2 \frac{d^2k}{d\omega^2}|_{\omega=\omega_0} + \ldots \tag{2.2}$$

The first order term in Eq.2.2 is related to the group velocity term and the second order term is to the group velocity dispersion (GVD) term. GVD and higher order Taylor expansion terms of the dispersion $k(\omega)$ should be small compared to first order term to describe the velocity of the envelope of the wave packet.

For a dispersive medium, the group velocity can also be written:

$$v_g = c/(n + \omega\, dn/d\omega) = c/n_g \tag{2.3}$$

where n_g is *group index*. On the other hand, group velocity will be equal to phase velocity when the medium in which the wave packet travels is non-dispersive. For the vacuum, the dispersion relation is linearly dependent on the wave number which means $\omega = ck$. The phase velocity and the group velocity are the same and both equal to c in this case:

$$v = \omega/k = \partial\omega/\partial k = c = v_g. \tag{2.4}$$

2.1.2 Dispersion relation of an isolated oscillator (the Lorentz oscillator model)

Even though the Lorentz oscillator model is purely classical, it gives a very basic, but insightful understanding of atom-light interactions. The "atom" is represented by two oppositely charged particles (nucleus and electron) connected by a spring as shown in

Fig. 2.1a. The nucleus has a much larger mass than the electron. The light is represented by an electric field varying with time. The dispersion of photon (light) and oscillator ("atom") is shown Fig. 2.1b, when they do not interact.

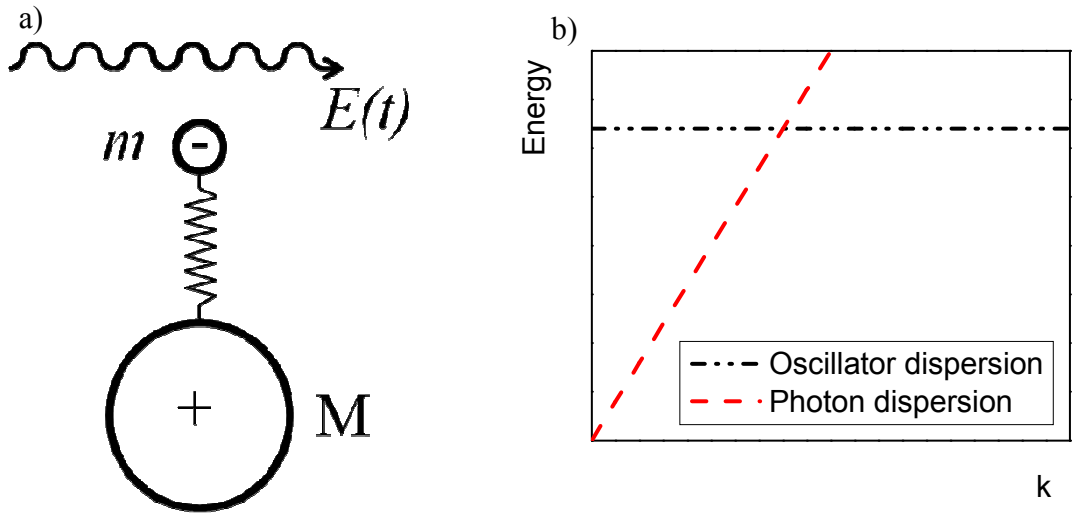

Figure 2.1 The Lorentz model. a) Basic schematic of light and matter interaction. Light is represented with an oscillating electric field. Electron and heavy nucleus are oppositely charged and they are connected with a spring. b) Oscillator and photon dispersion when light and matter are not interacting.

When "atom" and light interact, the electric field of the light will attract or repel the much lighter electron while the heavy nucleus remains stationary. Therefore, the field sets the electron into the motion, and displaces it by an amount x from its equilibrium position. This can be expressed by the following equation:

$$\frac{d^2\vec{x}(t)}{dt^2} + \gamma\frac{d\vec{x}(t)}{dt} + \omega_0{}^2\vec{x}(t) = -\frac{e}{m}\vec{E}(t) \tag{2.5}$$

where γ is the damping rate, ω_0 is the characteristic frequency of mass-spring system, e is the charge of electron, m is the mass of the electron and $\vec{E}(t)$ is the electric field of the

light wave. For a propagating monochromatic wave, the electric field that can be written as $\vec{E}(t) = \vec{E}_0(\omega) * e^{-i(kx-\omega t)}$. If we look for the solutions in the form of $\vec{x}(t) = \vec{x}_0(\omega) * e^{-i(kx-\omega t)}$, we can easily obtain $\vec{x}_0$.

$$\vec{x}_0 = \frac{-e\vec{E}_0 / m}{{\omega_0}^2 - \omega^2 - i\omega\gamma}. \tag{2.6}$$

The polarization per unit volume associated with the motion of electron will be

$$\vec{P}(t) = -Ne\vec{x}(t) = \frac{Ne^2 / m}{{\omega_0}^2 - \omega^2 - i\omega\gamma}\vec{E}(t) \tag{2.7}$$

where N equals the number of molecules per unit volume. The polarization and the electric field are correlated with complex susceptibility in the linear limit:

$$\vec{P} = \varepsilon_0 \chi(\omega)\vec{E}. \tag{2.8}$$

Therefore, the optical susceptibility is given by

$$\chi(\omega) = \frac{Ne^2 / \varepsilon_0 m}{{\omega_0}^2 - \omega^2 - i\omega\gamma}. \tag{2.9}$$

$\vec{P}$ and $\vec{E}$ should also satisfy the wave equation

$$\nabla^2\vec{E} - \frac{1}{c^2}\frac{\partial^2\vec{E}}{\partial t^2} = \frac{1}{c^2\varepsilon_0}\frac{\partial^2\vec{P}}{\partial t^2}. \tag{2.10}$$

If $\vec{P}$ is substituted into the equation above, and it is solved for k^2, we get

$$k(\omega)^2 = (|\, k_0.n(\omega) + i\frac{\alpha(\omega)}{2}\,|)^2 = \frac{\omega^2}{c^2}(1 + \chi(\omega)) \tag{2.11}$$

where ω is the absorption coefficient. This result will be the dispersion relation for this system. Note that we already solved for $\chi(\omega)$, and $\chi(\omega)$ is a complex number.

The model described here, is just for one oscillator, and it does not take background index, quantum well (QW) thickness, etc… into account. Therefore, the optical susceptibility of MQW samples which has been used in the measurements will be calculated from the 2D Elliot formula [51,52] which in SI units can be written as

$$\chi_{2D}(\omega) = -\frac{g}{\varepsilon_0}\frac{\left|d_{cv}^2\right|}{\hbar\omega - E_{hh} + i\gamma} \tag{2.12}$$

as in Ref. 22. $g = 8/\pi a_0^2$ is the 2D, 1s exciton probability density of finding the electron and hole in the same location where a_0 is the Bohr radius and 150 Å for bulk GaAs. d_{cv} is the dipole moment, E_{hh} is the 1s hh exciton energy, and γ is the non-radiative, homogeneous exciton dephasing rate. The dipole moment d_{cv}, and the damping γ which sets the oscillator strength and width of the transition, respectively, were chosen to give an absorption line that is close to the experimentally measured absorption line of the 1s heavy-hole exciton of the GaAs/AlGaAs MQWs. The real and imaginary parts of the 2D optical susceptibility $\chi_{2D}(\omega)$ are shown in Fig. 2.2a.

Experimentally, index of refraction and absorbance are more relevant quantities than the real and imaginary parts of the optical susceptibility. The index $n(\omega)$ and absorption $\alpha(\omega)$ for the (QW) can be calculated from the susceptibility:

$$n(\omega) = \sqrt{\frac{1}{2}\left(n_b^2 + \frac{1}{L}\chi_r^{2D}(\omega) + \sqrt{\left\{ n_b^2 + \frac{1}{L}\chi_r^{2D}(\omega)\right\}^2 + \left\{\frac{1}{L}\chi_c^{2D}(\omega)\right\}^2}\right)} \tag{2.13}$$

$$\alpha(\omega) = \frac{\omega}{cn\ (\omega)L}\chi_c^{2D}(\omega) \tag{2.14}$$

where n_b is the background index ($n_b = 3.6$ for Bulk GaAs), L is the quantum well thickness, and χ_r^{2D} and χ_c^{2D} are real and imaginary part of the 2D optical susceptibility, respectively. In Fig. 2.2b, simulated absorbance and index of refraction for $d_{cv} = 4.0$ eÅ, $\gamma = 0.5$ meV and $L = 140$ Å are shown. These parameters have been chosen to simulate a 20 GaAs/AlGaAs quantum well structure at 80 K which will be shown in Chapter 3.

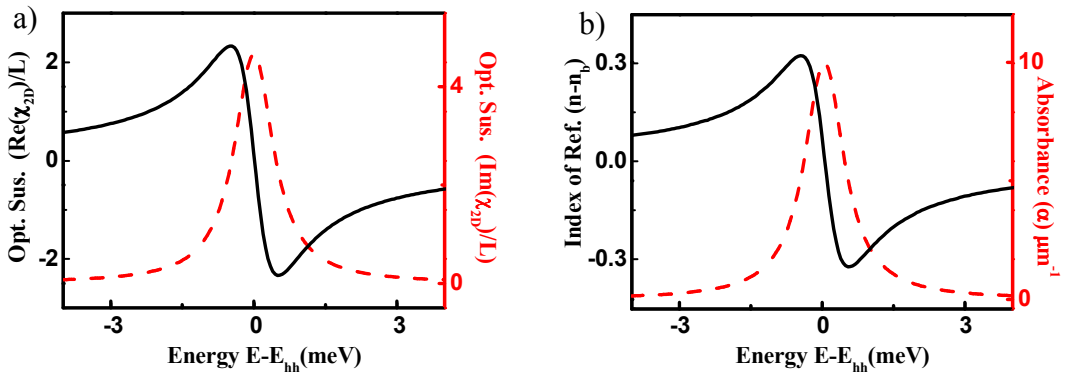

Figure 2.2 Calculations for MQW structures in Chapter 3. a) Calculated (with use of 2D Elliott formula) real (solid black) and imaginary (dashed red) part of the optical susceptibility which normalized with QW thickness L. b) Simulated index of refraction (solid black) and absorbance (dashed red) of the 20 GaAs/AlGaAs MQW structure.

2.1.3 Excitons in MQW

In bulk semiconductors, the discrete exciton levels associated with the Coulomb interaction between the electron and hole are characterized by a quantum number n_{ex} that is given atomic-like assignments s, p, d, etc. Similar to bulk semiconductors (Appendix A), the binding energy of the exciton states of n_{ex}=1, 2, 3, etc. for MQW structures is given by

$$E_{nex} = \frac{E_R}{(n_{ex} - 1/2)^2} \tag{2.15}$$

where the Rydberg energy is $E_R = \frac{\hbar^2}{2\mu a_0^{\,2}} = \frac{e^2}{(4\pi\varepsilon)a_0}$, the reduced effective mass μ is given by the equation $\frac{1}{\mu} = \frac{1}{m_e^*} + \frac{1}{m_h^*}$, a_0 is the exciton Bohr radius, and ε is the permittivity of both the barrier and well material in the static limit (also assuming ε is very similar for both well and barrier semiconductor). The binding energy of the excitons in MQWs is greater than those of bulk semiconductors (about four times higher for an idealized 2-D case for infinite wells and infinitely narrow well width for 1s excitons). This is an effect of localization of electrons and holes in the quantum wells due to increased overlap of electron and hole wavefunctions.

In MQW's, these levels are further quantized by the confinement in the growth direction, e.g., *z*. The conduction and valence bands are similarly split into a series of step-like sub-bands by this confinement. Here, we will focus only on lowest lying excitonic 1s ($n_z = 1$, $n_{ex} = s$) level. The confinement in the MQW heterostructure also lifts the degeneracy between the heavy hole and light hole bands. Therefore, both the 1s heavy hole and light hole exciton resonances can be seen in Fig. 2.3 in contrast to bulk semiconductors. For a comparison of excitons in bulk semiconductors to the excitons in MQWs one can check Appendix A which describes some of the basic concepts for bulk semiconductors and MQWs. Also, note that the 1s hh absorptive resonance can be approximated as a Lorentzian superimposed on a quantized step-like band.

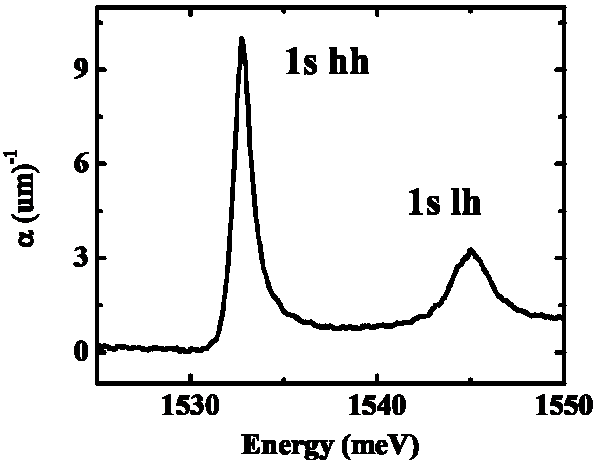

Figure 2.3 The absorption profile is shown near the 1s resonance for a MQW structure as a function of energy. The 1s heavy hole and light hole excitonic resonances are separated because of the confinement effects of quantum well structure.

2.1.4 Kramers-Kronig Relations

Optical susceptibility, $\chi(\omega)$, characterizes the response (in this case it is in the form of the polarization) of the medium to light. The Kramers-Kronig (KK) relations allow us to find the real part of this response if we know the imaginary part of the response at all frequencies, and vice versa. The KK relations are very general and rely on the causality and locality of the response.

$$\chi_c(\omega) = \frac{-2\omega}{\pi} P\int_0^\infty \frac{\chi_r(\omega')}{\omega'^2 - \omega^2} d\omega' \tag{2.16}$$

$$\chi_r(\omega) = \frac{2}{\pi} P\int_0^\infty \frac{\omega' \chi_c(\omega')}{\omega'^2 - \omega^2} d\omega' \tag{2.17}$$

where P is the principle value, $\chi_r(\omega)$ and $\chi_c(\omega)$ are the real and complex part of the optical susceptibility, respectively.

This is not the form of the KK relations that we want to use. First, obtaining either of these components by measurement at all frequencies is not realistic. Second, what we really need in our planned experiments and calculations is the absorption and index of refraction of the quantum wells rather than the real and imaginary part of the optical susceptibility.

By assuming $n_b^2 + \frac{\chi_r^{2D}}{L}(\omega) >> \frac{\chi_c(\omega)}{L}$, Eq. 2.13 can be written as:

$$n(\omega) = \sqrt{n_b^2 + \frac{1}{L}\chi_r^{2D}(\omega)} = n_b\sqrt{1 + \frac{1}{n_b^2 L}\chi_r^{2D}(\omega)} \ . \tag{2.18}$$

If $\frac{1}{n_b^2 L}\chi_r^{2D}(\omega) << 1$, then Eq. 2.18 becomes

$$n(\omega) - n_b = \frac{1}{2n_b L}\chi_r^{2D}(\omega) . \tag{2.19}$$

Substituting Eq. 2.17, then Eq. 2.14 into Eq.2.19, one can get:

$$n(\omega) - n_b \cong \frac{c}{\pi} P\int_0^\infty \frac{\alpha_{QW}(\omega')}{\omega^2 - \omega'^2} d\omega' \tag{2.20}$$

by assuming $|n(\omega) - n_b| << n_b$.

The absorption coefficient of a single quantum well sample α_{QW} can be obtained from a transmission measurement only over a finite range. However, in practice, to get sufficient signal to noise ratio, 10 or 20 quantum wells have been employed. The range of the transmission measurement has been chosen to contain the 1s hh absorption resonance

and the sharp index change (and anomalous dispersion) associated with the 1s hh absorption resonance.

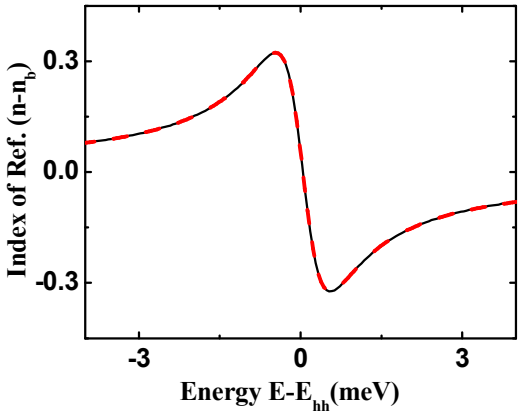

Figure 2.4 The indices of refraction profiles for the simulation of the MQW structure used in measurements in Chapter 3. The black solid curve is directly calculated from optical susceptibility whereas the red dashed one is calculated by using Kramer-Kronig transformation of the absorption profile.

After the absorption coefficient per quantum well over a sufficient range is acquired, the index $n(\omega)$ can be attained from Eq. 2.20. Note that even though the integration range of Eq. 2.20 is from zero to infinity, in practice, it is just the frequency range of the transmission measurement. More detail can be found in Ref. 1. To check the validity of this approach, Fig. 2.4 shows two indices of refractions. First is calculated exactly from optical susceptibility same as in Fig. 2.2 and the second is calculated approximately with use of Eq. 2.20 from a simulated absorbance with the same parameters. The excellent agreement between the two approaches validates the use of Eq. 2.20 in this instance to experimentally extract n_{QW} from the measure α_{QW} .

2.1.5 A simple calculation of group delay in slow light medium

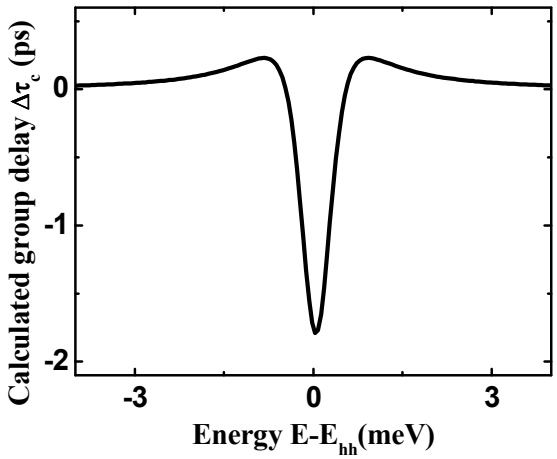

Figure 2.5 The calculated group delay for a simulated absorption resonance.

The typical energy dependence of pulse propagation near an absorptive resonance is of interest for this research. Therefore, the calculated group delay $\Delta\tau_c$ for the simulated GaAs / AlGaAs MQW resonance can be evaluated. The group index n_g from Eq. 2.3 and $\Delta\tau_c$ the calculated group delay are related through

$$\Delta\tau_c = \frac{L}{v_{group}} - \frac{n_b L}{c} = \frac{Ln_g}{c} - \frac{Ln_b}{c}. \tag{2.19}$$

For the index of refraction shown in Fig. 2.4, delay verses energy is shown in Fig. 2.5. Notice that the calculated group delay in Fig. 2.5 has both negative and positive values. Positive values indicate subluminal propagation, whereas negative values point to advancement in time or superluminal propagation. Also note that the superluminal propagation is in the area with negative slope in Fig. 2.4 where the anomalous dispersion

is present. The superluminal propagation also indicates a negative group velocity since the second term in Eq. 2.5 has already negative sign in front. Therefore pulse advancement as well as delay should be expected in the experimental results.

2.1.6 Slow light studies in literature

The study of the propagation of a wave packet in an absorbing medium without spatial dispersion (see Appendix A for the discussion of spatial dispersion and polaritons) started with Sommerfeld and Brillouin [3]. They have theoretically shown that the group velocity can exceed the speed of light in the vicinity of absorption resonance. After their surprising results, an extensive amount of theoretical work has been done [4-15]. Some of these studies [4-11] have focused on determining the propagation speed of the wave packet's envelope and when the group velocity is a valid way to describe the speed of the envelope through a resonant medium. In later theoretical work, superluminal propagation (fast-light) of the envelope and the meaning of superluminal propagation in terms of data transfer has been discussed [12-15].

The common understanding of wave-packet propagation through a dielectric medium can be summarized as follows. When the absorption of the material can be ignored (i.e. away from the absorption resonance), the group velocity always describes the propagation of light through dielectric media. However the group velocity can be zero, or negative when the medium has strong spatial dispersion. In some cases, superluminal (faster than c) propagation can be observed. There is no doubt, however, that you cannot transfer information faster than the speed of light in vacuum c [16].

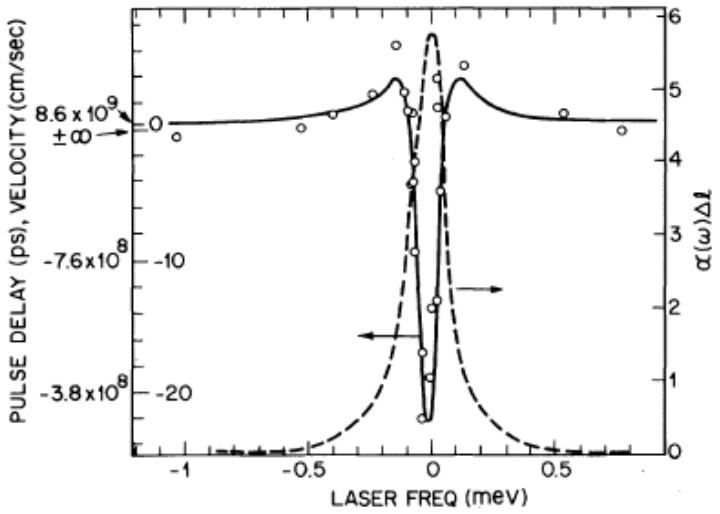

Figure 2.6 Summary of experimental results of Ref.24 (with permission of AIP). Absorption profile of N-doped GaP sample is shown. The pulse delay and group velocity versus energy graph is centered on the peak of the absorption profile.

There are two principal experimental studies in propagation of light through absorptive media. Wave propagation in the vicinity of the absorption resonance of nitrogen-doped gallium phosphide (GaP:N) has been investigated, by Chu and Wong [17]. Chu et al. observed a considerable amount of superluminal propagation (fast light) in addition to subluminal propagation as shown in Fig. 2.6. Notice the similarity between the Fig. 2.5 and Fig. 2.6 as well as observance of subluminal propagation in the wings and the superluminal propagation in the middle.

Next is the study of pulse propagation in the vicinity of the 1s exciton resonance in bulk gallium arsenide (GaAs) which has been investigated by Ulbrich and Fehrenbach [18]. When Ulbrich et al. tuned over the resonance, they observed only subluminal propagation (slow light), as seen in Fig. 2.7. There is no indication of superluminal

propagation, and there results (Fig. 2.7) are different from our calculation (Fig. 2.5) and Chu results (Fig. 2.6) in that sense.

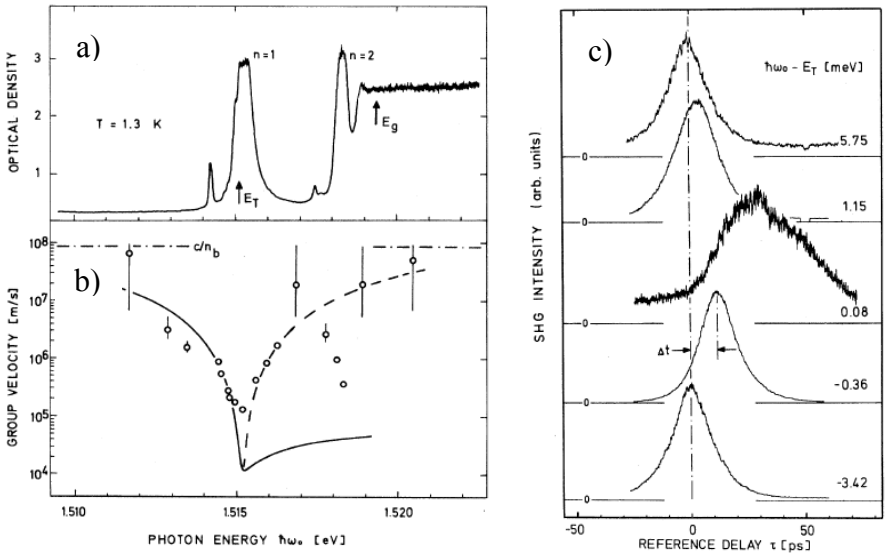

Figure 2.7 Summary of experimental results of Ref.23 (with permission of AIP). (a) Absorption profile of GaAs sample versus energy. (b) Group velocity versus energy measured by time-of-flight (TOF) measurements. (c) Individual TOF traces for corresponding detunings.

The presence of the spatial dispersion is the main difference between the two materials (bulk GaAs with spatial dispersion and GaP:N without; see Appendix A for a small discussion of spatial dispersion and polaritons). Ulbrich and Fehrenbach have also explained their experimental results with arguments of the spatial dispersion of polaritons [18]. However as will be seen in Chapter 3, the pulse propagation measurements are sensitive to other experimental conditions other than the sample. The spectral bandwidth of the incident pulse, linewidth of the absorption resonance can affect the measurements.

In a more recent study [20] and a conference presentation [21] (both shown in Fig. 2.8), Sarkar et al. studied pulse propagation in 50 period of GaAs/AlGaAs MQWs (17.5 nm well width), where spatial dispersion is expected to be unimportant in the growth direction. They observed only slow light when tuning across the absorption resonance and a 2-bit delay was observed.

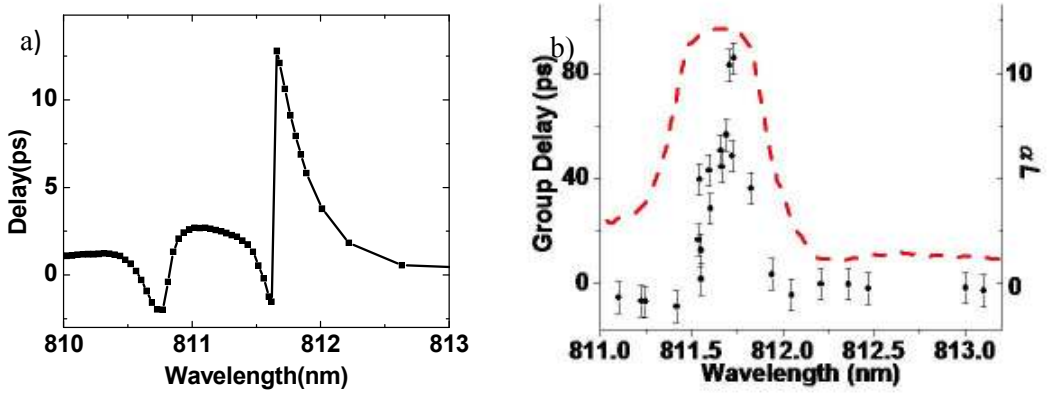

Figure 2.8 Summary of experimental results from Ref.s 25 and 26. a) Delay of 6 ps pulses versus wavelength is plotted in the vicinity of 1s hh (heavy hole) and lh (light hole) of GaAs/AlGaAs MQWs [25] (with permission of AIP) b) Delay of 100 ps pulses (black dots) versus wavelength is plotted in the vicinity of to 1s hh of the same resonance which is plotted as red dashes [26] (with permission of AIP).

Note that the MQW sample which Sarkar et al used should not have any spatial dispersion in propagation direction and the spectral pulsewidths in Sarkar's measurements cover a broader range than both Ulbrich or Chu' s measurements. However, Sarkar's results only show subluminal pulse propagation similar to Ulbrich's results, even though the mentioned experimental conditions are much more similar to Chu's results. Our calculated group delays also disagree with Sarkar's results.

As a result, a systematic investigation of light propagation on the absorptive resonance of the GaAs/AlGaAs MQW structure was carried out and the results of this investigation will be discussed in the next chapter.

CHAPTER 3: SUPERLUMINAL AND SUBLUMINAL PULSE PROPAGATION IN GAAS/ALGAAS QUANTUM WELLS

3.1 Introduction

Pulse propagation near an absorption resonance is a fundamentally important, textbook problem [25] first studied theoretically by Sommerfeld and Brillouin in absorptive media nearly a century ago [26]. Corresponding experimental studies did not follow until the advent of ultrafast pulsed lasers in the 1970's and 80's. Today, pulse propagation in slow light media and at tunable ultraslow group velocities is vital for applications like optical buffers and tunable delay lines, which would be useful in optical networks [for recent reviews see Refs. 53 and 54].

When studying light propagation in the vicinity of a resonance, the simplest case to consider is a medium made out of the uncoupled dipole oscillators (which has no spatial dispersion). Multiple quantum well (MQW) structures are an ideal medium to investigate the linear interaction of a light pulse with an absorptive medium consisting of identical, localized, and non-interacting dipoles. However, systematic experimental studies near the absorption resonances of MQW structures are lacking. The principal studies, [38,39] which are discussed in Chapter 2, are not in MQW structures. The only published studies [40, 41] in MQW structures to date are not yet supported by theory, and the results cannot be explained with dispersion theory. In this study, we systematically study pulse propagation both experimentally and theoretically in the vicinity of absorption resonances of GaAs/AlGaAs MQW structures.

When a pulse propagates through highly dispersive and/or heavily absorptive resonant media, the temporal and spectral profile of the incident pulse may become

distorted, depending on the pulse bandwidth and the sample thickness. The propagation speed of the distorted pulse can also deviate significantly from its group velocity. The concept of pulse propagation speed in a resonant media, and the validity of the group velocity description is a topic discussed in recent literature [27-30,33,39].

In this chapter, we follow the theoretical framework used in [55] for the description of pulse delay and propagation in resonant media. We experimentally test the group velocity description of slow and fast light by studying pulse propagation in MQWs with different number of quantum wells (20 and 40), and with different input pulse bandwidths ($\Delta\omega_p$=023, 0.84, and 1.6 meV). Furthermore, we will show simulations based on an exact theoretical description of pulse propagation and the full material dispersion accurately reproduces of the experimental results of pulse propagation in semiconductor MQWs.

3.2 Theory

3.2.1 Transit time

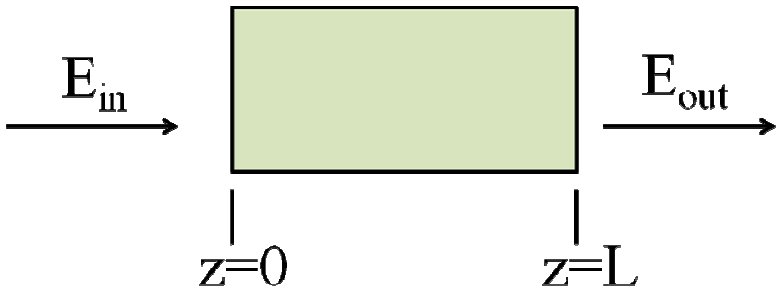

Figure 3.1 Electric field transmits through semiconductor slab which starts at z=0 and ends at z=L.

A complex electric field (which transmits through an absorptive medium as in Fig.3.1 has the form of $E(z,t) = \frac{1}{2\pi}\int E(\omega,z)\exp(ikz - i\omega t)d\omega$, where E(ω) is the pulse amplitude at frequency ω of the incident pulse. The complex transmission coefficient (transmissivity) of a homogeneous slab of dispersive material of width L can be expressed simply:

$$T(\omega) = \frac{E(\omega,L)}{E(\omega,0)} = \exp(i\phi(\omega)), \tag{3.1}$$

where $\phi(\omega)$ is the complex phase of transmission and, $E(\omega,0)$ and $E(\omega,L)$ are the incident and transmitted electric field at frequency ω, respectively. Here the MQW samples used in the experiment are modeled as resonant slabs of localized oscillators (excitons are localized in the propagation direction by the walls of the quantum wells) rather than structures having alternating layers.

When studying propagation of a light pulse though dispersive and absorptive media, defining a transit time $\bar{\tau}$ (time required to travel through the medium) can be difficult, because the temporal and spectral profile of the incident pulse may change as it travels through the media. For example, a single input pulse may be severely distorted or even break up into a pulse train. Therefore we use the first moment of the temporal profile of the pulse to determine the location of the pulse's center-of-mass. The transit time will be the difference in times between the arrival of the pulse "center-of mass" at the back (z=L) and front surface (z=0) of the MQW structure:

$$\bar{\tau}(\omega_0) = \frac{\int t\cdot\left|\mathrm{E}(L,t)\right|^2 \mathrm{d}t}{\int\left|\mathrm{E}(L,t)\right|^2 \mathrm{d}t} - \frac{\int t\cdot\left|\mathrm{E}(0,t)\right|^2 \mathrm{d}t}{\int\left|\mathrm{E}(0,t)\right|^2 \mathrm{d}t} \tag{3.2}$$

The complex field can be written in the form of $E(z,t) = \varepsilon(z,t)\exp[-i(\omega_0 t - kz)]$ where $\varepsilon(z,t)$ is the slowly varying amplitude and ω_0 is the center frequency of the pulse. Then, the transit time for a field can also be expressed as a convolution of the transit time of the individual frequencies, which is obtained from Eq. 3.2:

$$\bar{\tau}(\omega_0) = \frac{\int \tau(\omega)\cdot\left|\mathrm{E}(L,\omega)\right|^2 \mathrm{d}\omega}{\int\left|\mathrm{E}(L,\omega)\right|^2 \mathrm{d}\omega} = \frac{\int \tau(\omega).\left|E(\mathrm{L},\omega-\omega_0)\right|^2 d\omega}{\int\left|E(\mathrm{L},\omega-\omega_0)\right|^2 d\omega}, \tag{3.3}$$

where $$\tau(\omega) = \mathrm{Re}(\frac{\partial\phi}{\partial\omega}) = \mathrm{Im}(\frac{\partial \ln T}{\partial\omega}) = \mathrm{Im}(\frac{1}{T}\frac{\partial T}{\partial\omega}), \tag{3.4}$$

and $T(\omega)$ is the complex transmission coefficient as mentioned above. Then, $\bar{\tau}(\omega_0)$ is the convolution of the transmitted pulse spectrum $E(L,\omega)$ with the material dispersion $\tau(\omega)$. In the case of no spatial dispersion through a simple absorptive resonance, it is straightforward to show that $\tau(\omega)$ reduces to the group delay $\tau(\omega) = \frac{L}{v_g(\omega)} = L\frac{\partial(k_0 n)}{\partial\omega}$, where $k = k_r + ik_i = k_0 n + i\alpha/2$ is the complex wavevector. When in addition the spectrum of the electric field is much narrower than τ(ω)so that it acts like a delta function in Eq. 3.3, the pulse delay in Eq. 3.3 will reduce to the group delay: $\bar{\tau}(\omega_0) = L/v_g(\omega)$ On the other hand, as the spectrum of the incident pulse gets broader, the dispersive features of $\bar{\tau}(\omega_0)$ will be smoothed and rounded by the convolution of $\tau(\omega)$ .with the transmitted electric field.

3.2.2 Effects of the finite spectrum of the incident pulse

For finite spectral bandwidth, it is desirable to come up with a clear set of parameters that specify when the pulse delay deviates from the group delay, and when it

is distorted. We begin by looking at the inverse Fourier transform of the transmitted pulse [55]:

$$E(L,t) = \frac{1}{2\pi}\int \exp(-i\omega t)E(L,\omega)d\omega\,. \tag{3.5}$$

Let us define a complex phase,

$$\phi(\omega) = -i\ln T(\omega)\,. \tag{3.6}$$

Also, from Eq. 3.1, $E(L,\omega)$ can be written as $E(L,\omega) = T(\omega)E(0,\omega)$. Equation 3.5 can then be expressed as:

$$E(L,t) = \frac{1}{2\pi}\int \exp(i\phi(\omega) - i\omega t)E(0,\omega)d\omega\,. \tag{3.7}$$

Next we expand $\phi(\omega)$ in a Taylor series about ω_0, which is the center frequency of the incident pulse [55]:

$$\phi(\omega) = \phi(\omega_0) + (\omega-\omega_0)\frac{d\phi(\omega_0)}{d\omega} + \frac{1}{2}(\omega-\omega_0)^2\frac{d^2\phi(\omega_0)}{d\omega^2} + ...\,, \tag{3.8}$$

where all the derivatives are with respect to ω and they are evaluated at ω_0. Let us introduce the following notation for simplicity and clarity:

$$\phi(\omega) = \phi_r(\omega) + i\phi_i(\omega)\ , \tag{3.9a}$$

$$\Delta\omega = \omega - \omega_0\,. \tag{3.9b}$$

Then Eq. 3.7 will become:

$$E(L,t) = \frac{1}{2\pi}\exp\left[-i(\omega_0 t - \phi_r(\omega_0)) - \phi_i(\omega_0)\right]$$

$$x\int E(0,\omega_0+\Delta\omega)\exp\left[-i\Delta\omega(t-\tau(\omega_0))\right]\exp\left[i\frac{\Delta\omega^2}{\Delta\omega_{GVD}^2} - \left(\frac{\Delta\omega}{\Delta\omega_{\alpha 1}} + \frac{\Delta\omega^2}{\Delta\omega_{\alpha 2}^2}\right)\right]d\Delta\omega\ , \tag{3.10}$$

where $\tau(\omega) = \mathrm{Re}\dfrac{d\phi(\omega)}{d\omega}$ ($\ln T(\omega) = i\phi(\omega)$), and $\Delta\omega_{GVD}$, $\Delta\omega_{\alpha 1}$, and $\Delta\omega_{\alpha 2}$ are defined as below:

$$\frac{1}{\Delta\omega_{GVD}^2} = \frac{1}{2}\mathrm{Re}\frac{d^2\phi}{d\omega^2} = \frac{1}{2}\frac{d\tau}{d\omega}, \tag{3.11a}$$

$$\frac{1}{\Delta\omega_{\alpha 1}} = \mathrm{Im}\frac{d\phi}{d\omega} = -\mathrm{Re}\left(\frac{d\ln T}{d\omega}\right), \tag{3.11b}$$

$$\frac{1}{\Delta\omega_{\alpha 2}^2} = \frac{1}{2}\mathrm{Im}\frac{d^2\phi}{d\omega^2} = \frac{1}{2}\frac{d}{d\omega}\left(\frac{1}{\Delta\omega_{\alpha 1}}\right). \tag{3.11c}$$

For the special case of $T = \exp(ikL)$, $\tau(\omega)$ will become

$\tau(\omega) = \dfrac{d\,\mathrm{Re}(k)}{d\omega}L = \dfrac{dn}{d\omega}k_0 L = \dfrac{L}{v_g}$ and Equations 3.11a-c will be equal to:

$$\frac{1}{\Delta\omega_{GVD}^2} = \frac{1}{2}\frac{d^2 n}{d\omega^2}k_0 L, \tag{3.12a}$$

$$\frac{1}{\Delta\omega_{\alpha 1}} = \frac{1}{2}\frac{d\alpha}{d\omega}L, \tag{3.12b}$$

$$\frac{1}{\Delta\omega_{\alpha 2}^2} = \frac{1}{4}\frac{d^2\alpha}{d\omega^2}L. \tag{3.12c}$$

Then, $\tau(\omega)$, $\Delta\omega_{GVD}$, $\Delta\omega_{\alpha 1}$, and $\Delta\omega_{\alpha 2}$ will be directly connected to material parameters of the propagation media, namely the index of refraction and the absorption coefficient. Therefore, this new formalism relates the propagation integral (Eq. 3.10) to basic material properties elegantly. When the spectral bandwidth of the incident pulse, $\Delta\omega_p$ (full-width at half maximum), is much narrower than $\Delta\omega_{GVD}$, $\Delta\omega_{\alpha 1}$, and $\Delta\omega_{\alpha 2}$, the pulse envelope of the transmitted field $E(L,t)$ can be seen from Eq. 3.10 to reduce to the pulse envelope

of the incident field $E(0,t)$. As $\Delta\omega_p$ get broader, the transmitted pulse spectrum will be modified and distorted, and the transit time $\bar{\tau}(\omega_0)$ will deviate from the group delay.

3.3 Experimental study

Experimental arrangements and techniques which were utilized to investigate the pulse propagation in GaAs/AlGaAs MQW samples will be presented and discussed in this section. First, samples and pulse-shaper which were used will be described briefly. Then, the basic technique for a time-of-flight measurement will be introduced.

3.3.1 Samples

In this study, quantum well structures grown by molecular beam epitaxy at the University of Iowa with 20 and 40 wells were used. The reason for choosing these samples is that if the number of quantum wells is too few (much less then 20) in MQW structure, it is hard to observe the effects dispersion and pulse distortion after propagation through the sample. On the other hand, if the sample is too thick (more than 40 QWs), then the absorption of the sample limits the detection of spectrally narrow pulses when the pulses propagates in the vicinity of the absorption resonance.

The samples which were used in these measurements contain GaAs quantum wells which are 14 nm thick and the $Al_{0.33}Ga_{0.67}As$ barriers which are 17 nm thick. The quantum wells were grown on a (100) GaAs substrate with an $Al_{0.33}Ga_{0.67}As$ etch stop layer. After growth, the samples were mounted epilayer-down on BK-7 using optical adhesive (Norland #61). The substrates were then removed mechanically. The rest of the substrate was removed chemically using the recipe in Ref. 56.

Figure 3.2 shows a high resolution measurement (20 μeV) of the 1s heavy-hole absorption profile for the N=20 (black solid), and 40 (black dashed) quantum well

structures. At 80 K, the heavy-hole exciton of the 20 and 40 quantum well samples exhibited a narrow full width at half maximum of 1.10 meV, showing samples are of high quality.

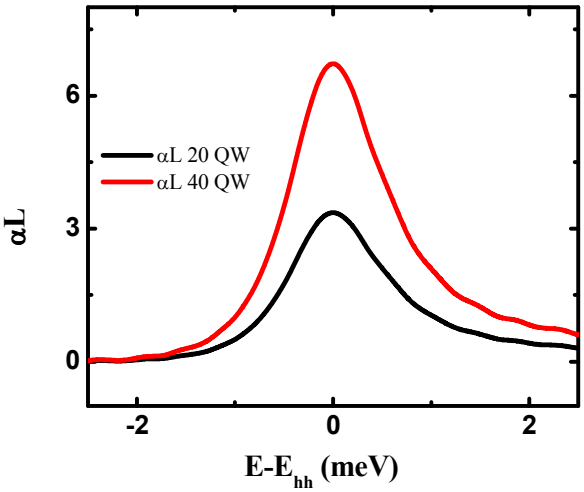

Figure 3.2 Measured absorption coefficient of the 1s heavy-hole absorption profile for 20 (black), and 40 (red) quantum well structures at 80 K.

3.3.2 Pulse shaper

In experimentally investigating pulse propagation in the presence of an absorptive resonance, control of the spectral width of the incident pulses is important. Such control can be achieved with a pulse shaper. A pulse shaper operates by using a grating-lens pair to spatially disperse different spectral components of the pulse into a continuum of points in the focal plane of a lens. A reflective mask or slit-mirror pair is used in the focal plane to attenuate the undesired spectral components, and then reflect the light back through the lens-grating pair, recombining spectral components. By altering the amplitude of

different spectral components, the pulse is also shaped temporally according to an inverse Fourier transform [57,58].

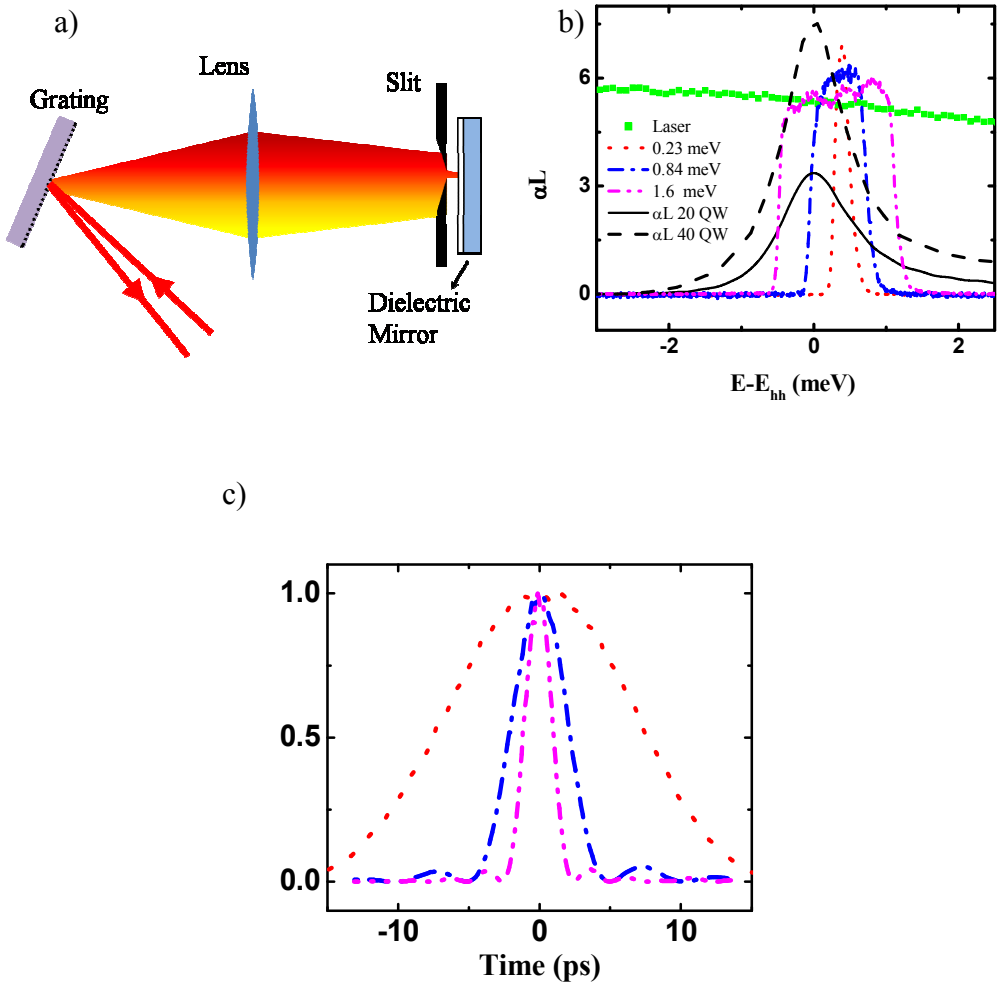

Figure 3.3 A schematic of the pulse shaper used in the experiments, and related spectra and time traces of the shaped pulses**.** a) Simple schematic of the pulseshaper. b) Spectra of the unshaped laser pulse (green squares), $\Delta\omega_p$=0.23 meV (red dots), $\Delta\omega_p$=0.84 meV (blue dash-dot), $\Delta\omega_p$=1.6 meV (magenta dash-dot-dot) bandwidth pulses, and 1s heavy-hole absorption profile for 20 (black solid) and 40 (black dashed) QW structures at 80 K. c) Corresponding cross-correlation traces for $\Delta\omega_p$=0.23 meV (red dots), $\Delta\omega_p$=0.84 meV (blue dash-dot), $\Delta\omega_p$=1.6 meV (magenta dash-dot-dot) bandwidth pulses with unshaped laser pulse.

The pulse shaper used in this experiment is illustrated schematically in Fig. 3.3a. It was used to shape 100 femtosecond (fs) pulses generated by an 80 MHz mode-locked Ti:Sapphire (Mai Tai Spectra-Physics) laser. A variable slit-mirror pair was used in the focal plane of a grating-lens pair to select the desired width of the pulse. By checking the product of the spectral and temporal width of the pulses, we make sure that the pulses are roughly transform-limited. The slit width and position enable us to control the spectral width $\Delta\omega_p$ and central frequency ω_0, respectively, relative to the frequency of the 1s heavy hole exciton resonance ω_x ($E_{hh} = \hbar\omega_x \approx 1532.77 meV$) of the quantum well sample.

Figure 3.3b shows the spectrum of the shaped pulses used in the experimental work described here. In particular, spectra of the unshaped laser pulse (green squares), and $\Delta\omega_p$=0.23 meV (red dots), $\Delta\omega_p$=0.84 meV (blue dash-dot), and $\Delta\omega_p$=1.6 meV (magenta dash-dot-dot) bandwidth pulses are shown with respect to the absorption resonances of 20 QW (black solid) and 40 QW (black dash) samples. Figure 3.3c shows the temporal profile of the shaped pulses of $\Delta\omega_p$=0.23 meV (red dots), $\Delta\omega_p$=0.84 meV (blue dash-dot), and $\Delta\omega_p$=1.6 meV (magenta dash-dot-dot) in arbitrary units.

3.3.3 Experimental arrangement and time-of-flight measurements

Figure 3.4 shows a schematic of the experimental geometry used to investigate pulse propagation through quantum well samples. The laser is separated into probe and reference beams using a beam splitter. The probe pulse propagates through a quantum well sample after it has been shaped. The transmitted probe pulse is split into two paths, one for spectrally resolving the probe and the other for temporally resolving the probe.

Spectral resolution of transmitted pulses was achieved with a spectrometer with 0.1 meV resolution. Temporal resolution of the pulse was achieved by cross-correlating the transmitted probe with an unshaped 100 fs reference pulse by second harmonic generation (SHG) [59] with use of a beta barium borate (BBO) crystal. By varying the delay between the two pulses, the temporal profile of the transmitted pulse is mapped out, a technique known as a *time-of-flight (ToF) measurement*. The cross correlation signal is detected after the BBO crystal by a photomultiplier tube (PMT) as a detector. The probe is chopped and the cross-correlated signal measured using a lock-in amplifier referenced to the chopping frequency. Then, the experimentally measured τ_m with respect to nonresonant frequencies can be defined as by using first moment of the ToF trace:

$$\tau_m(\omega_0) = \frac{\int t \cdot \left|\mathrm{E}_{\mathrm{SHG}}(t,\omega_0)\right|^2 \mathrm{d}t}{\int \left|\mathrm{E}_{\mathrm{SHG}}(t,\omega_0)\right|^2 \mathrm{d}t} - \frac{\int t \cdot \left|\mathrm{E}_{\mathrm{SHG}}(t,\omega_{NR})\right|^2 \mathrm{d}t}{\int \left|\mathrm{E}_{\mathrm{SHG}}(t,\omega_{NR})\right|^2 \mathrm{d}t} \tag{3.13}$$

where $\left|\mathrm{E}_{\mathrm{SHG}}(t,\omega)\right|^2$ is the detected intensity after the SHG crystal and second term sets the delay at nonresonant frequencies to zero. The measured delay τ_m will be equal to the difference of the transit time at and below resonance:

$$\tau_{\mathrm{m}}(\omega_0) = \bar{\tau}(\omega_0) - \bar{\tau}(\omega_{NR}) \tag{3.14}$$

where $\bar{\tau}(\omega_{NR})$ is the transit time for nonresonant frequencies.

A challenge for the transmission measurements was obtaining sufficient number of photons for spectrally narrow pulses propagating through optically thick samples with absorbances in excess of 7. As the spectral width of the pulse gets narrower than the spectral band width of the absorption resonance, the pulse is almost totally absorbed in the vicinity of the peak of the absorption resonance profiles. The pulse fluence cannot be

turned up arbitrarily high because it will begin to induce a nonlinear material response. In order to boost the transmitted number of photons while keeping fluence low, the laser was only weakly focused to a relatively large spot, roughly 300 μm in diameter, on the sample surface.

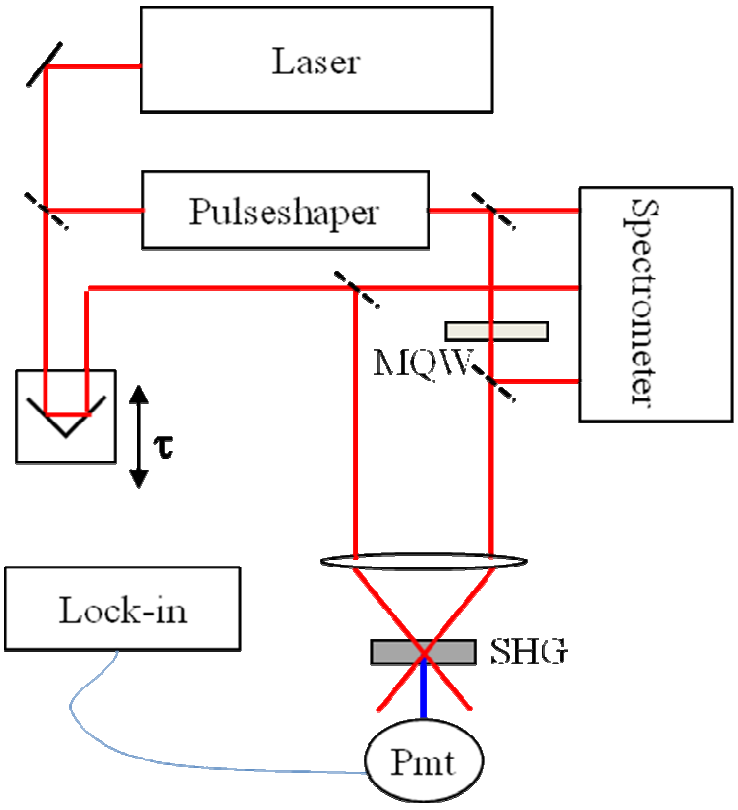

Figure 3.4 Basic geometry of the optical setup. Probe pulse goes through a pulse shaper before it transmits through MQW. After transmission the second harmonic generation (SHG) of probe and reference pulses is detected with a photo multiplier tube (PMT). The spectrometer measures the spectra of the probe pulse before and after the probe pulse transmit through the sample, and reference pulse.

For the measurements, the laser beam was focused on the sample with a fluence of approximately 1.5 nJ/cm2 per pulse. The linearity of the material response as a

function of fluence has been checked with an 0.84 meV pulse (~5 ps) centered on the 1s heavy hole exciton resonance of the 20 MQW sample. As seen in Fig. 3.5, no significant change was observed in transmitted pulse delay or integrated pulse absorption for fluences up to one order of magnitude greater than 1.5 nJ/cm^2.

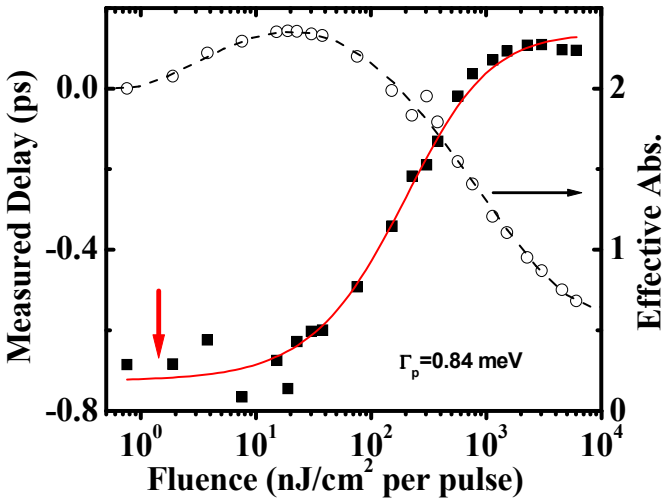

Figure 3.5 The fluence dependence of pulse propagation is tested with a tight focused spot on the 20 quantum well sample. The delays (solid squares) are measured with a pulse width 0.84 meV at heavy hole resonance. The effective absorbance (open circles) is calculated at each point. The red arrow points to the fluence corresponding approximately to that used in our measurements with a large excitation spot. (Black and red lines are guides to the eye)

3.4 Results and Analysis

We begin by comparing calculated group delay and measured delay near the 1s-hh exciton resonance in multiple quantum wells under a variety of conditions, such as wide and narrow input pulses, and thin (20 MQW) and thick (40 MQW) samples. The goal is to see both under what conditions group delay is obeyed, and if deviations from

group delay occur when predicted by the figures of merit (Eqs. 3.11a-c) developed in the prior section. The index of refraction is needed as function of frequency to make this calculation whereas only absorption is experimentally measurable. As discussed in Chapt. 2, the index of refraction is obtained from the absorption coefficient with use of the Kramer-Kronig relation.

We will then show that in cases where delay deviates from group delay, it can still be calculated from a transmission measurement alone through the sample (Eq. 3.3). Finally, we show that for both wide and narrow pulses propagating through the thick MQW samples, temporally and spectrally resolved pulse transmission can be accurately modeled from an exact calculation using the full dispersion relation.

3.4.1 Group delay in multiple quantum wells

As discussed in Sec. 3.2.2, Eq. 3.3 for the dispersive $\tau(\omega)$ reduces to the group delay for the simple case of a singly resonant material:

$$\tau(\omega) = \tau_g(\omega) = \frac{L}{v_g(\omega)} = \frac{Ln_g(\omega)}{c} \tag{3.15}$$

where L is the total width of quantum wells, c is the speed of light, and $n_g(\omega)$ is the dispersive group index of the MQW. The group index was obtained from the index of refraction (Fig. 3.6b) associated with the measured 1s-hh quantum well exciton (Fig. 3.6a). And the quantum well index of refraction was calculated from the measured absorption coefficient using a Kramers-Kronig transformation (Eq. 2.20).

The calculated group delay based on the extracted quantum well dispersion is shown as black squares in Figs. 3.7b and f for the 20 and 40 MQW samples, respectively. Under some circumstances, the measured transit time agrees with the expected group

delay as the frequency of the incident pulse is tuned across the quantum well resonance. For example, for the spectrally narrowest incident pulse ($\Delta\omega_p$ = 0.23 meV) and the thinner 20 MQW sample, the measured transit time (red circles, Fig. 3.7b) closely follows the group delay.

Furthermore, Fig. 3.7d shows the temporally resolved profile of transmitted pulses at pulse-exciton spectral detunings indicated in Fig. 3.7c. Very little pulse distortion occurs in each case. Figure 3.7c also shows the temporal full-width-at-half-maximum of the transmitted pulse tracked over a range of pulse- exciton detunings shows only a small change (about 5%) across the quantum well 1s hh resonance.

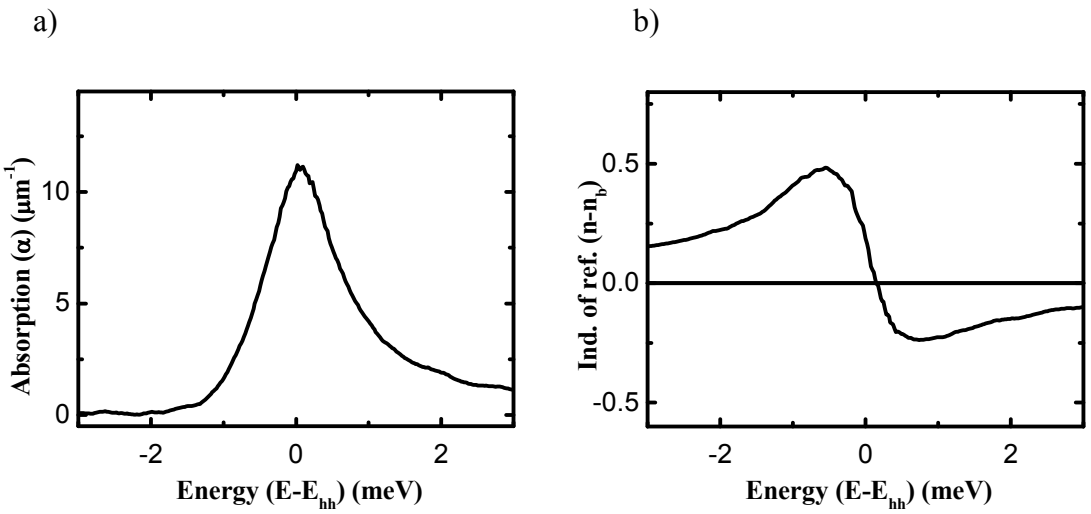

Figure 3.6 For the 20 MQW structure: a) Measured absorption coefficient. b) The index of refraction which is KK of absorbance in part a.

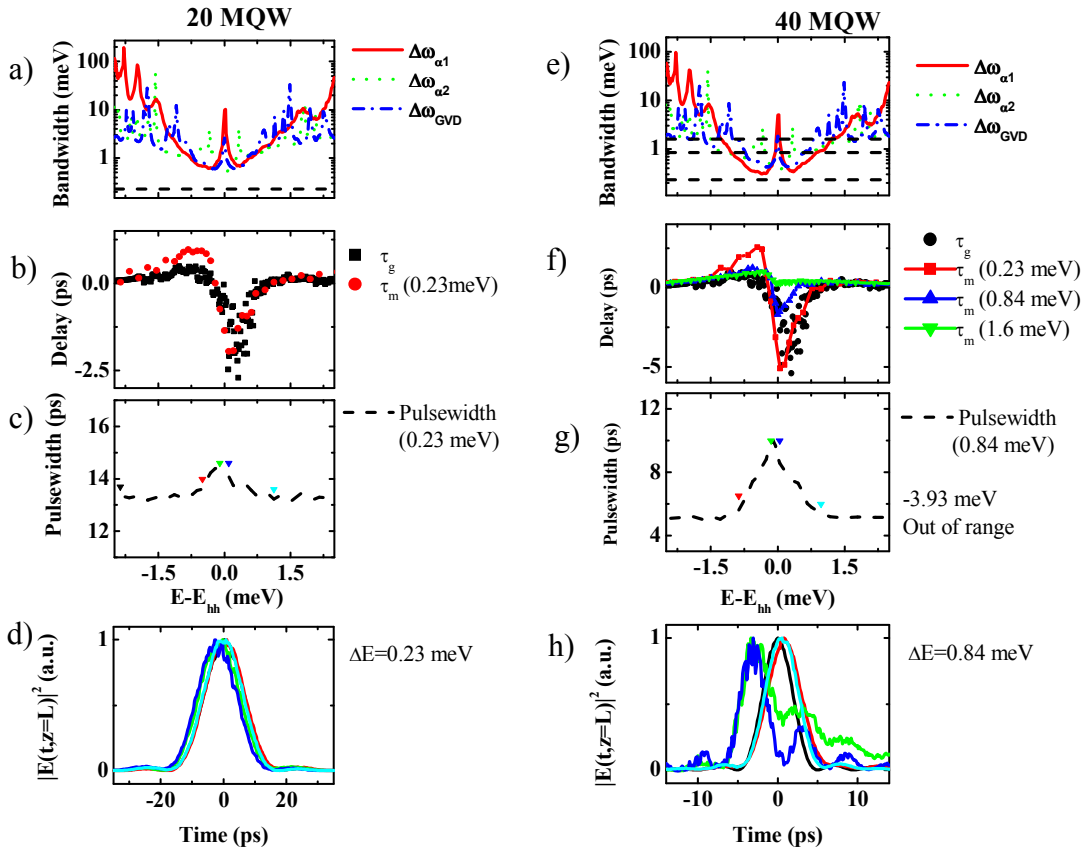

Figure 3.7 Experimental results and simulations. a) The spectral band width of the incident pulse $\Delta\omega_p$=0.23 meV (black dashed line), and figures of merits $\Delta\omega_{\alpha 1}$ (red solid), $\Delta\omega_{\alpha 2}$ (green dots), and $\Delta\omega_{GVD}$ (blue dash-dot) are plotted for 20 MQW. b) The measured delays, $\tau_m(\omega)$, for propagation of the 0.23 meV spectral bandwidth pulse through the 20 quantum well sample (red dots) and the calculated delay $\tau_g(\omega)$ (black dots). c) The pulsewidths are shown for the measured delays in part b. Color coded triangles mark the spectral position of chosen ToF measurements in part d. d) Normalized ToF measurements (all peak values are 1) are shown for the spectral positions marked in part c. e) The spectral band width of the incident pulses $\Delta\omega_p$=0.23, 0.84 and 1.6meV (black dashed lines), and figures of merits $\Delta\omega_{\alpha 1}$ (red solid), $\Delta\omega_{\alpha 2}$ (green dots), and $\Delta\omega_{GVD}$ (blue dash-dot) are plotted for 40 MQW. f) The measured delays, $\tau_m(\omega)$,for propagation of the 0.23 meV spectral bandwidth pulse through the 40 quantum well sample (red squares), 0.84 meV pulse (blue triangles, 1.6 meV pulse (green triangles) and the calculated delay $\tau_g(\omega)$ (black dots). g) The pulsewidths are shown for the measured delays in part f. Color coded triangles mark the spectral position of chosen ToF measurements in part h. h) Normalized ToF measurements (all peak values are 1) are shown for the spectral positions marked in part g.

On the other hand, for the thicker 40 MQW sample, Fig. 3.7f shows that the deviation of the measured transit time from the group delay gets progressively worse as the incident pulse bandwidth increases from $\Delta\omega_p$ = 0.23 meV to 1.6 meV. Figure 3.7h shows temporally resolved transmitted pulses at detunings indicated in Fig. 3.7g. The temporal pulse distortion shown in Fig. 3.7h is severe. The strong variation (factor of 2) in the pulse temporal full-width-at-half-maximum for the $\Delta\omega_p$ =0.84 meV pulse is shown in Fig. 3.7g.

A quantitative set of criteria that, taking into account input pulse width and sample thickness, accurately predicts when transit time will deviate from group delay is desired. These are the figures of merit $\Delta\omega_{\alpha 1}$, $\Delta\omega_{\alpha 2}$, and $\Delta\omega_{GVD}$ described in Eqs. 3.11a-c, and have been calculated from the measured dispersion for the 20 and 40 MQWs as shown in Figs. 3.7a and e, respectively.

Figure 3.7a shows that for the spectrally narrowest input pulse ($\Delta\omega_p$ =0.23 meV) transmitted through the 20 MQW sample, the input pulse bandwidth is smaller than $\Delta\omega_{\alpha 1}$, $\Delta\omega_{\alpha 2}$, and $\Delta\omega_{GVD}$ for all input pulse detunings. The minimum value of $\Delta\omega_{\alpha 1}$, $\Delta\omega_{\alpha 2}$, and $\Delta\omega_{GVD}$ is about 0.5 meV near resonance, about a factor of two larger still than in the input pulse bandwith. As expected, the measured delay $\tau_m(\omega_0)$ in this case shows reasonable quantitative agreement with the group delay $\tau_g(\omega_0)$ for all detunings shown in Fig. 3.7b. The only real disagreement between $\tau_m(\omega_0)$ and $\tau_g(\omega_0)$ is around a pulse-exciton detuning of about -1 meV on the low energy side, where $\Delta\omega_{\alpha 1}$, $\Delta\omega_{\alpha 2}$, and $\Delta\omega_{GVD}$ reach a minimum.

None of the incident spectral bandwidths (0.23, 0.84, and 1.6 meV) for the 40 MQW structure are much less than the figures of merit $\Delta\omega_{\alpha 1}$, $\Delta\omega_{\alpha 2}$, and $\Delta\omega_{GVD}$,as shown in Fig. 3.7e. For $\Delta\omega_p$=0.23 meV, which is about same as the 0.3 meV minimum of the characteristic bandwidths $\Delta\omega_{\alpha 1}$, $\Delta\omega_{\alpha 2}$, and $\Delta\omega_{GVD}$, the measured delay $\tau_m(\omega_0)$ agrees with $\tau_g(\omega_0)$ where the delay is negative (superluminal propagation) in Fig. 3.7f. However, the disagreement at negative pulse-exciton detunings is worse than the 20 MQW sample for the same spectral bandwidth. As the spectral bandwidth of the pulse is increased to $\Delta\omega_p$=0.84 meV, which is larger than the minimum of $\Delta\omega_{\alpha 1}$, $\Delta\omega_{\alpha 2}$, and $\Delta\omega_{GVD}$ as seen Fig. 3.7e, the measured delay $\tau_m(\omega_0)$ starts to differ considerably from the group delay $\tau_g(\omega_0)$, as can be seen in Fig. 3.7f. However the general features of slow and fast light can still be observed. As for the $\Delta\omega_p$=1.6 meV pulse, which is greater than $\Delta\omega_{\alpha 1}$, $\Delta\omega_{\alpha 2}$, and $\Delta\omega_{GVD}$ for almost all detunings, the measured delay $\tau_m(\omega_0)$ does not agree with $\tau_g(\omega_0)$ even qualitatively. Figures 3.7g shows the transmitted pulse temporal full width at half maximum for the 0.84 meV pulse incident on the 40 MQW sample. The pulse is broadened temporally by about a factor of 2. Figure 3.7h shows temporally resolved measurements of the 0.84 meV pulse after transmission through the 40 MQW sample. The transmitted pulses show significant distortion and break up.

As the bandwidth of the incident pulse widens, the features of the measured delay $\tau_m(\omega_0)$ get washed out in Fig. 3.7f. This washing out can be understood by looking at the convolution of $\tau(\omega)$ (Eq. 3.4) and the spectrum of the incident pulse (Eq. 3.3). When the incident pulse spectrum is narrow compared to $\tau(\omega)$, it is expected that the result of

the convolution will be similar to $\tau(\omega)$ itself. As the incident spectrum gets wider, the features of $\tau(\omega)$ will be washed out.

3.4.2 Calculation of delay for pulses with finite spectra

In last section, it was obvious that the group velocity does not always describe a pulse's propagation in the presence of a resonance. The group delay $\tau_g(\omega_0)$ calculated from the material dispersion takes into account neither transmitted nor incident pulse spectrum. It only assumes an infinitely narrow spectrum centered around ω_0 of the incident pulse. In the literature, there are attempts [29,30,33] to describe propagation of a pulse even in the vicinity of a resonance with a modified group velocity. In this section we show that Eq. 3.3, which calculates the delay of an input pulse from a weighted average of the group delay and the transmitted pulse spectrum, can be used to calculate the delay of any pulse with a finite spectral bandwidth.

To demonstrate the accuracy of Eq. 3.3, the probe pulse was spectrally positioned on the resonance of the 20 MQW sample, and the spectral width of the pulse was varied. Figure 3.10a shows the measured transmitted pulse spectrum for the different incident pulse bandwidths, and Fig. 3.8b the measured delays $\tau_m(\omega)$ (black squares). The red dots in Fig. 3.8b are calculated delays $\bar{\tau}_0(\omega_0 \approx E_{hh}/\hbar)$ for different spectral widths by using transmitted spectra and $\tau(\omega)$ in Eq. 3.3. The blue dashed line in Fig 3.8b shows the group velocity limit $\tau_g(\omega)$, which of course does not depend on the spectral width of the pulses.

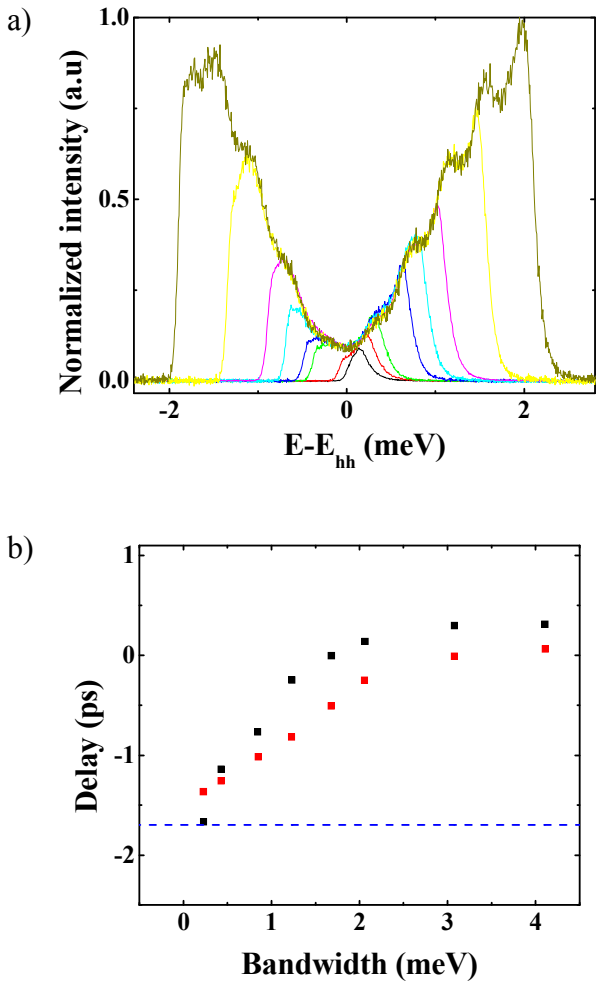

Figure 3.8 Exprimental results. a) Increasing the spectral bandwidth of the incident pulse at resonance (about ~ 0 meV detuning) b) Corresponding delays for measured $\tau_m(\omega)$ (black squares), group velocity limit $\tau_g(\omega)$ (blue dashed line), and calculated delays $\Delta\bar{\tau}_0(\omega_0 \approx \omega_x)$ (red dots) for different spectral bandwidths in part a.

For narrow incident spectral widths, delay times of pulses are consistent with group delay. As the bandwidth of transmitted spectra widens, the measured delay $\tau_m(\omega)$ deviates from the group delay. However, when the calculated delays $\bar{\tau}_0(\omega_0 \approx E_{hh}/\hbar)$ from Eq. 3.3 are compared to measured delay $\tau_m(\omega)$, there is good agreement between

both the narrow and wide spectral bandwidths. Also note that the observed slow-light-only measured delays in Fig. 3.7f for wide spectral bandwidths at 40 MQW sample is reproduced by this calculation technique. Because $\tau_g(\omega)$ is obtained from a transmission measurement, as described in Sec. 3.4.1, and Eq. 3.3 is a convolution of $\tau_g(\omega)$ and the pulse transmitted spectrum, pulse delay can be determined by a spectrally resolved transmission measurement alone.

3.4.3 Experimental and theoretical simulations of pulse propagation through GaAs/AlGaAs MQWs

In this section, we show that the experimental data on propagation of light through semiconductor GaAs/AlGaAs MQWs can be simulated with good agreement for both temporally wide and narrow input pulses with an exact theoretical model. Theoretical simulations were done by Adam Heiniger, who was provided with the experimental data, including the material dispersion obtained as described in Chapt. 2 and Sec. 3.4.1.

In the simulations, the quantum well structure is treated as a homogeneous slab with the same total thickness and absorption coefficient rather than taking individual wells into account. The program evaluates the complex transmissivity $T(\omega)$ of the structure by calculating the magnitude and phase of the electric field at the exit interface of the sample for a single frequency using the boundary conditions for the electric and magnetic fields at the two surfaces of the slab. Such a calculation requires the dispersion of the layer is known, and the simulation used the experimentally measured absorption coefficient and extracted index as described in Sec. 3.4.1. The propagation of a pulse

through the quantum well structure is simulated by propagating each individual frequency, and then integrating over all (weighted) pulse frequencies:

$$E(z_{in},t) = \int A(\omega)\exp[i(k(\omega)z_{in} - \omega\tau)]d\omega \tag{3.16}$$

$$E(z_{out},t) = \int T(\omega)A(\omega)\exp[i(k(\omega)z_{out} - \omega\tau)]d\omega \tag{3.17}$$

where $A(\omega)$ defines the spectral shape of the incident pulse profile [25]. Note this approach is exact in the sense that all orders of the complex phase of transmission are included in the calculation and does not use an expansion. During the integration over ω, the integrand is carefully monitored to ensure the ω step size does not exceed a fast oscillation period due to the proximity of a complex pole.

Figures 3.9 and 3.10 show a comparison of the experimentally measured temporal and spectral profiles of pulses transmitted through the 40 QW sample and theoretical simulations based on Eqs. 3.16 and 3.17. There is good overall agreement for both spectrally narrow ($\Delta\omega_p$=0.23 meV) and wide ($\Delta\omega_p$=0.84 meV) incident pulses, and for all pulse-exciton detuning ($\Delta E \equiv \hbar\omega_0 - \hbar\omega_x$). In both figures, the intensity of the transmitted pulse has been normalized to one for ease of comparison. Theoretically and experimentally, transmission of the narrow incident pulse in Fig. 3.9 shows superluminal advancement for small pulse spectral detunings from the 1s hh exciton resonance, and subluminal propagation at intermediate negative detunings. In all cases, little pulse distortion is observed. Similarly, theoretically and experimentally, transmission of the wide incident pulse in Fig. 3.10 shows superluminal and subluminal propagation close to the exciton resonance and intermediate negative detunings, respectively.

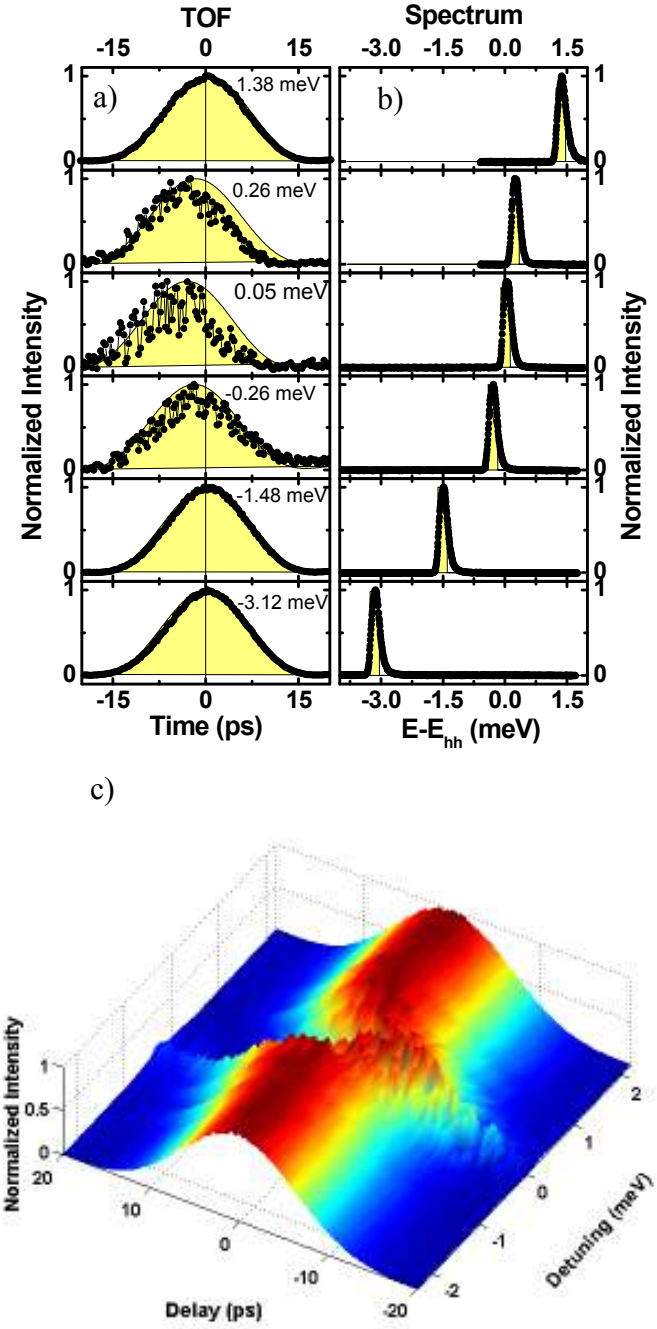

Figure 3.9 Experimental results and simulations. a) Individual TOF measurements (black) simulations (yellow shaded area) for the 40 quantum well sample and 0.23 meV spectral bandwidth incident pulse for different pulse-exciton detunings. b) Corresponding spectrum for TOF measurements (black dots) and simulations (yellow-shaded area). c) 3-D rendering of TOF measurements shown in parts a and b.

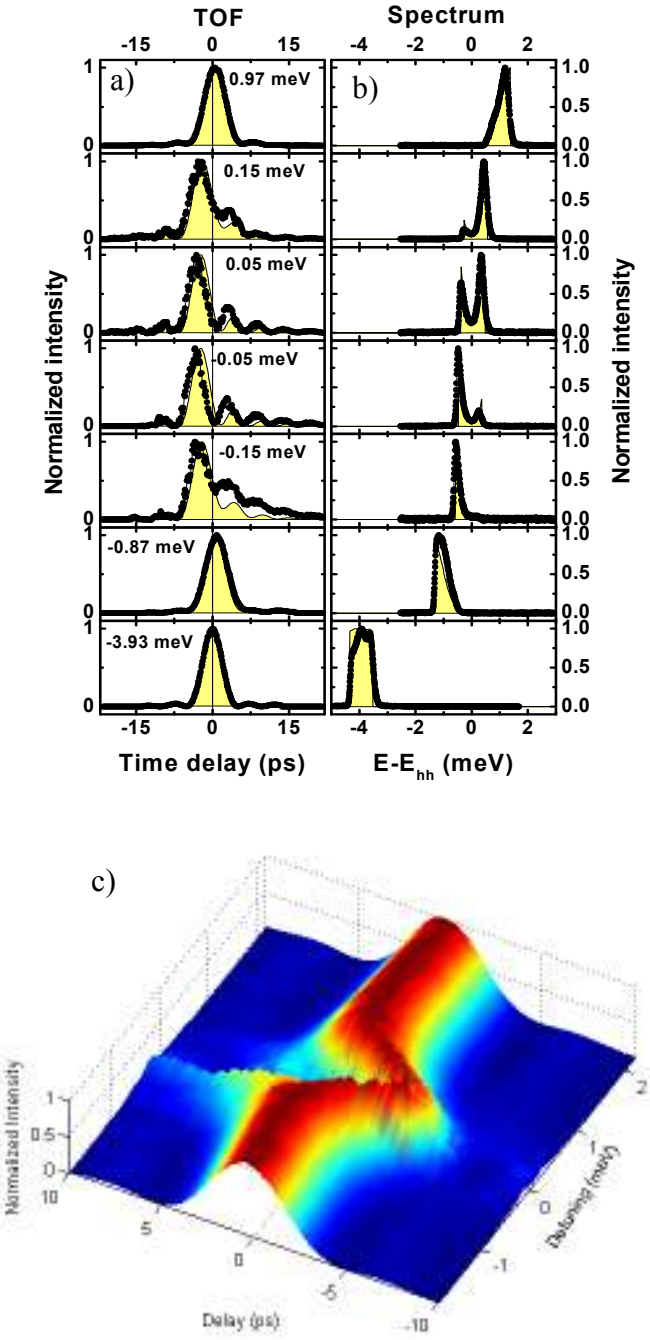

Figure 3.10 Experimental results and simulations. a) Individual TOF measurements (black) simulations (yellow shaded area) for the 40 quantum well sample and 0.84 meV spectral bandwidth incident pulse for different pulse-exciton detunings. b) Corresponding spectrum for TOF measurements (black dots) and simulations (yellow-shaded area). c) 3-D rendering of TOF measurements shown in parts a and b.

However, Fig. 3.10 shows substantial pulse breakup both theoretically and experimentally, consistent with Fig. 3.7e-h and the conclusions of Sec. 3.4.1. Figures 3.9c and 3.10c show pulse transmission from parts a and b of the figure plus additional data in a three dimensional format. The z-axis of the 3-D plot is the signal intensity which is normalized for convenience as x- axis is pulse-exciton detuning and y-axis is time.

3.5 Conclusion

We have undertaken an experimental study of pulse propagation in the vicinity of the resonance of multiple semiconductor quantum wells to understand the pulse propagation in spatial-dispersion-free structures.

As seen throughout this chapter, our measured delays are consistent with the group delay so long as newly developed figures of merit, $\Delta\omega_p << \Delta\omega_{GVD}$, $\Delta\omega\alpha_1$, $\Delta\omega_{\alpha 2}$, are satisfied. When this condition is not satisfied, however, the pulse delay can be accurately calculated by convolution with $\tau(\omega)$ (Eq. 3.3) and the pulse's transmitted spectrum. Theoretical simulations showed that when the full dispersion relation is taken into account, the individual time traces of pulses transmitted through the MQW structures can be modeled reasonably well. These simulations agree with our measurements for both narrow and wide pulse spectra.

CHAPTER 4: ALL-OPTICAL SWITCHING

As was mentioned in the first chapter, there is a high demand for optical counterparts of electronic components in order to take full advantage of fiber optic communication systems. The building blocks of circuitry logic such as AND, OR, XOR gates to perform logic operations on individual bits within a signal or header stream are missing, as are the optical switches which can be used in building some of the logic gates. For instance, one might need to check if two header signals match, since headers contain the information about the pulse, then process or reroute the signals accordingly. An optical switch can check mismatch between to header signals by cross-correlating, therefore acting as an AND gate.

Another application for an optical switch can be found in WDM (wavelength-division multiplexing) schemes. The switch can act as a temporal filter for long pulses in time. By gating the long signal pulse with a temporally short control pulse, one can acquire of a copy of the signal stream with same bit rate and shorter individual bits.

In Chapter 2 and Appendix A, some of the fundamental concepts of the semiconductor science were discussed. Here, some additional concepts and processes that are critical to the understanding of all-optical switching will be summarized. An all-optical switch will then be briefly described. Some basic figures of merit involved in comparing different optical switches will also be discussed. After this introduction, an all-optical switch demonstrated at low temperatures by Gansen et al. [42,43] will be reviewed as the experimental work shown in Chapter 5 is a continuation of his research. To describe what has been accomplished requires an understanding of his work.

Therefore some of his experimental results from his articles and dissertation will be shown. I would like to thank Eric Gansen, AIP, and UMI for permitting me to use these figures. In Chapter 5, a step towards bringing the all-optical switch closer to real-life application will be demonstrated.

4.1 Background and important concepts

4.1.1 Optical selection rules for excitons in quantum wells

Since light has been used to produce excitons in all-optical switching, it is important to understand the optical selection rules governing these transitions. In Fig 4.1, the optical selection rules [60] are summarized. The light propagates in the z-direction, normal to the plane of the MQW. The quantum numbers j and s represents the total angular momentum and spin. m_j and m_s are the projections of the angular momentum and spin in the z-direction, respectively. m_j and m_s are employed to label the states within which transitions occur. The four ground energy levels in Fig. 4.1 represent the valance bands for $k = 0$, two for heavy hole excitonic transitions with quantum numbers $j = +3/2$ and $m_j = +/-3/2$, and two for light hole excitonic transitions with corresponding quantum numbers $j = +3/2$ and $m_j = +/-1/2$. The quantum number for excited states which correspond to two bound exciton states in the conduction band are $j = +3/2$ and $m_j = +/-1/2$. Notice that $m_j = +/-3/2$ and $m_j = +/-1/2$ (heavy hole and light hole) states will be separated in MQW structures in contrast to bulk semiconductors due to the effect of confinement. Also, the spin quantum numbers $m_s = +/-1/2$ are marked for $s = +1/2$ in Fig 4.1.

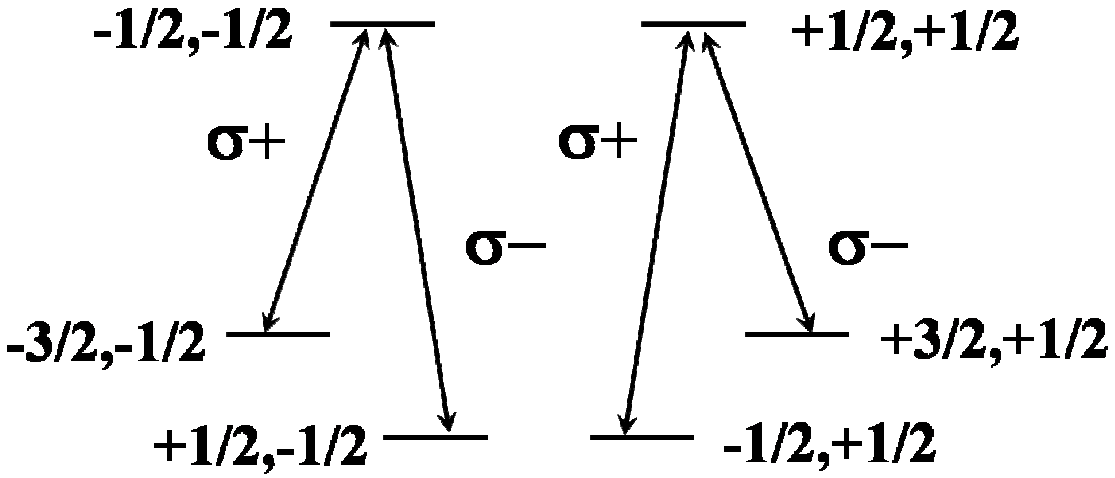

Figure 4.1 Diagram of the optical selection rules for the heavy hole and light hole excitons. The quantum numbers m_j and m_s are next to each state. Coupled right (σ+) and left (σ-) circular polarizations are shown next to each transition.

Note that each allowed transition responds to only one kind of circular polarization $\left(\sigma\mp = \frac{\hat{x} \mp i\hat{y}}{\sqrt{2}}\right)$ as the allowed transitions are shown in Fig 4.1. The right circularly polarized light, denoted as $\sigma+$, is coupled to transitions of heavy hole $m_j = -3/2$ to conduction band $m_j = -1/2$ and light hole $m_j = -1/2$ to conduction band $m_j = +1/2$; whereas left circularly polarized light, denoted as σ-, is coupled to heavy hole $m_j = +3/2$ to conduction band $m_j = +1/2$ and light hole $m_j = +1/2$ to conduction band $m_j = -1/2$ transitions. For example, right circularly polarized light coupled to the heavy hole transition energy will excite only a population of spin-down $m_j = -1/2$ carriers. In contrast, left circularly polarized light of the same frequency will excite a spin-up population of carriers. However, light coupled to the light hole transition

will not only excite a population of one spin polarization from the light hole transition, but the opposite spin from the heavy hole transition will be excited as well. This occurs because the heavy hole transition frequency is less than light hole transition frequency. Therefore, in contrast to bulk semiconductors, a highly polarized (nearly 100%) exciton population in multiple quantum well structures can be excited by coupling circularly polarized light only to heavy hole optical transition and by taking advantage of removed degeneracy between heavy hole and light hole transition.

4.1.2 AC and DC Stark effect

D.A.B. Miller et al. observed that as multiple quantum well structures were placed in a strong electric field parallel to the growth direction, the exciton absorption is shifted to lower energies [61]. As the strong external electric field is applied to the multiple quantum well structure, the electron states shift to lower energies while the hole states shift to higher energies. As a result, the absorption frequency is redshifted towards lower energies. At the same time, the peak value of absorption is decreased (bleaching) with some broadening of the exciton absorption linewidth. This results from the diminished oscillator strength due to decreased overlap of distorted wave functions. This effect known as the *DC Stark effect* or *quantum-confined Stark effect* (QCSE) since the electric field which applied to the multiple quantum well structure is a static field.

AC or dynamic or optical Stark effect (ACSE) refers to the shift (splitting) of atomic energy levels induced by strong resonant (non-resonant) optical field in atomic physics [62]. However, the ACSE in semiconductors is more complex than in atomic systems because of the extended and strong nature of the excitations in semiconductor materials [63]. In an ideal semiconductor, the regions below the n=1 exciton absorption

resonance are transparent. However, a strong pump laser tuned to this region, changes the optical properties of a semiconductor by inducing optical nonlinearities even though the laser is not absorbed and no real carriers are excited. “Virtual carriers” are created by the incident, intense, non-resonant optical field. In the ACSE, or optical Stark effect, the virtual excitation leads to a shift of the absorption line towards to higher energies (blue shift). This blue shift will vanish as soon as the non-resonant light field turns off. To describe the ACSE properly, one needs to solve related semiconductor Bloch equations numerically. For large detunings between the resonance and the non-resonant pump laser, the magnitude of the shift is directly proportional to the intensity of the pump laser and inversely proportional to the detuning magnitude [64].

The quasi-stationary (not for ultra-short fs lasers) ACSE in the low intensity regime can be described by shifts of exciton levels and oscillator strength changes due to phase–space filling as well as the anharmonic exciton-photon and exciton-exciton interactions. As the phase-space filling reduces the oscillator strength, the anharmonic exciton-photon and exciton-exciton interactions increase the binding energy and therefore the oscillator strength [52].

At high intensities of pulsed excitations, the many body effects need to be taken into account. Therefore, not only the pure Hartree-Fock terms but also the leading contributions of the correlation terms are needed to be considered when one writes the corresponding semiconductor Bloch equations. The many body interactions add further non-linearities to the excited system. When the many body effects turned off, there would be two independent subspaces of optical excitation due to spin selection rules which we discussed above.

For a semiconductor in which pumping and probing optical fields are co-circularly polarized, the first order many body Coulomb interactions and phase-space filling terms (the pure Hartree-Fock contributions) induces the blue shift, when the correlation terms induce a red shift which is comparatively smaller. Therefore the usual blue shift would be observed for same circularly polarized pump and probe pulses. However, when the pump and probe fields have opposite circular polarization, the Hartree-Fock contributions will vanish and only the correlation terms will survive. Therefore, a red shift of the absorption resonance will be observed [52].

Experimentally, Frohlich et al. [65,66] has seen the first evidence of ACSE in Cu2O, even though it was difficult to distinguish the shift because of the inhomogeneous broadening of the excitonic transition. Mysyrowicz et al. [67] and von Lehman et al. [68] observed the AC Stark effect in GaAs based multiple quantum well samples more clearly. For the duration of the strong pump pulse, Mysyrowicz et al. [67] observed a shift of the 1s exciton resonance towards higher frequencies (blue shift) along with the bleaching of the excitonic resonance. On the other hand, a pure shift without bleaching was demonstrated by Knox et al. [69] for low excitation intensities. Peyghamberian et al. [70] observed a shift in the absorption continuum of CdS (cadmium sulfide) to higher energy. Mysyrowicz et al. [67] explained his results with “dressed excitons”. Afterward, theoretical efforts of Chemla and Schmitt-Rink were based on virtual excitation which vanishes as the optical excitation ends. Zimmerman [71,72] also worked on the ACSE, and predicted a continuum and pure Stark shift. In addition, Chemla et al. reviewed the theory and experiments of ACSE with femtosecond pulses [63].

4.2 All-optical switching

4.2.1 Basic all-optical switch

An *all-optical switch* is a device that can modulate an optical signal pulse by employing an optical control pulse through the response of the switching material as seen in Fig. 4.2. For most all-optical switches, the signal pulse is weak and is used to carry information [42,43,73-79]. The control pulse is generally much stronger than the signal and induces the nonlinear response that the switch takes advantage of. Generally an all-optical switch is in the "off" state in the absence of the control pulse and is in the "on" state in the presence of the control pulse. However, it is possible to design a switch which works the opposite way ("off" in the presence of the control pulse). In addition, the switching material could be any material which gives a nonlinear response to light.

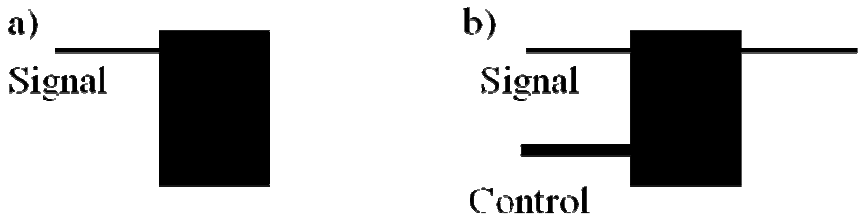

Figure 4.2 A basic diagram of an all-optical switch. a) The switch is "off" in the absence of the control pulse. b) The presence of the control pulse turns the switch to the "on" state.

To understand and compare the performances of different switches, there are some well known characteristics which will be discussed below. Furthermore, two of the most common all-optical switches will be described: Amplitude and Polarization switches.

4.2.2 Some engineering characteristics for all-optical switches

When a switch is off, it is ideally expected to have no output. However, in practice, there is always signal energy which leaks through the switch. This leakage can be harmful to the switch's performance if it is comparable to the energy of the signal beam during the "on" state. Consequently, our first important switch characteristic is the *contrast ratio*. The *contrast ratio* is the ratio of the transmitted signal energy through the switch when it is on versus when it is off. The contrast ratio is the measure of how effectively the on and off state of a switch can be distinguished from one another. Large contrast ratios indicate well defined on and off states. One way to improve the contrast ratio is to extinguish the incident signal energy efficiently when the switch is off.

Energy throughput of a switch is the fraction of incident signal energy that survives through the switch when it is in the "on" state. For an optical switch, it is possible to make a switch either in the transmission or reflection geometry. Thus, the energy throughput is the total reflectance or transmittance of the switch when it is on. A high energy throughput is always desirable for an optical switch.

The *switching energy* is the required amount of energy to turn the switch on each and every time it operates. A small switching energy is desirable.

The *switching time* is the total amount of time which is required to turn the switch on, and off. The time needed to turn the switch on is referred as the *rise or turn on time*. The amount of time required for the signal to die off is known as the *fall or turn off time*. The *recovery time* is the amount of time required for the switching material to fully recover and be ready for the next switching action. The *repetition rate* of the switch is

determined by the recovery time rather than switching time as the recovery of the material might take longer than switching time. Another important concept is the *optical bandwidth* of the switch. The optical bandwidth is given by the range of light frequencies over which an optical switch can operate.

Large contrast ratios, high energy throughput, fast switching time, small switching energy, broad optical bandwidth, as well as insensitivity to temperature fluctuations are all desired when designing a switch. However, some of these characteristics are in competition with one another and it is impossible to maximize all of them at the same time. For a polarization switch, using a thicker switching material can increase the contrast ratio by increasing the induced nonlinearities. However, as the switching material get thicker, the absorption of the material will increase and will eventually result in smaller throughput. It is often the case that one parameter can be optimized when designing a switch for a specific purpose, but always at the expense of one or more of the others.

4.2.3 Amplitude switches

Amplitude switches were very common among the earliest examples of all-optical switches. An example of the geometry of an amplitude switch is shown in Fig. 4.3. The signal and control pulses are spatially overlapped on the surface of a semiconductor switching material. The control pulse induces a change of the magnitude of the signal pulse by inducing a change of the absorption of the switching material. The induced change detected after the switching material is essentially the difference between the “on” and “off” state of the switching signal.

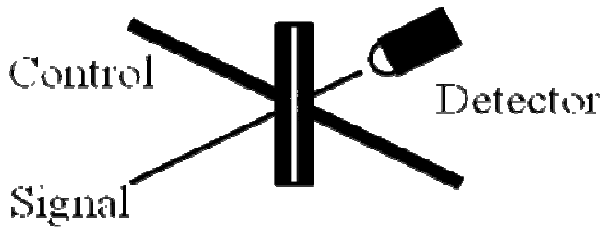

Figure 4.3 Schematic of an all-optical amplitude switch. The control pulse turns the switch "on"and "off" by changing transmissivity of the switching material.

The QCSE (section 4.1.2) is one of the mechanisms which have been utilized in amplitude switches [80-83]. These devices take advantage of a large shift and bleaching associated by QCSE. The multiple quantum well samples are placed in static electric fields which are either applied externally or built in internally (p-i-n structures). The control and signal pulses are tuned to red-shifted hh exciton resonance. In the off state of the switch, the signal is heavily absorbed in the absence of the control pulse. When it is incident, the control pulse excites electron hole pairs inside the wells. The excited carriers first bleach the absorption resonance through phase space filling and screening [84]. Then the carriers escape the wells either by tunneling or by thermal excitation, and the electrons and holes move to n and p regions due to electric field. The separated electron and holes produce an electric field which reduces the effect of QCSE, and blue shifts the absorption resonance. As a result, the induced bleaching and blue shift increases the transmission of the signal pulse and constitutes the on state of the switch.

Note that the referred amplitude switching studies in previous paragraphs and other studies in literature are mostly proof-of-principle measurements, and usually little or no effort has been made to optimize the referred switch. Therefore, only general

tendencies and characteristics about amplitude switches will be pointed out next rather than listing specific numbers.

Amplitude switches mostly take advantage of resonant excitation schemes. As a result they have generally lower switching energies compared to polarization switches employing non-resonant (below resonance) excitation schemes. As a direct result of induced shifts and bleaching, the throughput (more than 10% in most cases) of amplitude switches is generally higher than polarization switches. On the other hand, amplitude switches have poor contrast ratios (less than 100:1) because the signal beam's energy can not be extinguished efficiently in the off state of the switch. Switching time and repetition rate of amplitude switches generally depend on the switch design. Since real carriers (as opposed to virtual ones) are mostly involved in amplitude switches, switching times vary from 10s to 100s of picoseconds. Also carrier accumulation might be a limiting factor for the repetition rate.

4.2.4 Polarization switch

All-optical polarization switches are based on similar principles as all-optical amplitude switches. However, in this case, the signal pulse's polarization state is changed instead of its magnitude. The only difference in the design of the polarization switch is the addition of a crossed polarizer-analyzer pair as seen in Fig. 4.4. A polarizer which will yield a linearly-polarized signal pulse is inserted in to the beam path before the switching material. The analyzer placed after the switching material (MQW sample in our case) rejects the signal pulse in the absence of the control pulse. Therefore, no signal, or a very small amount of leakage, is detected in the "off" state of the switch. As the control pulse becomes incident on the switching material, it produces non-linearities such

as circular dichroism and birefringence. Since the linearly-polarized signal pulse is composed of circular polarization components, the circular induced non-linearities will affect each circular component differently. The linear polarization of the signal pulse will be modulated (i.e. it will be rotated and will become elliptical). Therefore more of the signal pulse will pass through the analyzer, and the switch would be "on".

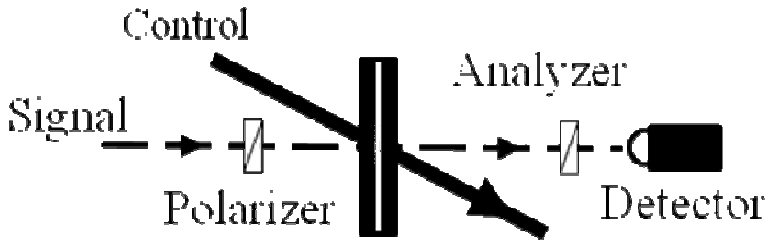

Figure 4.4 Schematic of an all-optical polarization switch. The control pulse turns the switch "on"and "off" by changing the signal pulse's polarization state.

In amplitude switches throughput and contrast ratio are directly related. If the throughput goes down, the contrast ratio decreases as well. As was mentioned in the previous section, the reason amplitude switches have poor contrast ratio is the inefficiency of extinguishing the off state of the switch. However, a pair of commercially-available broadband polarizers can extinguish the incident signal pulse better than 10^5:1 in the absence of the control pulse for a polarization switch. Therefore a small change in the polarization state will correspond to low throughput and relatively high contrast ratio in polarization switches. As a result it is still possible to get impressive contrast ratios for relatively short MQW structures [42,43] even though the induced change of the polarization state is not large and the throughput of the switch is low.

The recovery times are very different for polarization switches based on real and virtual carriers. The virtual carriers produced by below-resonance excitation disappear after the control pulse exits the sample. Therefore, the recovery of the switching material is nearly instantaneous, and it is only limited by the pulsewidth of the control pulse which could be hundreds of femtoseconds. However, the real carriers produced by resonant excitation may need nanoseconds to recombine. As a result, the recovery time of the switch will be much longer. Using the switch without waiting for recovery will cause accumulation of carriers which will decrease the performance and will cause heating. The switching time of the switch will again depend on the detuning of the excitation. A virtual excitation below resonance will have a very fast switching rate compared to on- or above resonance excitation because of the lack of the real carriers. Consequently, the only limiting factor will be the width of the control pulse [85.86]. Therefore, the switching time and the repetition rate of a polarization switch will be based on the design.

4.3 Discussion of spin-polarized virtual carrier switch

The polarization switch discussed below was first demonstrated by Gansen et al. [42,43], with theoretical description given by Rumyantsev et al. [79], and it is based on the near-resonant excitation of spin-polarized virtual carriers. The control pulse is tuned near but below the 1s heavy-hole absorption resonance to excite virtual carriers. Hence, the population of spin polarized virtual carriers exists only when the control beam is present within the switching material. Therefore, the switching time is only governed by the cross-correlation of signal and control beams, not by the spin relaxation time or the carrier recombination time. Consequently, the switching times can be reduced to femtoseconds from a nanosecond scale.

4.3.1 Basic operation of spin-polarized virtual-carrier (SPVC) switch

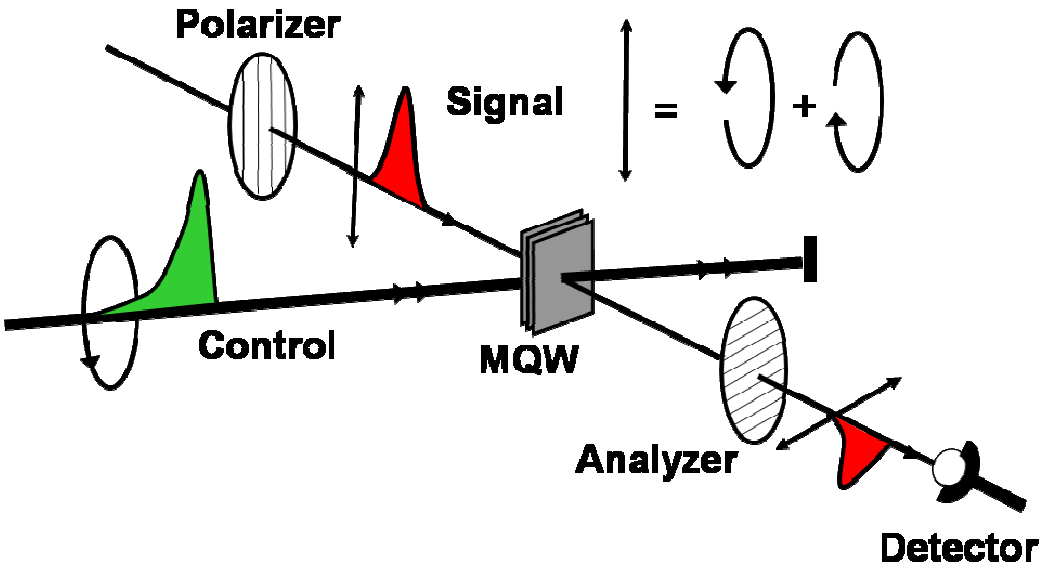

Figure 4.5 Schematic of an all-optical polarization switch. The control pulse turns the switch "on" and "off" by taking advantage of the spin selection rules and virtual excitation of spin-polarized population of a carriers in the MQW sample.

As illustrated schematically in Fig. 4.5, the all-optical polarization switch previously demonstrated by Gansen et al. [42,43] is designed to extinguish the pulses of the signal beam in the "off" state of the switch. The switching material is sandwiched between two broadband polarizers which are oriented to reject the linearly-polarized signal pulse when the pump is not present. In this state, only a very small amount of energy from the signal beam leaks through; depending on the extinction ratio of the polarizers (~5×10^{-5} in this case).

To turn the switch on, Gansen et al. [42,43] took advantage of the spin selection rules for the 1s heavy-hole excitonic transitions in a multiple quantum well structure as was discussed in section 4.1.1. When the right-circularly-polarized control pulse is incident on the MQW structure, it will inject a spin-polarized virtual population of carriers only with one type of spin (spin-down) if the 1s heavy-hole exciton absorption resonance is assumed to obey the usual circular selection rules summarized in Fig 4.1. Note that the control pulse was detuned [42,43] below the heavy hole absorption and shaped to minimize overlap with the heavy hole resonance in order to minimize the production of real carriers, as seen in Fig. 4.6c. Even though the excitation of real carriers is minimized or extinguished, optical properties of MQW structure can be manipulated through the AC Stark effect. The strong circularly-polarized control pulse will bleach and blue shift the absorption coefficient and index of refraction even though the control pulse is non-resonant. However the right-circularly-polarized (σ^+) control pulse will only excite spin-down electrons. On the other hand, the signal pulse is linearly polarized, thus it is composed of equal amounts left- (σ^-) and right- (σ^+) circularly-polarized components. Therefore, the σ^+ component of the signal will see the blue shifted and bleached absorption coefficient and index of refraction, whereas the σ^- will see a nearly unmodified absorption coefficient and index of refraction. When the signal exits the sample, it will become elliptically polarized and rotated, hence a bigger fraction of the signal beam will pass through the second polarizer as seen in Fig. 4.6a. This will be the "on" state of the switch [42,43,78,79].

Another advantage of this arrangement is that the excitation of the light hole band will be much smaller compared to the heavy hole excitation due to increased detuning

between light hole and spectrally-shaped control pulse (detuning between heavy hole transition and control pulse ~13 meV; between light hole transition and control pulse ~20 meV for Fig. 4.6). Therefore, in the absence of many-body interactions, the heavy hole exciton can be viewed as two independent 2-level systems (in Fig. 4.6b), because the contribution from the light hole exciton will be much smaller due to larger detuning and smaller oscillator strength.

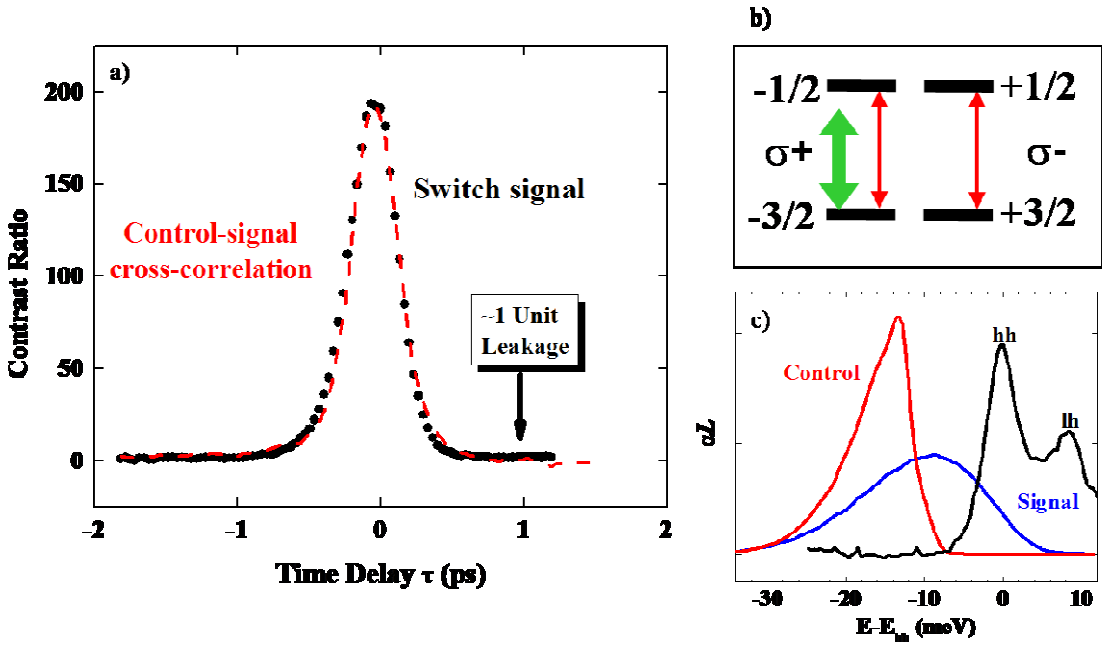

Figure 4.6 Experimental configuration for the SPVC switch measurements at 80 K. a) The switch signal (black dots) and normalized cross-correlation of probe and reference pulses (red dashes). b) Diagram of the control (green) and the signal (red) pulses' coupling to states. c) The spectra of the control (red), and signal (blue) pulses with respect to the 1s hh exciton absorption resonance [1,2].

The MQW structure used for these measurements has 40 periods of 10-nm-wide GaAs wells separated by 10-nm-thick $Al_{0.3}Ga_{0.7}As$ barriers. It was grown on a [001]-oriented GaAs substrate, which was removed to allow for transmission measurements.

An amplified Ti:Sapphire laser system generates both signal and control pulses. The signal pulses are about 150 femtoseconds (full-width at half-maximum, FWHM) temporally, about 21 meV spectrally, and are equivalent to the original pulses leaving the source. However the control pulses are spectrally filtered by the use of a pulseshaper as seen in Fig. 4.6c, and they are about 450 femtoseconds wide, as shown in the cross-correlation of signal and pump pulses in Fig. 4.6a. The control and signal pulses are spatially overlapped on the surface of the MQW sample with a variable time delay τ introduced between them. The signal pulses are tuned very slightly below 1s hh exciton absorption resonance whereas the control pulses are tuned 13 meV below the 1s hh exciton absorption to ensure the excitation of virtual carriers. Recall that when the signal pulses are linearly polarized, the control pulses are circularly polarized. The sample is cooled to approximately 100 K. For detection, the signal beam is modulated via a mechanical chopper and is synchronously detected as a function of τ by using a lock-in amplifier.

As shown in Fig. 4.6a, the switch demonstrated by Gansen et al. [42, 43] has a relatively high contrast ratio of 200:1 and very fast recovery time of 450 femtoseconds. The temporal profile of the switch signal is compared to the cross-correlation of the control and signal pulses; they are basically on top of each other. The real switch signal is skewed slightly towards negative delays because of the memory effects in the sample [87], but here it is drawn as a guide to the eye. This similarity between cross-correlation and switch signal as well as the 1 unit of leakage is an indication that switch is based on virtual carriers and there is no serious carrier accumulation between pulses. However, one needs to ensure that AC Stark effect is solely responsible for the switching action and

there is no real carrier accumulation after the switch is turned off. Therefore, Gansen et al. [42,43] removed the analyzer after the sample from the signal beam path. A quarter-wave plate was inserted to the signal path before the MQW sample to get a circularly-polarized probe (or signal) and the detector was replaced with a spectrometer. The signal pulse was spectrally resolved to observe changes of 1s hh exciton absorption for low pump irradiance of 12 MW/cm^2 (fluence 4.4 μJ/cm^2) as the control and signal pulses were overlapped in time (τ=0). The results for same (filled circles) and opposite circular (open circles) polarization of the control and signal beams are shown in Fig 4.7.

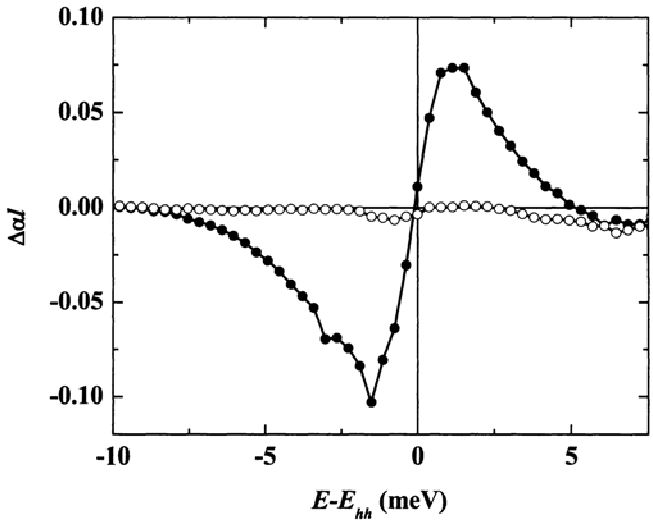

Figure 4.7 The change of the absorption profile for same (filled circles) and opposite (empty circles) circular polarization of control and signal pulses for low control irradiance of 12MW/cm^2 (fluence 4.4 μj/cm^2)at τ=0.(Fig.6.3 from [87]).

When the control and signal pulses are overlapped in time, a blue shift and a small amount of bleaching for the 1s hh exciton absorption is observed for the same circular polarization. There is no appreciable change of the 1s hh exciton absorption for opposite

circular polarization. These results are signatures of the AC Stark effect. However the control irradiance is about 450 MW/cm^2 (fluence 165 μJ/cm^2) for the switching data [42,43] shown in Fig. 4.6, a much higher irradiance than in Fig. 4.7. For the coincident signal and control pulses (τ=0 ps), the only apparent signature is heavy bleaching of the 1s hh exciton absorption for the same circular polarization (filled circles) as seen in 4.8a [87]. For opposite circular polarization (open circles), the bleaching and the blue shift of the 1s hh exciton absorption is observed as shown in Fig. 4.8a.

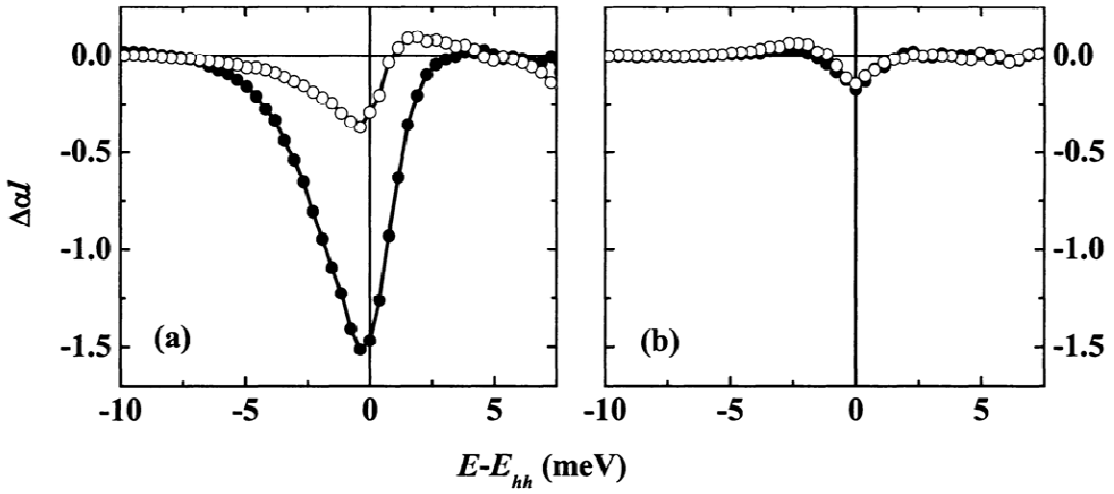

Figure 4.8 The change of the absorption profile for same (filled circles) and opposite (empty circles) circular polarization of control and signal pulses for control irradiance of 450 MW/cm^2 (fluence 165 μj/cm^2) at (a) τ=0 and (b)τ=4.8 ps (Fig.6.4 from [87]).

At positive delays (after the control pulse has left the sample, τ=4.8 ps is seen in Fig. 4.8b), one can see a small but measurable change of the 1s hh exciton absorption profile for both the same (filled circles) and opposite (open circles) circular polarization, an indication that a population of real excitons has been created. In addition, the

magnitude of the change seen in both the same and opposite circular polarizations is very similar which suggests the interband exciton polarization has already dephased. Note that spin relaxation time is much longer than 4.8 ps.

Hence, these observations at positive time delays ensure that the changes induced by the control pulse are mostly “virtual”; they are gone after the control pulse left the sample. Therefore, it can be said that the switching mechanism is based on the spin-polarized virtual excitation.

CHAPTER 5: NEAR-ROOM TEMPERATURE ALL-OPTICAL SWITCHING

As it has been mentioned in the Chapters 1 and 4, optically addressed polarization switches are a part of today's growing interest in spin-based technologies. These switches make use of spin-polarized carriers in semiconductor multiple quantum wells (MQWs) and they have been shown to operate at high speeds and with relatively high contrast ratios. These devices [42,43,73-79] operate by using a circularly polarized control pulse to inject a spin-polarized population of carriers in a MQW and using this spin-polarized population to change the polarization state of a weaker signal pulse as was discussed in the Chapter 4. The change in the signal polarization is subsequently converted to a modulation of the signal amplitude by using additional polarization sensitive elements and persists as long as the spin-polarized population exists in the sample. In conventional spin-based switches [73-78], the carriers are generally excited resonantly by tuning the control pulse to the 1s heavy hole (hh) exciton absorption resonance. In many of these devices, the lifetime of the excited carriers is long compared to the time over which they maintain their spin. Therefore, it is the spin relaxation time of the carriers that determines the turn-off time of the switches. On the other hand, the complete recovery of the switching materials is limited by the time that it takes the carriers to recombine or to be swept out by an electric field. The accumulation of carriers between pulses can limit the repetition rate of these devices.

A coherent polarization switch based on the below-resonant excitation of *spin-polarized virtual carriers* (SPVC) that does not suffer from these same limitations has been investigated, both experimentally [42,43] and theoretically [79]. As Gansen et al.

[42,43] demonstrated and as I discussed in the Chapter 4, by tuning the control pulse near but below resonance, thereby taking advantage of the spin-dependent nonlinearities associated with virtual carriers, femtosecond switching times and relatively high-contrast modulation could be achieved without relying on fast spin relaxation times and without significant carrier accumulation. However, those switch measurements were conducted with the MQW cooled to a temperature of ~100 K. Cooling the switching material adds complexity to the device, which is undesirable for practical applications. Here, we investigate the near-*room-temperature* operation of the SPVC switch and study the temporal dynamics of the spin-polarized carriers excited in the MQW during its operation.

5.1 Experimental details

The SPVC switch geometry is illustrated schematically in Fig. 5.1a. The switch is composed of a MQW positioned between two broadband polarizers that are oriented to reject the signal pulse in the absence of the control. The MQW is the same sample as was used by Gansen et al. [42,43] for the previous low temperature studies of the SPVC switch [42,43,79] reviewed in the Chapter 4. It consists of 40 periods of 10-nm-wide GaAs wells separated by 10-nm-thick $Al_{0.3}Ga_{0.7}As$ barriers, grown on a [100]-oriented substrate, which was removed to allow transmission measurements. The control and signal pulses are generated by an amplified Ti:Sapphire laser system and are spatially overlapped in the MQW with a variable time delay τ introduced between them. The ~145 fs full-width at half-maximum (FWHM) incident signal pulses (~21 meV in spectral width) are tuned below the 1s hh exciton absorption resonance by ~4 meV by adjusting the sample temperature to ~267 K (see Fig. 5.1b).

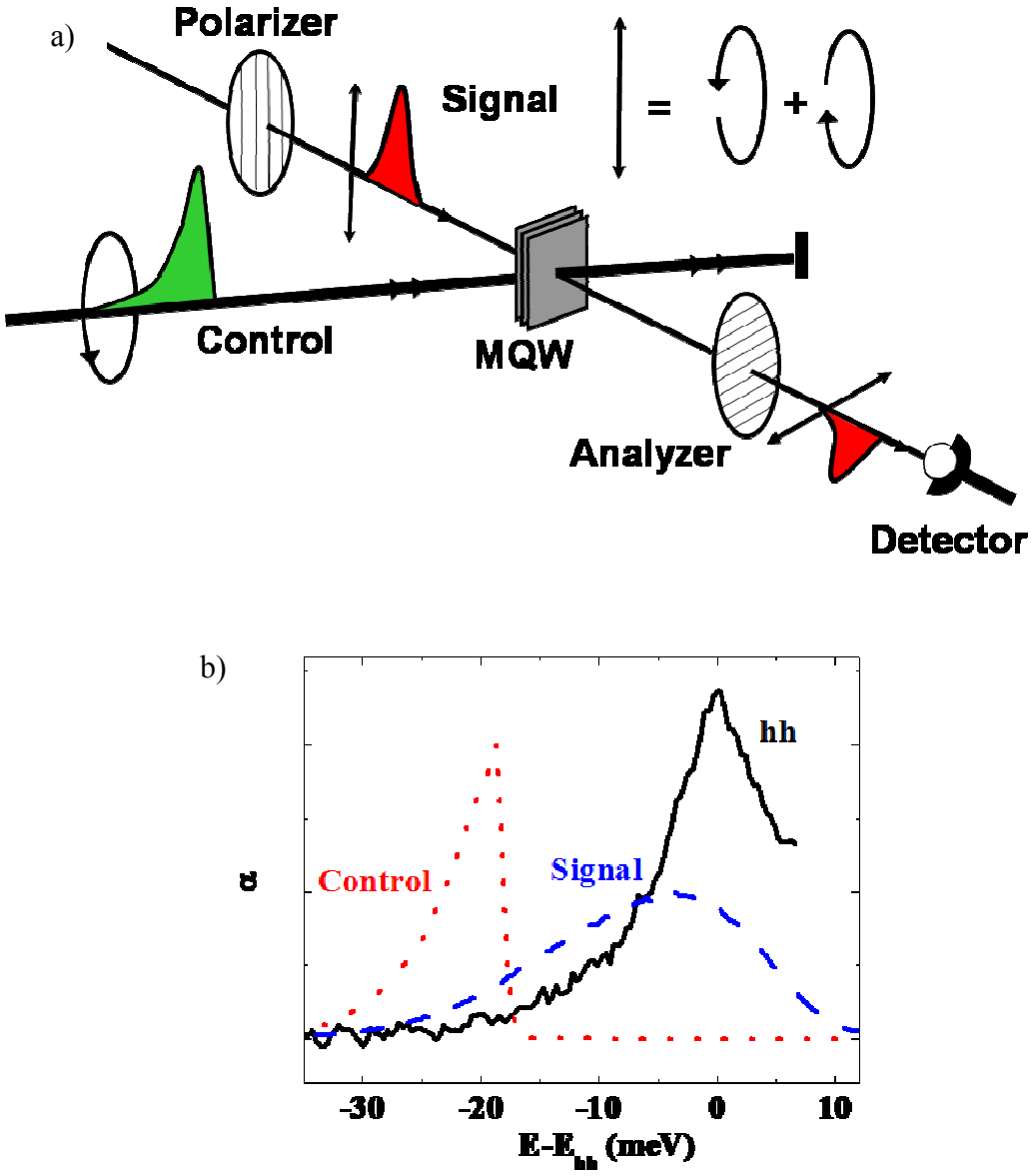

Figure 5.1 Experimental configuration for the SPVC switch measurements. a) Basic schematic of experimental setup. b) The graph shows the tuning of the control (red dots) and signal (blue dashed line) spectra relative to the 1s hh exciton absorption resonance (black solid), where the energies are referenced to the hh exciton energy E_{hh}.

For convenience, we chose to fix the laser wavelength and tune the band gap by controlling the sample temperature, rather than tuning the laser wavelength and fixing the

sample temperature—otherwise there is no significance to the relatively small deviation from room temperature. The spectrally-filtered, circularly-polarized, ~445 fs control pulses are tuned ~19 meV below the hh exciton absorption resonance to suppress the resonant excitation of carriers. The signal beam is modulated by using a mechanical chopper and is synchronously detected as a function of τ using a lock-in amplifier.

5.2 Switch performance

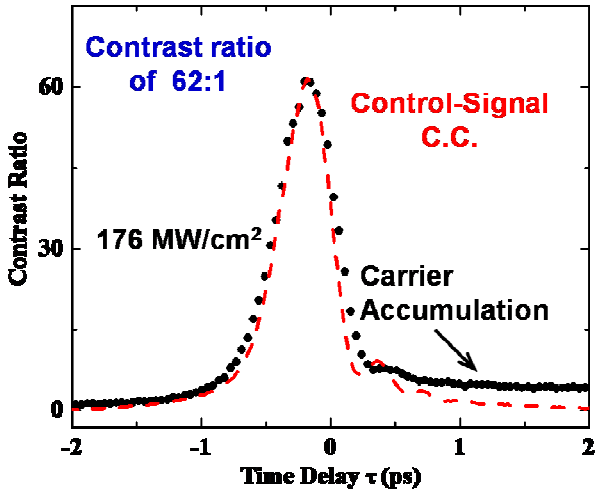

Figure 5.2 Contrast ratio (black filled circles) of the switch as a function of time delay τ for a control irradiance of ~176 MW/cm^2 . The time-resolved control pulse (red dashed line), shifted by ~180 fs to negative delays, is shown for comparison.

The near-room-temperature SPVC switch performance is illustrated in Fig. 5.2. Here, the contrast ratio (or on-off ratio) is plotted as a function of time delay τ. The time-resolved control pulse (measured using up conversion in a second harmonic crystal) is also shown for comparison. The switching time [i.e., the time required for the device to turn on and off] is~540 fs (FWHM), it is pulse width limited, and a peak contrast ratio of

~62:1 is obtained for a control irradiance of ~176 MW/cm^2 (fluence ~80μJ/cm^2). Also notice that the contrast ratio does not perfectly return to unity at positive delays. As we will discuss below, this offset is the result of the accumulation of a small number of spin polarized carriers.

The spectrally-resolved contrast ratio and throughput are shown in Fig. 5.3 for τ=-180 fs, which corresponds the peak contrast ratio in Fig. 5.2. The spectrum of the incident signal pulse (red solid line) is also included in Fig. 5.3 for comparison. The switch exhibits a peak contrast ratio and throughput of ~115:1 and ~0.4%, respectively, and an optical bandwidth of ~12 meV (or ~3 THz, FWHM). The peak contrast ratio and throughput occur near the hh exciton peak, and the bandwidth is determined by the width of the hh excitonic resonance.

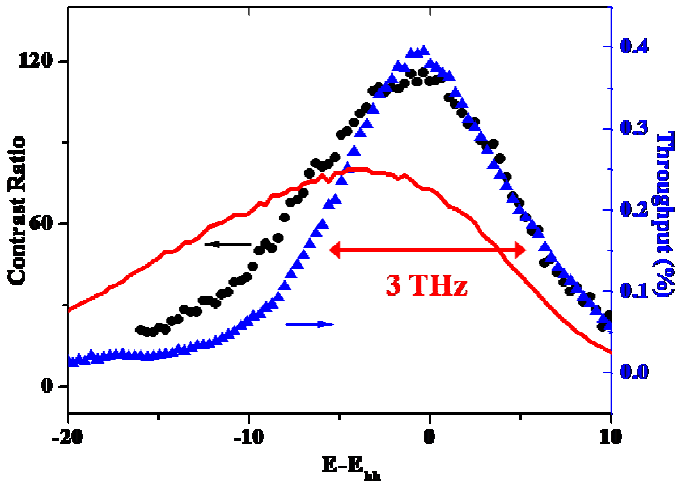

Figure 5.3 Spectrally resolved contrast ratio (black circles) and throughput (blue triangles) for τ=-180 fs. The incident signal spectrum (red solid line) is plotted for comparison.

The overall speed of the SPVC switch (i.e. the maximum allowed incident bit rate) will be limited by the slower of the switching speed and the inverse of the optical bandwidth. As illustrated in Fig. 5.2 and 5.3, the switching speed and optical bandwidth are determined by two independent quantities: the temporal width of the control pulse and the spectral width of the exciton, respectively. Clearly, in the proof-of-principle experiments shown in Fig. 5.2, the control pulse width and the signal pulse width were not chosen to optimize device switch performance, but for spectroscopic convenience. The signal bandwidth is shifted with respect to, and is not tailored to match, the optical bandwidth, and the control pulse width unnecessarily restricts the device speed. The data suggest that we can significantly improve the contrast ratio and throughput by shifting the center frequency of the signal spectrum and by reducing its width to match the optical bandwidth (~12 meV) and that we can simultaneously increase the switching speed by reducing the control pulse temporal width to a corresponding spectral bandwidth of ~12 meV (same spectral bandwidth as the signal). However this device improvement does not come without a price. For example, the increase in control pulse bandwidth will either (i) result in an increase in the spectral overlap between the control and the hh (in which case there will be a concurrent increase in carrier accumulation from single-photon absorption) or (ii) the center frequency of the control will need to be shifted farther from the hh resonance (which will require a higher switching energy).

5.3 Low–temperature versus near-room-temperature operation of SPVC switch

The near-room-temperature operation of the SPVC switch portrayed in Fig. 5.2 is in some respects qualitatively similar to the low-temperature operation reported

previously [42,43,79]. When present, the circularly-polarized, below-bandgap control pulse excites a virtual population of spin-polarized carriers through the optical Stark effect, which produces a circular birefringence and dichroism in the sample [43]. Consequently, when the linearly-polarized signal pulse overlaps the control pulse in the sample, the signal polarization becomes elliptical and is rotated, and a portion of the signal pulse is passed by the output polarizer.

There are, however, fundamental differences between the low and higher temperature operation of the SPVC. At 80 K, the interband dephasing time is longer than the widths of the fs pulses that were used in the experiments, and consequently, coherent emission played an important role in determining the switch dynamics, for example, leading to a skewing of the peak on-off ratio toward negative delays [43,79]. Near-room-temperature, the opposite is true: the dephasing time is short compared to the signal and control pulse widths, and we do not expect coherent emission to be important after the pulses have exited the sample. The increased scattering at the higher temperature will also reduce the peak of the excitonic resonance and broaden it (such that the area remains approximately constant in the absence of saturation). This excitonic broadening improves (increases) the optical bandwidth; however, it also increases the overlap between the excitonic resonance and the control pulse spectrum, leading to an increased production of real carriers by single-photon absorption. In addition, the concurrent reduction in the excitonic peak at higher temperatures results in a decrease in the contrast ratio.

We investigate the circular dichroism induced by the control during near-room-temperature operation of the SPVC switch by removing the output polarizer and performing spectrally-resolved differential transmission measurements using control and

signal pulses that have the same and opposite circular polarizations. Results are shown for three fixed time delays in Fig. 5.4. First, notice that for coincident signal and control pulses (Fig. 5.4b) pronounced absorbance changes are produced in the vicinity of the hh absorption resonance when the two pulses have the same circular polarizations, but the changes are much smaller when opposite circular polarizations are used. These results confirm that the control excites a highly spin-polarized population of carriers and are consistent with the effective polarization switching observed near τ=0 in Fig. 5.2.

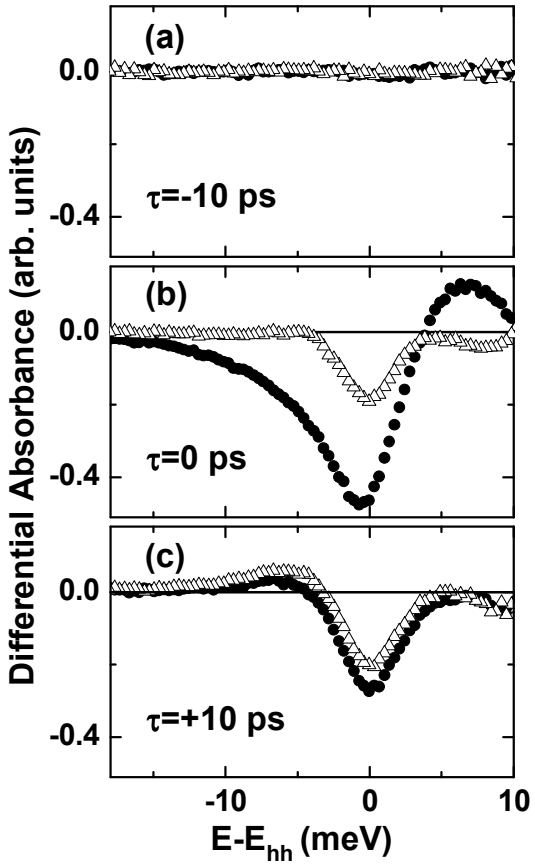

Figure 5.4 The differential absorbance [difference, $\Delta\alpha l$, with and without a right circularly polarized control pulse (σ^+)] for signal pulses that have the same (σ^+, filled circles) and opposite (σ^-, open triangles) circular polarizations as the control for (a) τ=-10 ps, (b) τ=0 ps, and (c) τ=+10 ps.

By comparison, notice that for small positive and negative delays ($\tau=\pm10$ ps) in Fig. 5.4 there is very little difference between the absorbance changes observed for control and signal pulses with the same and opposite circular polarizations, consistent with the absence of significant polarization switching produced for positive and negative time delays in Fig. 5.2. In addition, notice that while no absorbance changes are apparent when the signal pulse arrives before the control pulse ($\tau=-10$ ps), appreciable changes persist for positive delays ($\tau=+10$ ps), indicating that a significant number of carriers remain after the control pulse has exited the MQW.

Because the spectral absorbance changes for the same and oppositely circularly polarized signal and control pulses are approximately the same in shape and magnitude for $\tau=+10$ ps, it is tempting to conclude that the spin relaxation time of the residual carriers left by the control pulse is less than 10 ps — a time short compared to those previously measured (>50 ps) for GaAs/AlGaAs MQWs [88,89]. This apparent discrepancy is resolved by performing spectrally-integrated differential transmission, again using signal and control pulses with the same and opposite polarizations, as shown in Fig. 5.5. The difference between the two sets of measurements is a direct measure of the circular dichroism.

Two time scales are of interest. For time delays such that the signal and control pulses overlap (inset, Fig. 5.5), the dirchroism is large, and it adiabatically follows the intensity profile of the control pulse, consistent with a spin-polarized virtual excitation. On longer time scales, the circular dichroism decays with a characteristic time of ~70 ps, consistent with reported electron spin relaxation times (as defined in Ref. 88) for similar MQW samples and experimental conditions. These differential transmission

measurements are consistent with the time-resolved contrast ratio of the SPVC switch shown in Fig. 5.2.

5.4 Conclusion

In summary, we have investigated the near-room-temperature operation of an optically addressed polarization switch based on the virtual excitation of spin-polarized carriers. We have demonstrated that the device turns on and off in a time dictated by the control pulse width (~540 fs for the pulses used here), exhibits a contrast ratio of >18 dB, and an optical bandwidth of ~3 THz at a switching fluence of ~80 μJ/cm^2.

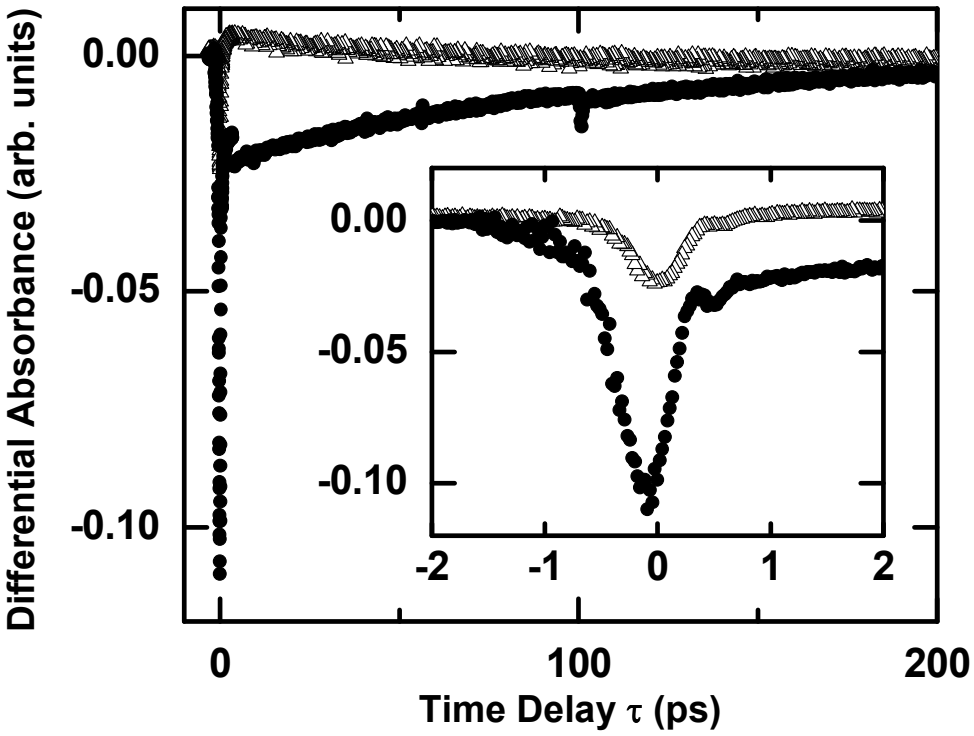

Figure 5.5 The spectrally-integrated differential absorbance as a function of time delay for signal pulses that have the same (σ^+, filled circles) and opposite (σ^-, open triangles) circular polarizations as the control pulse (σ^+). The inset magnifies the data near τ=0 ps.

We also found, however, that there is a price to pay for operating the switch near room temperature, in that the device exhibits increased carrier accumulation and decreased contrast and throughput in comparison to our original low temperature (~100 K) measurements [42,43,79]. The residual carriers produced by the control pulse lose their spin-polarization in ~70 ps and recombine on ns time scales. The circular dichroism associated with the residual carriers, however, does not contribute substantially to the switch signal, and additional suppression of these carriers is expected by increasing the control detuning. Moreover, we want to emphasize that this is an unoptimized device and that, in addition to reduced carrier accumulation, significant improvements to the contrast ratio and throughput of the switch should be possible by using more wells and by optimizing the control detuning and the spectral content of the signal pulses.

CHAPTER 6: MOLECULAR BEAM EPITAXIAL GROWTH OF BRAGG-SPACED QUANTUM WELL STRUCTURES

Resonant photonic bandgap (RPBG) structures are an unusual kind of photonic band gap material. In the conventional photonic band gap materials, such as dielectric mirrors or photonic crystals, material resonances are spectrally far away from the photonic bandgap. On the other hand, RPBG structures have material resonances which are degenerate or nearly resonant with the photonic band gap frequencies (or Bragg frequency in our case) of the structure. This degeneracy of two different resonances will be discussed below in more detail. Examples of RPBG structures include structures with two-level dopant atoms embedded uniformly [90,91] or periodically in alternating layers of a dielectric mirror or photonic crystal [92-94].

Another example is a structure consisting of ring resonators spaced with Bragg periodicity [95]. Linear and non-linear properties of the resonant photonic bandgap structures have been studied in several theoretical papers and exhibit properties which make them attractive for all-optical device applications such as optical buffering and all-optical switching [46,77,96,97]. However, no resonant photonic bandgap structures have been experimentally realized except Bragg-spaced quantum wells (BSQWs), and even BSQWs are very difficult to fabricate.

In this chapter, we will focus on a most basic RPBG consisting of quantum wells with a single pronounced exciton resonance spaced with Bragg periodicity. After a brief introduction of Molecular beam epitaxy (MBE), BSQW structures will be introduced. The challenges and results of MBE growth of BSQWs will then be presented. Additionally, slow light measurements in our BSQW's will also be presented.

6.1 Molecular Beam Epitaxy

Molecular beam epitaxy is a technique that can be used to grow semiconductor hetero-structures, such as (multiple quantum wells) MQWs, which are constructed from alternating layers of different semiconductors. A schematic of a MBE growth chamber is shown in Fig. 6.1. The first step of this type of growth is to evaporate or sublimate the components of the semiconductor structure which we want to fabricate. In their vapor form, these materials will deposit on the surface of a substrate (much like spray painting at the atomic level). At growth temperatures, the atoms on the heated surface of the substrate move around so that they arrange themselves in a crystalline form rather than amorphous layers. Since this is a very slow growth process (on the order of an atomic monolayer per second, or a couple angstroms per second), and unintentional impurities are not welcome, this process is usually realized under an ultra-high vacuum of about 10^{-9} to 10^{-11} Torr.

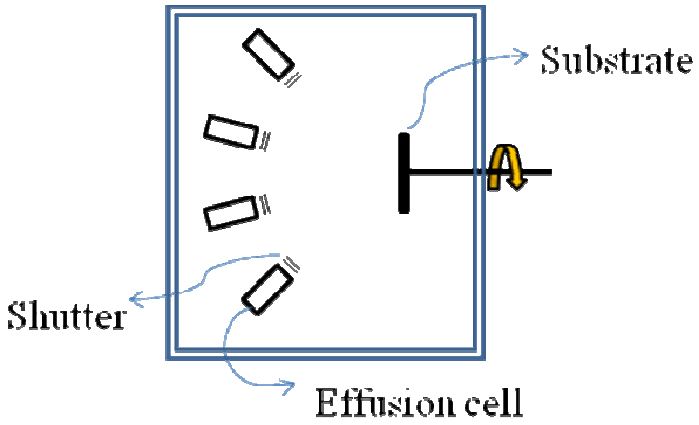

Figure 6.1 Schematic of a MBE growth chamber. Materials are evaporated from the effusion cells and the flux through these cells can be controlled with computerized shutters and cell temperature. The substrate is attached to a rotating platform to homogenous layer thickness across the wafer that might otherwise result from angular variations in material flux.

The temperature of the effusion cells and the shutters in front of the cells are computer-controlled. By changing the temperature of the effusion cells as well as opening and closing the shutters, the amount and layering of materials deposited on the substrate can be controlled. This fabrication process offers ultimate precision in layer thickness less than 1 monolayer of material. By taking advantage of computerized components, growth recipes can be written before the growth begins and the entire process can be completed with minimum operator involvement.

6.2 Bragg-spaced quantum wells

The Bragg-spaced quantum well structures may be characterized by two distinct frequencies: the frequency of the 1s hh exciton absorption resonance (ω_X), and the fundamental Bragg frequency ($\omega_B = c\pi / n_b a$) where c is the speed of light, n_b is the background index, and a is the spacing between two periodic quantum wells. Similar to the electronic bandgap in semiconductors, the Bragg periodicity in the index of refraction results in a photonic bandgap, a band of energies where photons are not allowed because there are no photonic states available. Unlike the electronic bandgap, there is an almost flat band (when $\omega_B \approx \omega_X$) in the middle of the two band edges of the photonic band structure as shown in Fig. 6.2. This intermediate transmission band is analytically expressed as in Ref. 46,

$$\cos(Ka) = \cos(qa) + \frac{\Gamma}{(\omega + i\gamma) - \omega_X}\left(\frac{\omega}{\omega_X}\right)\sin(qa) \tag{6.1}$$

where ω is angular frequency, $q = n_b\omega / c$ and K are the photon and polariton wave vectors, respectively, Γ is the radiative decay rate, and γ is the dephasing rate. For most

of the energies, the second term in the Eq. 6.1 is small, so the dispersion relation is linear ($\cos(Ka) = \cos(qa)$). However when $\omega = \omega_B \approx \omega_X$, the second term tends towards infinity and K becomes an imaginary number which means photons with real wave vector are not allowed. That is the photonic bandgap which was discussed above. Another demonstration of the photonic bandgap is the total reflection of the frequencies within the photonic bandgap.

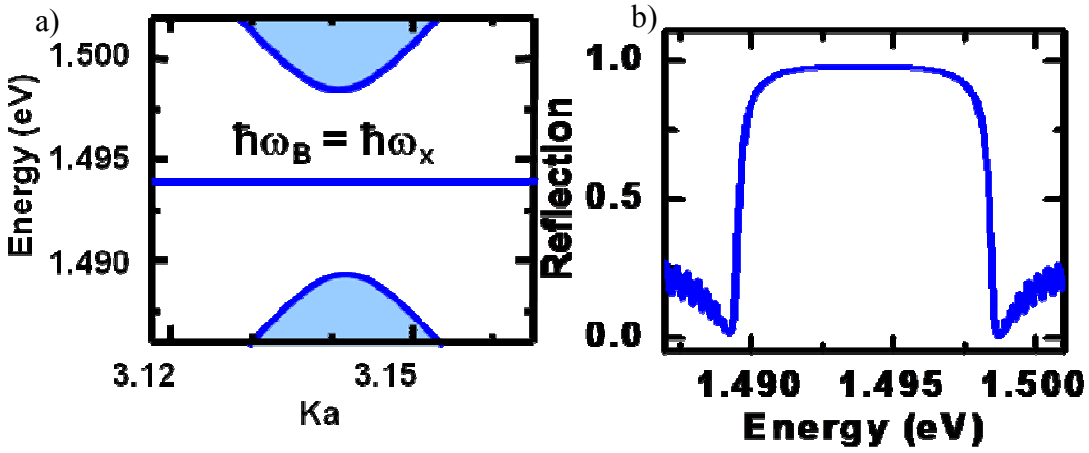

Figure 6.2 Simulated photonic band structure of BSQW structure [48] for $\Delta\omega = \omega_B - \omega_X = 0$ meV (a) and reflection band (b).

The width of the intermediate band is linearly proportional to the detuning between ω_X and ω_B. For small detuning, the intermediate band spreads and covers the area between the two resonances. As a result, light can propagate through for the frequencies corresponding to the detuning, and this will open a small window in the reflection gap allowing transmission. Therefore the intermediate band and the dispersion associated with it for small detuning between ω_X and ω_B give an opportunity to use the

BSQW structures as a slow-light medium. There are currently schemes proposed for stopping, storing, and releasing light pulses using BSQW structures [46,47]. In addition, BSQW structures can be fabricated from technologically important semiconductor materials [48] allowing for potentially compact devices which are integrable with current optoelectronic systems.

6.3 Challenges in growth of BSQW

With current MBE technology, growing high-quality, regular MQWs is common. However, fabrication of BSQWs is much more difficult. There are several difficulties associated with the growth of the BSQW structures which are unique to this type of fabrication. Discussed here are some of the challenges we faced during the growth of 210 quantum well GaAs/InGaAs BSQW structures [48]. The first difficulty is the sensitivity of BSQW structures to detuning between the Bragg frequency ω_B and the material resonance frequency ω_X [48]. Even an error as small as two monolayers (one lattice constant) per period, or 0.5% of one period of the RPBG is enough to distort the linear response (e.g. photonic band) of the structure considerably. Fig. 6.3 shows simulations of the RPBG for varying N, all two monolayers short per period of the Bragg spacing condition.

As was mentioned, the precision of the growth (exactness of a particular layer thickness which needs to be repeated) is less than one monolayer. However, growing the desired thickness is more challenging and the estimated percentage error of accuracy is several times greater (2-3%). In other words, a certain layer thickness can be repeated over within better than single monolayer certainty but that thickness can be a few percent different than what was initially intended. There are various reasons for these types of

errors including growth rate deviations over time, and difference in the width of a particular layer because of strain.

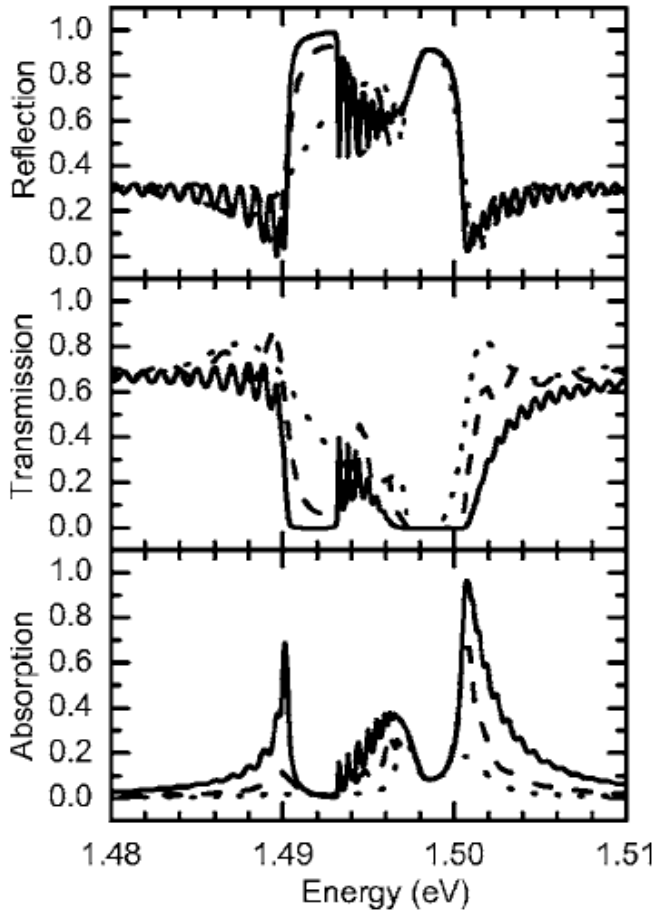

Figure 6.3 Simulated linear response of a Bragg-spaced quantum well structure [48] with each period two monolayers short of the Bragg condition for N=100 (dot), 300 (dash), 1000 (solid). The small deviation from Bragg spacing leads to opening of the intermediate band.

Another difficulty in fabricating a BSQW is the time required for growth. To realize a BSQW, hundreds of quantum wells are required with relatively thick, half-wavelength barriers. With the common growth rate of 0.5 monolayers per second, the

growth of a structure with 210 quantum wells (as in Ref.48) would take 2 days. Even small drifts over time in the growth rate of the materials can cause significant thickness differences among the individual quantum wells.

Even though the fabrication of these structures is difficult, they have some linear and non-linear properties which make BSQW structures unique. For instance, there are some theoretical studies proposing slowing and trapping light in BSQW type structures [46,47,96]. Also, they can serve as model systems for periodic resonant structures, which can be realized from other materials/geometries, such as periodic ring resonators [94,98]. To date, the BSQW is the only actual experimental realization.

6.4 Tunability of BSQW structures

As is mentioned in last section, even though MBE growth has great precision, it is lacking in the requisite accuracy for realizing BSQW structures. A simple solution for this problem is to introduce some tunability to the structure. One possible way to tune $\Delta\omega=\omega_B-\omega_x$ of the BSQW structure is with temperature. The exciton energies of the MQWs, which are the building blocks of the BSQW structures, depend on temperature since the fundamental band gap energies will change with temperature. These changes happen due to the electron-phonon interactions [99,100]. Tuning the quantum well resonance by changing temperature might increase the number of phonons in the structure. The increase in creation of phonons is not desirable especially for high speed applications, because this leads to increased collisional dephasing, increased incoherent carrier creation, and increased material recovery time.

Another technique which can be used to introduce tunability into BSQWs is to grow a wedged structure by varying the amount of material deposited across the surface

of the structure so that Bragg periodicity $\omega_B \approx \omega_X$ can be aimed to meet in the middle of the substrate instead of the entire surface. Any discrepancy between desired and actual growth rate will not compromise the entire sample. Instead, the Bragg periodicity condition will be achieved at some point on the sample.

To maintain uniform thickness of each individual layer, substrates are generally rotated since the material flux is not constant all over the substrate surface. By not rotating the substrate, the barrier and quantum well width will change across of the sample surface. By considering Ga cell's position with respect to substrate position, it is possible to get a gradient in sample thickness as large as 10% in a certain direction, since a big percentage of wells and all of the barriers are made out of GaAs [48].

The well and barrier thicknesses of the BSQW structures are related to the exciton ω_X and Bragg resonances ω_B of the material respectively. Even though well and barrier thicknesses are both subject to the same magnitude of deviations in thickness, Bragg resonance is more sensitive to changes in the thickness than exciton resonance, $\omega_X . \omega_B$ depends inversely on the barrier width whereas ω_X is determined in first order by the 3d bandgap energy which does not change with thickness and, then, in second order by the confinement energy which depends on quantum well thickness. This sensitivity difference enables us to use the wedge as an instrument of tunability.

6.5 Long growth times

The time required for the BSQW growth is another serious problem. In order to observe the interesting linear and non-linear properties of BSQW, a structure with hundreds of quantum wells is required. With the common growth rate of 0.5 monolayer

per second, the growth of a structure with 210 quantum well (as in Ref.48) would take 2 days. Even small drifts over time in the growth rate of the materials can cause significant barrier thickness differences among the individual quantum wells.

The simplest solution is to increase growth rate to reduce the growth time required for the BSQW structure. By increasing the effusion cell temperature, the sublimation or vaporization of materials can be increased. The growth rate can be controlled by changing the cell temperature. However, increasing growth rate indefinitely will decrease the growth quality. A growth time of 48 hours of 210 quantum wells can be decreased to nearly 24 hours by doubling the typical growth rate to one monolayer per second [48].

On the other hand, 24 hours is still a very long time for MBE growth, and the small drifts in growth rate could cause serious deviations from Bragg periodicity as seen in Fig. 6.3. Therefore, any drift needs to be detected, and then corrected by recalibrating growth rate. Reflection high energy electron diffraction (RHEED) measurements are used to detect actual growth rate during the growth process. This measurement is done by reflecting a high energy electron beam off the surface of the structure during growth. A series of diffraction spots are imaged onto a 2-dimensional CCD camera or a phosphorescent screen. The brilliance of these spots is at the maximum value when the beam is refracted from a complete monolayer, and the brilliance is at a minimum when the monolayer is exactly half completed. By measuring the change of the brilliance of a spot during several monolayer growths, the growth frequency can easily be determined. If the actual growth rate during the growth is different than the desired rate, it can be can be adjusted by changing the effusion cell temperature.

6.6 BSQW growth results

To optimize the growth of large-period Bragg-spaced periodic quantum wells, we chose to begin with a quantum well number N=210, large enough to produce a resonant photonic band gap but not too large to complete the growth in a reasonable time. Four N=210 Bragg-spaced quantum well structures were grown. These are the longest BSQW structures grown to date, with epilayer thicknesses exceeding 23 μm.

In our initial attempts to grow N=210 Bragg-spaced quantum well structures, we calibrated material growth rates before growth using RHEED and did not attempt to correct them during growth. The initial structure, IA1436, was grown at a rate as slow as 0.349 ml/ s and took over 65 hours to grow. Comparison of the simulated reflection from the target structure (see, e.g., Fig. 6.2, right) and the measured reflection from the experimental structure, displayed in Fig. 6.4, shows good agreement. The linear spectra show the clear formation of a resonant photonic band gap without substantial coupling to the intermediate band. The main departure from the target structure is apparent in a slight drop in reflection on the low energy edge of the resonant photonic band gap and corresponding slight increase in transmission.

The initial attempt to repeat the growth of IA1436 was made with a faster growth rate of 0.88 ml/ s, so the growth took over 26 h to grow. The result, IA1498, is shown in the measured linear spectra of Fig. 6.5. Compared to IA1436 in Fig. 6.4, there is a strong collapse of the resonant photonic band gap corresponding to a drift in growth rate of about 5%, as determined by a comparison of RHEED oscillations before and after the growth. The drift in growth rate was thus a substantial factor.

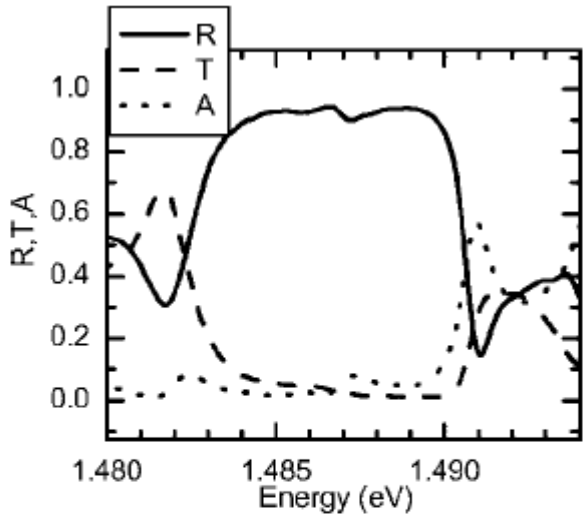

Figure 6.4 Low temperature (10 K) measured reflection (solid), transmission (dashed), and absorption (dot) A=1−R−T of Bragg-spaced quantum well structure IA1436. Growth rate was not monitored or corrected.

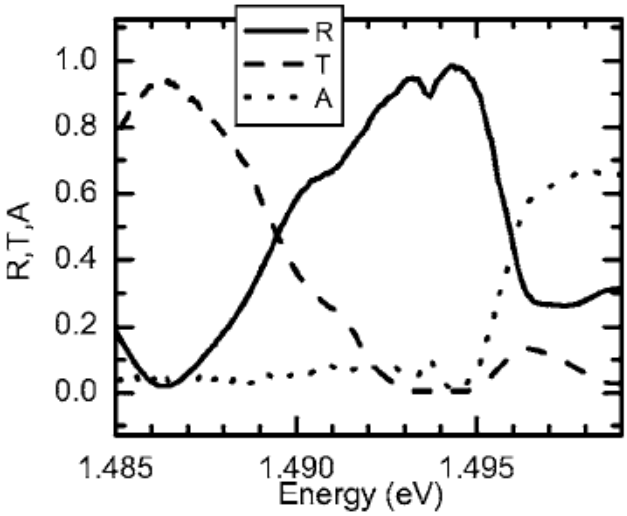

Figure 6.5 Low temperature (10 K) measured reflection (solid), transmission (dashed), and absorption (dot) A=1−R−T of Bragg-spaced quantum well structure IA1498. Growth rate was not monitored or corrected. Drift in growth rate led to collapse of the resonant photonic band gap.

To repeatably grow Bragg quantum well structures with N=210 quantum wells or much longer, growth rate drift should be kept to less than 1% throughout the entire growth. If the growth rate is checked, growth rates can be corrected during the growth of a structure by simply altering the cell temperature. Because drifts in growth rate are primarily due to Ga, which has a growth rate 20–50 times faster than In, we focused mainly on correcting the Ga growth rate.

A pause of about 20 s in the middle of the growth of the GaAs barrier in each period was introduced in the growth recipe in order to smooth the surface and allow the measurement of good RHEED oscillations during the growth of any period of the structure. By collecting RHEED oscillations for 90 s of GaAs barrier growth, we found RHEED could repeatably measure the Ga growth rate with a precision of 0.007 ml/ s or better than 1% for a growth rate of 0.88 ml/ s.

Using the above method of measuring and correcting the growth rate, the GaAs growth rate was checked and corrected if necessary every 5 h during the growth on the subsequent growth, which was otherwise an exact replica of IA1498. The result, IA1502, is shown in the linear spectra in Fig. 6.6 (a). A very square resonant photonic band gap appears in transmission spectrum and looks very close to the simulation of the ideal structure in Fig. 6.6 (b), simulated using a measured quantum well response.

The experimental structure deviates in a small way from the ideal structure. In particular, two small peaks appear in the experimental resonant photonic band gap that is not in the ideal structure. Correction of the growth rate from time to time during the growth leads to some random disorder in periodicity of about 1% of Bragg periodicity in the structure.

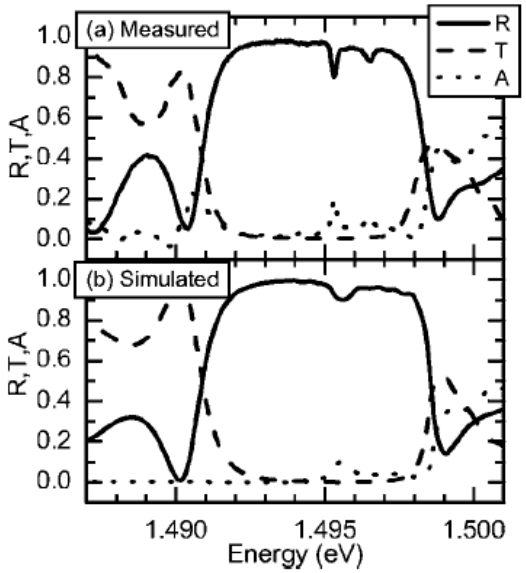

Figure 6.6 Experimental and theoretical results for: a) Low temperature (10 K) measured reflection (solid), transmission (dashed), and absorption (dot) A=1−R−T of Bragg-spaced quantum well structure IA1506. Growth rate was monitored and corrected during growth. b) Comparison to a simulation of an identical ideal (i.e., no disorder in periodicity) Bragg-spaced quantum well structure.

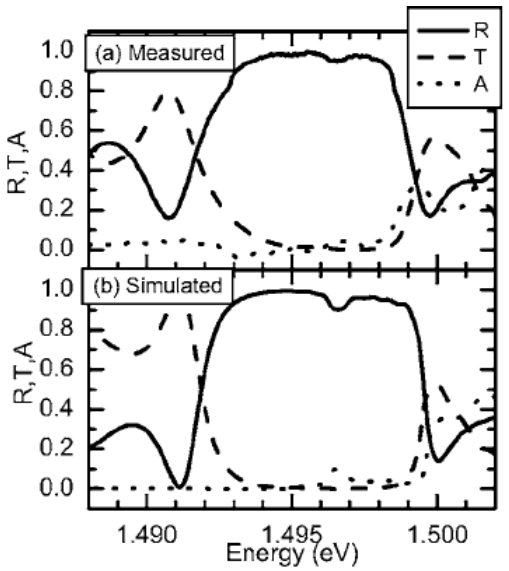

Figure 6.7 Experimental and theoretical results for: a)Low temperature (10 K) measured reflection (solid), transmission (dashed), and absorption (dot) A=1−R−T of Bragg-spaced quantum well structure IA1502, grown with a different Ga cell. Growth rate was monitored and corrected during growth. (b) Comparison to a simulation of an identical ideal (i.e., no disorder in periodicity) Bragg-spaced quantum well structure.

In a final run, we ran the recipe of IA1498 again except using a different but more stable Ga cell and still using the method of in situ correction of the GaAs growth rate. The result, IA1506, in measured linear spectra in Fig. 6.7 (a) and compared to simulated spectra of an ideal structure in Fig. 6.7 (b), shows good success in the formation of a near-ideal resonant photonic band gap. In the final structure, no extra peaks appear due to, e.g., random disorder as in IA1502. However, the resonant photonic band gap of IA1506 is not quite as square as in IA1502. The origin of this deviation may be due to up to 1% of drift in periodicity.

6.7 Slow light measurements on BSQW structures

After the growth of the InGaAs/GaAs BSQW structures, we demonstrated that BSQWs can be used to produce tunable slow light delays [97]. As discussed above, the width of the intermediate band (IB), $\Delta\omega_{IB}$, and the v_g associated with it are each proportional to the relative detuning $|\omega_B - \omega_X|$ [46,47]. Thus, the speed of light in a BSQW can be varied and controlled by shifting ω_B and/or ω_X externally following growth. Figure 6.8 (b) shows v_g as a function of photon energy for two $\Delta\omega_{IB} = -3.0$ meV (corresponding to the IB in Fig. 6.8 (a)) and −1.25 meV. The inset shows the variation of the maximum v_g versus $\Delta\omega_{IB}$. Clearly, the group velocity can be made arbitrarily small by narrowing the IB. In fact, when $\Delta\omega_{IB} = 0$, the IB is flat, $v_g = 0$, and no propagation is allowed. However, as v_g becomes smaller, the available bandwidth also shrinks so only smaller and smaller bandwidth pulses can propagate through.

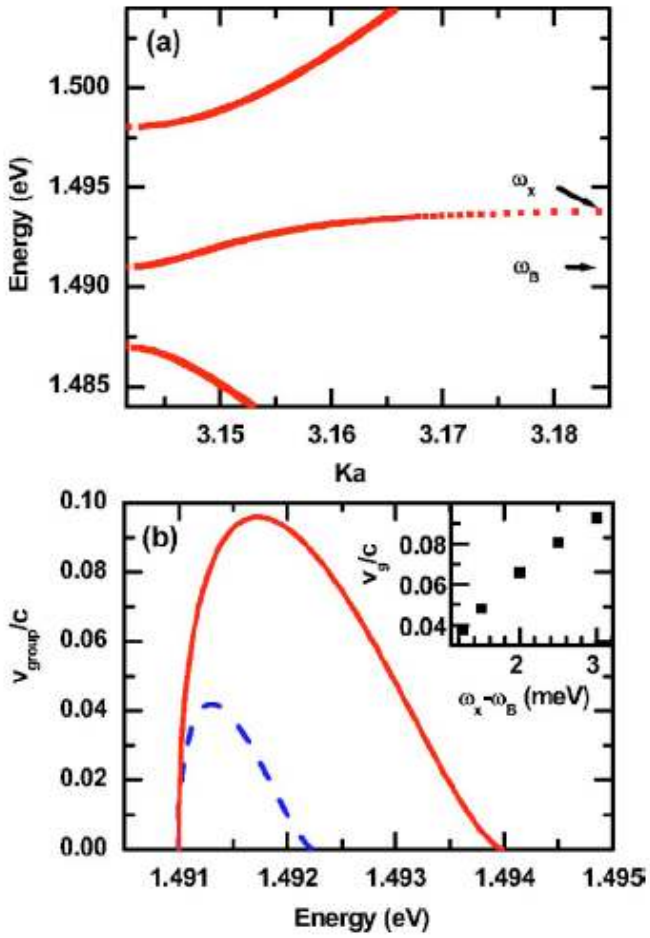

Figure 6.8 For a BSQW structure: a) Simulated band structure of a detuned ($\Delta\omega = \omega_B - \omega_X = -3.0$ meV) from Eq. 6.1. b) Simulated group velocity at two different detunings, $\Delta\omega = \omega_B - \omega_X = -3.0$ meV (red, solid) and −1.25 meV (blue, dashed). By varying the detuning $\Delta\omega$, the group velocity of the pulse is continuously tunable (inset).

Figures 6.9 a) and b) show, respectively, the simulated and measured reflection (R), transmission (T), and absorption (A=1−R−T) of the BSQW for a detuning $\Delta\omega$ = −3.3 meV. Experimentally, detuning is determined by mapping layer thicknesses, measured directly by x-ray diffraction, as a function of position on the sample surface, and confirmed with numerical simulations of the spectra. Measurements are performed with

the sample mounted in a cryostat cooled to 10 K. Good quantitative agreement can be seen in Figs. 6.9 (a) and (b) between simulation and experiment. Deviations can be explained by the disorder in the quantum well periodicity.

Both experiment Fig. 6.9 (a) and simulation Fig. 6.9 (b) show an ~8-meV-wide high-reflection on stop band associated with the forbidden photonic band gap. The IB is visible in the middle of the stop band and has a bandwidth approximately equal to the detuning $\Delta\omega = -3.3$ meV. However, the reflection (transmission) decrease (increase) is small, and oscillations in the reflection appear within the IB. These non-ideal features are caused by the large effective index of refraction associated with the BSQW [46]. Fresnel reflections at the front surface associated with this large index cause poor coupling efficiency of the light into the IB rather than a well-defined allowed transmission window. In addition, Fresnel reflections at the air/BSQW and BSQW/substrate interfaces lead to Fabry-Pérot fringing and account for the reflectivity oscillations seen within the IB.

The group velocity and group velocity dispersion of pulses propagating through the BSQW shown in Fig. 6.9 (a) are investigated by measuring the delay and broadening of a weak (88 nJ/cm^2) 3.5 ps transmitted pulse. The incident pulses are obtained by attenuating and using a pulse shaper to spectrally narrow (to 0.67 meV) pulses from a mode-locked Ti:sapphire laser. The time delay and width of each transmitted pulse are measured by cross correlating the transmitted pulse with an 80 fs reference pulse using second harmonic generation in a beta barium borate crystal. The relative delay and broadening of each transmitted pulse are shown in Fig. 6.9 (c). Near the low energy edge of the IB, time delays dramatically and continuously increase to ~0.4 bit (1 bit=3.5 ps),

corresponding to $v_g \sim 0.067c$, with little pulse broadening and ~10% transmission. In this regime, the pulse delay can be continuously tuned either by tuning the wavelength of the incident pulse or actively changing the width of the IB by external tuning of the exciton resonance (e.g., AC or DC Stark effect). As the pulse is tuned to the upper energy edge of the IB, the group velocity is further reduced; the transmission goes to zero, and the pulse broadening sharply increases. A maximum of 0.7 bit delay, corresponding to a group velocity ~0.038*c*, is observed in the region near the upper edge of the IB, but the pulse is broadened by ~0.5 bit.

6.8 Slow light measurements on antireflection coated BSQW structures

The less than ideal performance of the BSQW used for the measurements shown in Fig. 6.9 can be attributed to the Fresnel reflections and Fabry-Pérot fringing [46]. In an attempt to reduce these adverse effects, we grew an identical sample to the BSQWs, except that an antireflection (AR) coating was grown on both incident and exit sides. On the incident side (air/BSQW interface), the AR coating consists of 7.5 periods of quarter wave layers ($\lambda_{Design}/4n_b$ thick) of GaAs/$Al_{0.33}Ga_{0.67}As$, two available (but non-optimal) materials, designed according to Ref. 98. On the exit side (BSQW/substrate interface), an identical AR coating was used (but was nonoptimal due to GaAs rather than air as the exit medium). The design wavelength (λ_{Design}) was chosen to be close to λ_B ($=2\pi n_b c/\omega_B$) ,where the group velocity (and group index) is fairly flat (e.g., see Fig. 6.8). Figure 6.10 (a) shows simulations of *R*, *T*, and *A* of the target BSQW detuned to $\Delta\omega = \omega_B - \omega_X = -3.3$ meV.

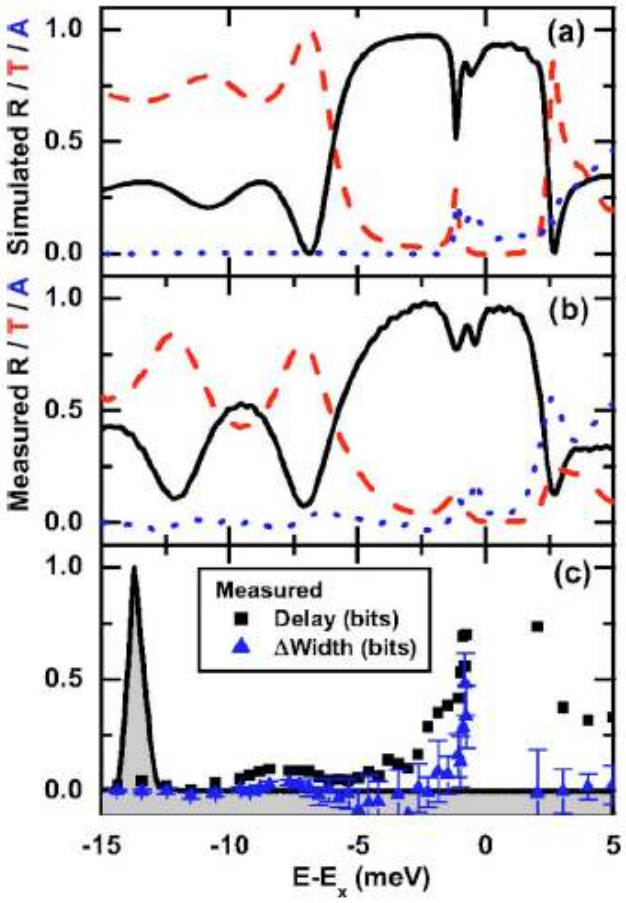

Figure 6.9 Experimental and theoretical results for the BSQW structure. a) Simulated reflection (black, solid), transmission (red, dashed), and absorption (blue, dotted). b) Low temperature measurements (10 K) on the corresponding experimental structure. c) Measured relative delay (black, square) and pulse broadening (blue, triangle) of a 0.67 meV (3.5 ps) pulse, shown for reference in black/gray fill.

The simulation shows reduced Fabry-Pérot fringing and improved coupling to the IB, i.e., less reflection across the IB. Figure 6.10 (c) shows measurements of *R*, *T*, and *A* of the corresponding AR coated BSQW structure performed at low temperature (10 K). The coupling of light clearly is improved in the AR coated BSQW compared to the non-AR coated structure (Fig. 6.9), with minimum reflection close to zero; however, Fabry-Pérot fringing is more pronounced than in the simulated target structure in Fig. 6.10 (a).

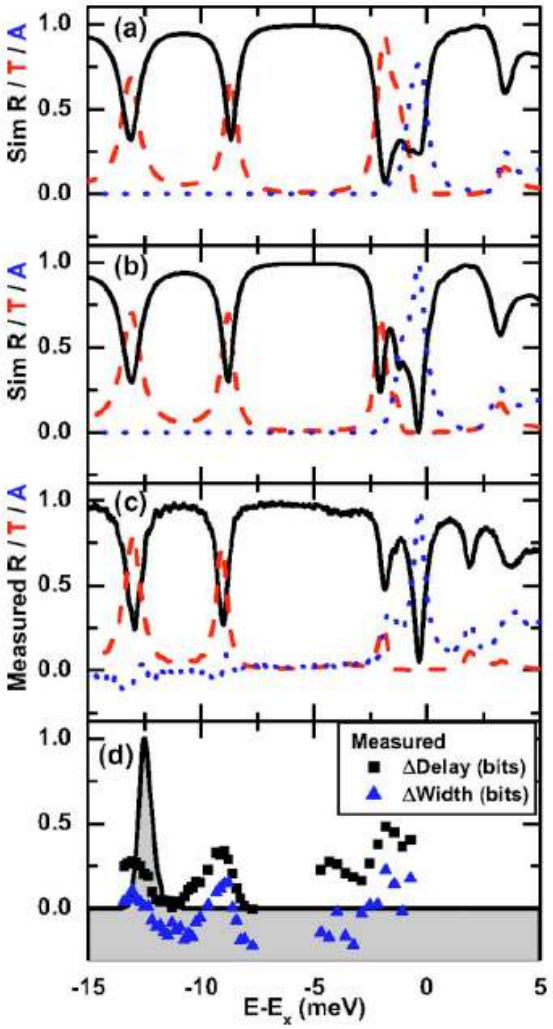

Figure 6.10 Simulation of a BSQW identical to Fig. 6.9 except with AR coatings on the front and exit interfaces designed for a) $\Delta\omega = -3.3$ meV and b) $\Delta\omega = 22$ meV, including reflection (black, solid), transmission (red, dashed), and absorption (blue, dotted). c) Measurement of an experimental sample with target structure of (a), but actual structure closer to (b). The percentage error in AR coating layer thicknesses equals 1.5%. d) Measured relative delay (black, square) and pulse broadening (blue, triangle) of a 0.67 meV (3.5 ps) pulse, shown for reference in black/gray fill.

We speculate that the difference between the simulated and grown AR coated BSQWs may be due to small errors in the thicknesses of the layers in the AR coating. This sensitivity to errors in the layer thickness is illustrated by the simulation shown in

Fig. 6.10 (b) where an error in the layer thicknesses of 1.5% has been assumed and which produces significantly better agreement with the experimental result. Improved designs that are less sensitive to small errors in the layer thicknesses can be constructed from materials with more optimal indices of refraction.

The delay and broadening of a 3.5 ps pulse transmitted through the AR coated BSQW using the same procedure as that used to obtain Fig. 6.9 (c) are shown in Fig. 6.10 (d). The AR coating improved the coupling and reduced the fringing of the BSQW. Near the lower edge of the IB, there is a spectral region where the delay is significant (~0.25 bit) and broadening is negligible. Closer to the excitonic resonance, a maximum bit delay of 0.5 is observed, but at the expense of increased broadening of the pulse width (~0.2 bit) and reduced transmission (~1%).

Slow light features are observed in the AR coated BSQW that are not present in the uncoated sample. Below the reflectivity stop band, the AR coating acts like an ordinary Fabry-Pérot cavity, i.e., two mirrors separated by the thickness of BSQW structure. Regularly spaced modes of the cavity can be seen at the low energy side of the high reflectivity photonic stop band in Fig. 6.10 (d). As expected, the laser pulses are also slowed and broadened by the dispersion associated with the bare cavity modes.

The negative changes in pulse width shown in Fig. 6.10 (d) suggest that the pulse is temporally compressed at some photon energies (e.g., midway between cavity modes). This compression of the nearly transform-limited pulses is due to a spectral reshaping of the pulse. When positioned midway between cavity modes, the spectral tails of the pulse are enhanced, while the center of the pulse is attenuated, resulting in a pulse with a spectrally broader and temporally narrower width.

6.9 GaAs/AlGaAs regular quantum wells

We also grew the samples used in slow light measurements of Chapter 3. They have been grown as a set of five samples: N= 20, 40, 80, 120, and 160. However we have only used N=20, and 40 QWs sample. Because the high absorbance of other samples made impossible to detect the slow light signal with narrow spectrum in the vicinity of the heavy hole absorption resonance.

Fortunately, the growths of these GaAs/AlGaAs QWs were not as challenging as BSQWs. It is partly because regular GaAs/AlGaAs QW growth is well established. Also the real hardship the growth of BSQW structures comes from the length of the structure (more than 20 μm) and MBE is a weak technique for this type of structures. On the other hand the longest (160 QW is about 5 μm) of the regular GaAs/AlGaAs MQW structures is still much shorter than a BSQW structure (5 μm versus 20 μm).

6.10 Conclusions

We have presented a comprehensive study of the MBE growth of BSQW's. To begin, we considered the impact of disorder and drift in periodicity of the quantum wells on the RPBG. We found that drift in the growth rate greater than a few percent leads to collapse of the RPBG. By monitoring and correcting the growth rate during growth of the BSQW with RHEED we were able to keep drift and disorder in periodicity to less than 1%, and we succeeded in growing near-ideal N=210 BSQW structures at a fast growth rate (0.9 ml/s). These are the longest BSQW structures yet grown. We see no fundamental or even practical barriers to growing much longer structures, such as N=1000 periods or longer.

We have measured slowing and broadening by group velocity dispersion of picosecond pulses propagating in the IB of the BSQW. We grew an identical sample to the BSQWs, except that an antireflection (AR) coating was grown on both incident and exit sides to reduce to the Fresnel reflections and Fabry-Pérot fringing observed during slow light measurements. Continuously tunable delays from 0 to ~0.4 bit were measured with negligible broadening for the non-AR BSQW. Unoptimized AR coatings were shown to improve the coupling of light into the structure. AR coatings fabricated from GaAs and AlGaAs were also found to be sensitive to small errors (~1.5%) in the AR coating layer thicknesses.

CHAPTER 7: FUTURE WORK

7.1 All-optically controlled slow light

As mentioned in Chapter 1, an optical buffer can help to increase the performance of an optoelectronic system. As can be deduced from the results of slow light experiments in Chapter 3, in a GaAs/AlGaAs MQW sample it is impossible to accomplish more than 1 bit delay without significant absorption of the light. Also in Chapter 5, the AC Stark effect was employed in our all-optical switch. By combining these two kinds of experiments we can control the fractional delay of a pulse all-optically by introducing a control pulse spectrally centered below the resonance. Instead of tuning the signal pulse with respect to the absorption peak of GaAs/AlGaAs MQWs, the absorption profile can be moved as the signal pulse is kept fixed spectrally. In other words, we will control the delay of a signal pulse actively rather than shifting the signal to control the delay. Since the AC Stark effect will be employed for controlling the delay, the material response and recovery will be only limited by the duration of the control pulse.

Therefore, I propose an investigation of an all-optically controlled optical buffer. The polarizers are removed from the switching setup as seen in Figure 7.1a. In the absence of the circularly-polarized control pulse, both co-linear signal pulses are not delayed when they are transmitted through the sample, since both are spectrally tuned slightly away from the absorption resonance. The slow pulse is Signal 1 and it has opposite circular polarization as the control pulse. Signal 2 is the fast pulse so that it needs to be delayed and it has the same circular polarization as the control pulse.

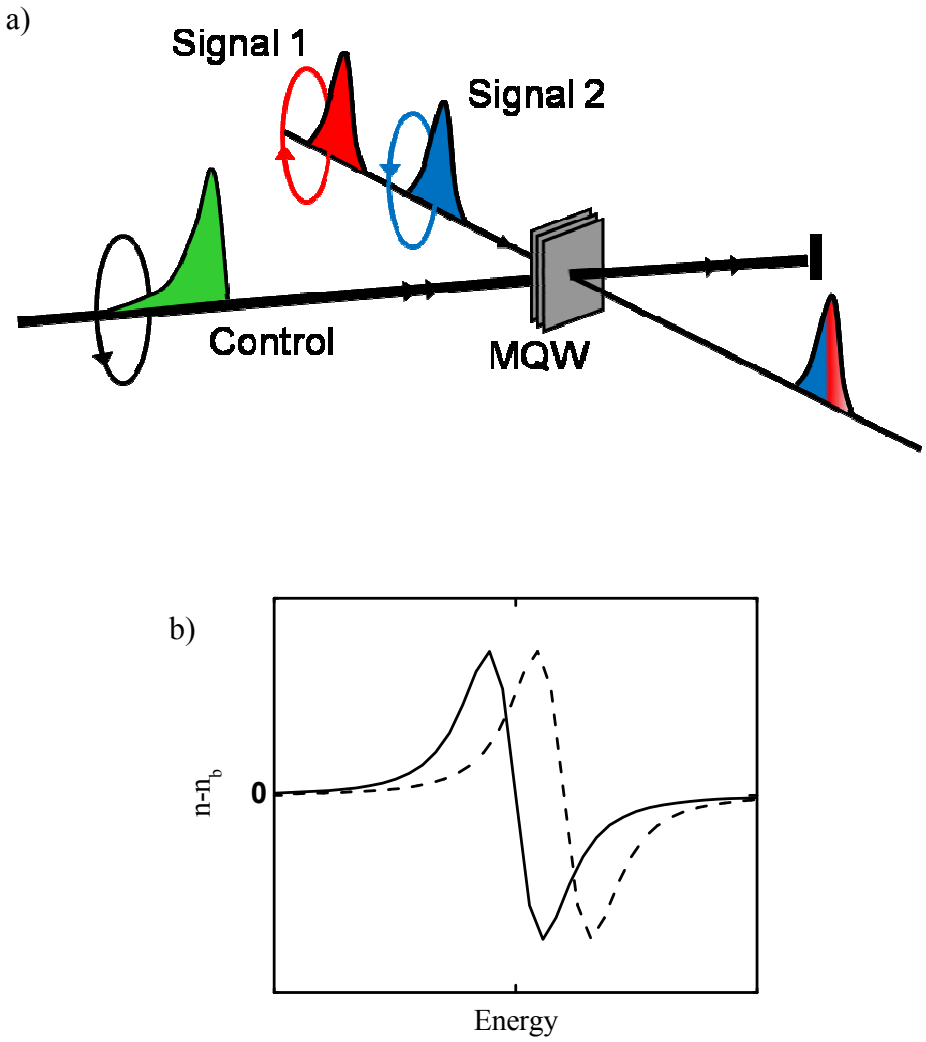

Figure 7.1 For all-optically controlled slow light measurements. a) Experimental configuration of setup. b) The blue shift of the index of refraction induced by the AC Stark effect. The background index of refraction is subtracted for convenience.

When the control pulse is present, it interacts with only one spin type but not with the other as was discussed in Chapter 4 and 5. Signal 2 also interacts with this same spin kind. Since the control pulse is spectrally detuned below-resonance, it will induce a blue shift and bleaching for this type of spinas can be seen in Fig. 7.1b. The spectral position of the Signal 2 pulse will change with respect to the peak of the absorption resonance and

it will experience absorption and delay. The amount of delay and absorption induced can be controlled by the detuning and the irradiance of the control pulse. On the other hand, the Signal 1 which has opposite circular polarization compared to the control pulse will not be affected by these induced changes. Therefore two oppositely circular signal pulses can be shifted continuously relative to each other in time by choosing the polarization, detuning, and the irradiance of the control pulse. Also there will be no material recovery time for the slow light medium, since no real carriers are created by employing the AC Stark effect. In addition there will be no need for any mechanical or moving parts. An effect such as this can be useful, for instance, where two pulses need to be synchronized after one of them delayed for a long time in a passive delay line that the delay amount is discrete.

7.2 Slow light measurements for spatially dispersive media

As we explained the differences in slow light experiments in resonant media in the literature, one of the points made is that spatial dispersion makes a large difference in the wave propagation in absorptive media. Observing the peculiarities that occur with spatial dispersion is difficult. As mentioned Chapter 2, when Gu et. al. [55] discussed the results of Ulbrich et. al. [38], Gu concludes that Ulbrich could not see these spatial dispersion features because Ulbrich did not have the spectral resolution. Gu estimated that 0.1 A^0 resolution and 100 ps pulses should have enough spectral resolution to see the difference spatial dispersion makes in high quality samples. So far, there is no experiment reported in the literature that has been conducted with this pulse width in a spatially dispersive medium such as bulk GaAs. In addition, results of an experiment with this

spectral resolution will be very important in demonstrating the role of spatial dispersion in the propagation of light in resonant media. At the same time, this experiment might be a corner stone in literature to compare, contrast and catalog previous results, some of which were discussed in Chapter 2. Therefore repeating the Ulbrich experiments, which are very similar to our slow light measurements with a new sample type and temperature, is another avenue which can be explored if we can obtain enough spectral resolution.

APPENDIX

A.1 Dispersion relation in bulk semiconductors

In single atoms, only certain orbits and discrete energies are allowed for electrons. However when a large number of atoms come together to form a crystal, these discrete energy levels become coupled and blended to form continuous energy bands in which the electrons are allowed and band gaps in which electrons are forbidden. A simplified band structure of a direct-gap zincblende semiconductor such as GaAs is illustrated in Fig. A.1. Conduction and valence bands are shown on the left hand side of the Fig. A.1, as the energy $\vec{E}$ verses real space position $\vec{z}$ graph.

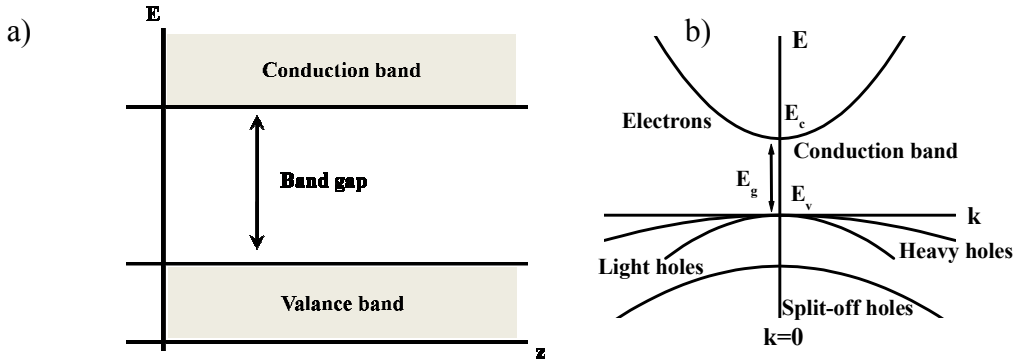

Figure A.1 The simplified band structure diagrams for a bulk direct-gap zinc-blende type semiconductor. a) The energies of conduction and valence band as a function of direction *z*. b) The conduction band and the heavy holes, light holes, and split-off holes sub-bands are represented as a function of crystal wave-vector $\vec{k}$ near $\vec{k} = 0$.

The *valence band* is the highest energy band filled with electrons at 0 K, and the highest energy point in this band called as the *valence band edge,* E_v. *The conduction band* is the lowest empty band at the same temperature and the lowest energy point in this

band referred as the *conduction band edge,* E_c. As shown on the right hand side of the Fig A.1, if the valence band edge and conduction band edge occur at same wave number, k, then the semiconductor is referred to as a *direct bandgap semiconductor*. The energy difference between the lowest energy point of the conduction band and the highest energy point of the valence band is called the *bandgap energy*, $E_g = E_c - E_v$.

When an electron is excited into the conduction band, it leaves behind an empty state in the valence band. This state can be viewed as an electron leaving the valence band or a positive charged particle called a *hole* moving into the valence band. The electron in the conduction band and the hole in valence band will have some of the excess of the excitation energy as kinetic energy. The electron in the conduction band and the hole in the valence band will move with this kinetic energy. Recall that the energy of a free electron is,

$$E = \frac{\hbar^2 k^2}{2m} \tag{A.1}$$

where $\hbar$ is the Planck's constant divide by 2π, $\vec{k}$ is the wave vector, and m is the mass of an electron. The excited electron is not totally free in a crystal however; in the dispersion relation curves in Fig. A.1 energy changes quadratically with $\vec{k}$ (at least close to $\vec{k} = 0$) as in the free electron form but with different curvatures. Hence, the motion of excited electrons and holes can be described as particles in free space with different effective masses, m^*. The effective mass is given by Ref. 101,

$$m^* = \frac{\hbar^2}{d^2 E / dk^2}\,. \tag{A.2}$$

The *effective mass* takes all the forces exerted on the electrons or the holes by the crystal into account, and allows us to use the standard equation of motions for them by replacing *m* with *m**.

As mentioned above, the valence and conduction bands can be approximated as a parabola centered on zero in $\vec{k}$ (crystal momentum) space for direct-gap bulk semiconductor. As shown in Fig A.1b, the valence band consists of three sub-bands called heavy hole (hh), light hole (lh), and split-off bands. The heavy and light hole bands are degenerate, and they cross the $k = 0$ line together at the same point, but can be differentiated by their curvature, which reflects their effective masses. The split-off band is depressed by spin-orbit coupling [102]. Each of these three bands and the conduction band consist of two sub-bands of opposite spin.

A.2 Dispersion relation in MQW structures

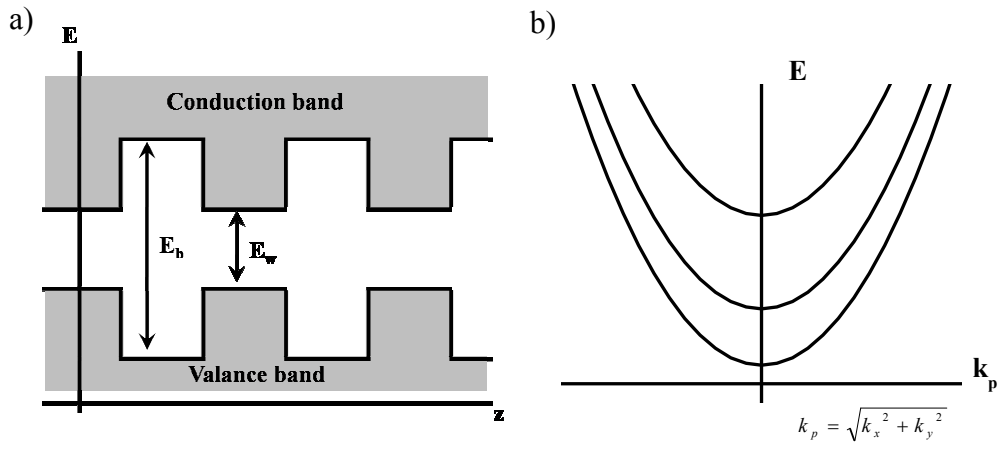

Figure A.2 The simplified band structure diagrams for a MQW structure. a) The energies of conduction and valence band as a function of direction *z* for wells and barriers. b)The energy versus wave vector graph for the electrons in the perpendicular to the growth direction.

A very well-known semiconductor material is the MQW structure. It consists of alternating semiconductor layers of different bandgap energies. The layers with smaller bandgap energy (E_w) are referred to as wells, as ones with greater bandgap energy (E_b) form barriers as seen on the left hand side of the Fig A.2.

The electrons in the conduction band and the holes in the valence band are confined in the z -direction (growth direction) due to the periodic potential formed by alternating layers. This confinement will change the allowed energy levels for both electrons and holes. The analytic solutions for dispersion relations of the quantum wells can be found in different sources [60,103]. For the sake of simplicity, we will assume an idealized case where all the bands of the well material are isotropic, and parabolic with respect to $\vec{k}$ as in Fig. A.2. Also, we assume the barriers are impenetrable, $E_b = \infty$ which is the very well-known quantum mechanics' problem: Particle in a box. Electrons and holes are still free to move in the plane of the well (x , and y -direction), but they will be confined in the growth direction (z direction). For infinitely high barriers, the energy levels of the electrons can be found to be

$$E_e^{n_z} = \frac{\hbar^2 \pi^2 n_z^2}{2 m_e^* l_w^2} \tag{A.3}$$

where $n_z = 1,2,3,...$ and l_w is the well width. In Fig. A.2a, the energy versus wave vector graph is plotted for the electrons in the perpendicular to the growth direction. The energy levels for the are shown for small k_x and k_y ($k_{x(y)}$) is the crystal wavevector in x(y) direction), the energy of electrons will be

$$E_{x(y)} = \frac{\hbar^2 k_{x(y)}^2}{2m_e^*}. \tag{A.4}$$

If we assume the valence band edge of the well material is zero energy, then the total energy of an electron in conduction band will be

$$E_{CB} = E_w + \frac{\hbar^2 (k_x^2 + k_y^2)}{2m_e^*} + \frac{\hbar^2 \pi^2 n_z^2}{2m_e^* l_w^2}. \tag{A.5}$$

Hence, the conduction band consists of an infinite number of sub-bands, and the bottom of the conduction band is moved to higher energies by the amount $E_e^{n_z}$. A similar split and shift can be shown for the valence band of a multiple quantum well structure; however it becomes more complicated for the valence band than the conduction band. The heavy and light holes in MQW are strongly coupled and have complicated dispersion relations. Under similar assumptions we made for the conduction band electrons, we can write the energy shift for heavy and light holes:

$$E_{hh}^{n_z} = \frac{-\hbar^2 \pi^2 n_z^2}{2m_{hh}^* l_w^2} \tag{A.6}$$

$$E_{lh}^{n_z} = \frac{-\hbar^2 \pi^2 n_z^2}{2m_{lh}^* l_w^2} \tag{A.7}$$

where n_z and the zero energy defined same way. Note that the effective masses of heavy hole and light hole are different. Therefore, the energy shift for each of them will be different and it will destroy the degeneracy of the energy levels of heavy hole and light hole. Even though an infinite number of sub-bands exists in both conduction and valence band, we will only be interested with the ones where $n_z = 1$. Note that the energy bands will be different for finite barrier energies. However, this difference will be small and it

will not affect the described qualitative behavior of the MQW. In Fig A.2b, the conduction and valence energy bands are illustrated as a function of k_x and k_y for $n_z = 1$. The valence bands are non-parabolic and distorted. In addition, the degeneracy in the valence band has lifted at $k_x = k_y = 0$ because of the different effective masses of light holes and heavy holes as mentioned above.

A.3 Excitons in bulk semiconductors

For bulk semiconductors, the absorption profile is modified significantly because of the formation of bound electron-hole pairs called excitons, when the semiconductor is excited by light near to the $n_z = 1$ the resonance. The Coulomb force between electron and hole holds them together to form a hydrogen-like atomic structure. Excitons have well-defined discrete energy levels as a hydrogen atom would have, described by principal quantum numbers and angular momentum quantum numbers. For the exciton states of n_{ex} = 1, 2, 3, (or s, p, d) etc. the binding energies of these excitons are given by

$$E_{nex} = \frac{E_R}{n_{ex}^2} \tag{A.8}$$

for bulk semiconductors where Rydberg energy, $E_R = \frac{\hbar^2}{2\mu a_0^2} = \frac{e^2}{(4\pi\varepsilon)a_0}$, the reduced effective mass μ is given by the equation $\frac{1}{\mu} = \frac{1}{m_e^*} + \frac{1}{m_h^*}$, a_0 the exciton Bohr radius, and ε the permittivity of the semiconductor in the static limit. These energy levels modify the absorption profile by producing multiple resonances just below the continuum band edge of a direct-gap semiconductor material as you can see in Fig. A.3. Here, the exciton states of $n_{ex} = 1$, 2 , and 3 levels are shown for near k = 0 in the simplified band

structure diagram to provide some insight into how they alter the absorption profile near the band edge.

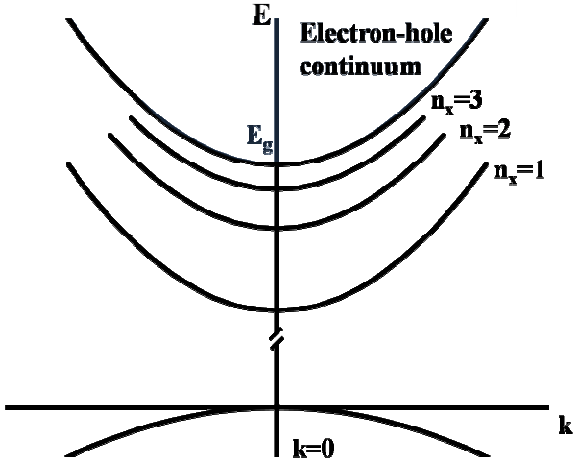

Figure A.3 The formation of excitonic bands are shown near the 1s resonance for a bulk direct-gap zincblende type semiconductor as a function of crystal wave-vector $\vec{k}$ near $\vec{k} = 0$. Exciton resonances are nearly at the same spectral positions for the heavy holes, and light holes.

Even though only one valence band is shown in Fig. A.3, excitons are produced for both heavy and light hole bands, but because of the degeneracy of those bands about $\vec{k} = 0$, exciton resonances are nearly at the same spectral points. Therefore, only one exciton peak (associated with the strongest 1s level) can be observed in the absorption spectrum. The binding energy is small (4.2 meV for GaAs) and they are easily broken apart due to collision with phonons as the temperature approaches room temperature. At room temperature, the exciton resonance broadens so much that it becomes impossible to distinguish the exciton resonance from the absorption continuum.

A.4 Polaritons and spatial dispersion

When light travels in a vacuum, it is a transverse electromagnetic wave, the quanta of which are known as photons. When light interacts with matter there are two limits which can describe the interaction between them. The first is the weak coupling between light and matter; electromagnetic fields of light and excitations of matter are treated as independent quantities as seen in Fig. 2.2a of section 2.1.2 of Chapter 2. However, in the case of the strong coupling, the light propagates in matter as a mixture of electromagnetic and polarization waves which come from the excited state of matter. This mixed wave can be quantized, and the energy quanta are known as polaritons. They are the quasiparticles of "light" in matter [104]. The most discussed types of polaritons are phonon-polaritons, resulting from coupling of an optical phonon with a photon; and exciton-polaritons, resulting from coupling of light with an electron- hole pair (e.g. exciton).

The Lorentz model of completely uncoupled oscillators described in section 2.1.2 (in which case the oscillators are only coupled indirectly through their interaction with the same light field) neglects any direct electronic coupling between the dipole oscillators. The light-induced polarization wave can't move through the system without direct electronic coupling. Therefore, a set of individual oscillators is connected together with a spring as shown schematically in Fig. A.5. For very long wavelengths of light, the adjacent oscillators are in phase, and the coupling springs will not be elongated or shortened. Therefore those oscillators will have the same frequency. As the wavelength becomes comparable to the spacing between two oscillators, some of the coupling springs will be elongated while some of them will be shortened. This will cause a change in the

"effective" spring constant. As a consequence, ω_0, the characteristic frequency of the individual oscillator (or the collective modes of the coupled oscillators system) will depend on wave vector k. The fact that the resonant (or eigen) frequency of some excitations of a solid depends on k is often called "*spatial dispersion*". Even though we describe polaritons and spatial dispersion together in the same context because of the pedagogical reasons, they are two different and independent concepts.

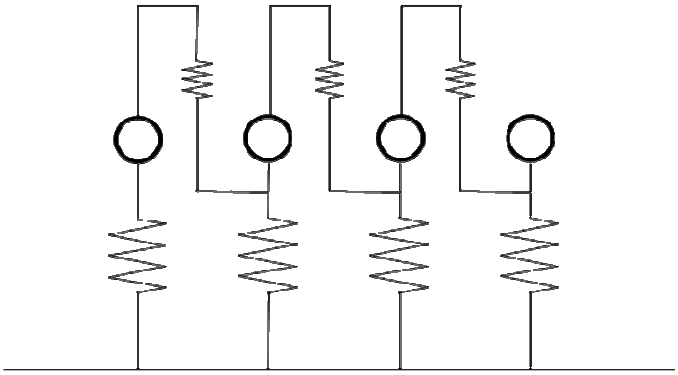

Figure A.4 Ensemble of coupled oscillators.

REFERENCES

1. G. P. Agrawal, “Fiber-Optic Communication Systems,” Wiley-Interscience (2002).

2. J. C. Palais, “Fiber Optic Communications,” Prentice-Hall (2005).

3. R.M. Camacho, M.V. Pack, and J.C. Howell, “Low distortion slow light using two absorption resonances,” Phys. Rev. A 73, 063812 (2006).

4. R. W. Boyd, D. J. Gauthier, A. L. Gaeta, and A. E. Willner, “Maximum time delay achievable on propagation through a slow-light medium,” Phys. Rev. A 71, 023801 (2005).

5. C. J. Chang-Hasnain, P. C. Ku, J. Kim, and S. L. Chuang, “Variable optical buffer using slow light in semiconductor nanostructures,” Proc. of IEEE 91, 1884 (2003).

6. R. S. Tucker, P. C. Ku, and C J. Chang-Hasnain, “Delay –bandwidth product and storage density in slowlight optical buffers,” Electron. Lett. 41, 208 (2005)

7. G. Lenz, B.J. Eggleton, C.K. Madsen, and R.E. Slusher, “Optical delay lines based on optical filters,” IEEE J. Quantum. Elect. 37, 525 (2001).

8. J.B. Khurgin, “Optical buffers based on slow light in electromagnetically induced transparent media and coupled resonator structures: comparitive analysis,” J. Opt. Soc. Am. B 22, 1062 (2005).

9. L. V. Hau, S. E. Harris, Zachary Dutton and Cyrus H. Behroozi “Light speed reduction to 17 metres per second in an ultracold atomic gas,” Nature 397, 594 (1999).

10. A. Kasapi, M. Jain, J.Y. Gin, and S.E. Harris, “Electromagnetically induced transparency: propagation dynamics,” Phys. Rev. Lett. 74, 2447 (1995).

11. C. Liu, Z. Dutton, C. H. Behroozi, and L. V. Hau, “Observation of coherent optical information storage in an atomic medium using halted light pulses,” Nature, 409, 490 (2001).

12. M. M. Kash, V. A. Sautenkov, A. S. Zibrov, L. Hollberg, G. R.Welch, M. D. Lukin, Y. Rostovtsev, E. S. Fry, and M. O.Scully, “Ultraslow Group Velocity and Enhanced Nonlinear Optical Effects in a Coherently Driven Hot Atomic Gas,” Phys. Rev. Lett. 82, 5229 (1999).

13. D. Budker, D. F. Kimball, S. M. Rochester, and V. V. Yashchuk, “Nonlinear Magneto-optics and Reduced Group Velocity of Light in Atomic Vapor with Slow Ground State Relaxation,” Phys. Rev. Lett. 83, 1767 (1999).

14. M. S. Bigelow, N. N. Lepeshkin, and R. W. Boyd, "Superluminal and Slow Light Propagation in a Room-Temperature Solid," Science 301, 200 (2003).

15. X. Zhao, P. Palinginis, B. Pesala, C. Chang-Hasnain, and P. Hemmer, "Tunable ultraslow light in vertical-cavity surface-emitting laser amplifier," Opt. Exp. 20, 7899 (2005).

16. P. Palinginis, F. Sedgwick, S. Crankshaw, M. Moewe, and C. J. Chang-Hasnain, "Room temperature slow light in a quantum-well waveguide via coherent population oscillation," Opt. Exp. 13, 9909 (2005).

17. M. S. Bigelow, N. N. Lepeshkin, and R.W. Boyd, "Observation of ultraslow light propagation in ruby crystal at room temperature," Phys Rev. Lett. 90, 113903 (2003).

18. P. C. Ku, F. Sedgwick, C. J. Chang-Hasnain, P. Palinginis, T. Li, H. Wang, S. W. Chang and S. L. Chuang, "Slow light in semiconductor quantum wells," Optics Lett. 29**,** 2291 (2004).

19. Y. Okawachi, M. S. Bigelow, J. E. Sharping, Z. Zhu, A. Schweinsberg,D. J. Gauthier, R. W. Boyd, and A. L. Gaeta, "Tunable All-Optical Delays via Brillouin Slow Light in an Optical Fiber," Phys. Rev. Lett. 94, 153902 (2005).

20. M. Gonzlez-Herrez, K.-Y. Song, and L. Thvenaz, "Optically controlled slow and fast light in optical fibers using stimulated Brillouin scattering," Appl. Phys. Lett. 87, 081113 (2005).

21. M. Gonzlez-Herrez, K.-Y. Song, and L. Thvenaz, "Arbitrary-bandwidth Brillouin slow light in optical fibers," Opt. Exp. 14, 1395 (2006).

22. D. Dahan and G. Eisenstein, "Tunable all optical delay via slow and fast light propagation in a Raman assisted fiber optical parametric amplifier: a route to all optical buffering," Opt. Exp. 13, 6234 (2005).

23. J. E. Sharping, Y. Okawachi, and A. L. Gaeta, "Wide bandwidth slow light using a Raman fiber amplifier,"Opt. Exp. 13, 6092 (2005).

24. Y. Okawachi, M. A. Foster, J. E. Sharping, and A. L. Gaeta, Q. Xu and M. Lipson, "All-optical slow light on a photonic chip," Opt. Express 14 , 2317-2322 (2006).

25. J. D. Jackson, "Classical electrodynamics" Wiley (1999).

26. A. Sommerfeld, Ann. Phys. 44, 177 (1914); L. Brillouin, Ann. Phys. 44, 203 (1914); translated and expanded in L. Brillouin, Wave propagation and group velocity Academic, New York, (1960).

27. R. Loudon, "The propagation of electromagnetic energy through and absorbing medium," J. Phys. A 3, 233 (1970).

28. C.G.B. Garrett and D.E. McCumber, "Propagation of a Gaussian light pulse through an anomolous dispersion medium," Phys. Rev. A 1, 305 (1970).

29. M. Tanaka, M. Fujiwara, and H. Ikegami, "Propagation of an absorbing wavepacket in an absorbing medium," Phys. Rev. A 34, 4851 (1986).

30. J. Peatross, S.A. Glasgow, and M. Ware, "Average energy flow of optical pulses in dispersive media," Phys. Rev. Lett. 84, 2370 (2000).

31. K. E. Oughstun and G. C. Sherman, "Electromagnetic pulse propagation in causal dielectrics" (Springer-Verlag, Berlin New York, 1994)

32. K. E. Oughstun and C. M. Balictsis, "Gaussian pulse propagation in a dispersive, absorbing dielectric," Phys. Rev. Lett., 77, 2210 (1996).

33. M.A.I. Talukder, Y. Amagishi, and M. Tomita, "Superluminal to subluminal transition in the pulse propagation in a resonantly absorbing medium," Phys. Rev. Lett. 86, 3546 (2001).

34. J.C. Garrison, M.W. Mitchell, R.Y. Chiao, E.L. Bolda, "Superluminal signals: causal loop paradoxes, revisited," Phys. Lett. A 245, 19 (1998).

35. L.J. Wang, A. Kuzmich, and A. Dogariu, "Gain assisted superluminal light propagation," Nature 411, 974 (2001).

36. A. Kuzmich, A. Dogariu, L.J. Wang, "Signal velocity, causality, and quantum noise in superluminal light pulse propagation," Phys. Rev. Lett. 86, 3925 (2001).

37. G. M. Gehring, A. Schweinsberg, C. Barsi, N. Kostinski, R.W. Boyd, "Observation of backward pulse propagation through a medium with a negative group velocity," Science 312, 895 (2006).

38. R.G. Ulbrich and G.W. Fehrenbach, "Polariton wave packet propagation in the exciton resonance of a semiconductor," Phys. Rev. Lett. 43, 963 (1979)

39. S. Chu and S. Wong, "Linear pulse propagation in an absorbing medium," Phys. Rev. Lett. 48, 738 (1982).

40. S. Sarkar, Y. Guo, H.L. Wang, "Tunable optical delay via carrier induced exciton dephasing in semiconductor quantum wells", Optics Express 14, 2845 (2006).

41. Y. Guo, S. Sarkar, and H. Wang, "Pulse Propagation near Exciton Resonance: Anomalous Transition between Slow and Fast Light," in Slow and Fast Light, OSA Technical Digest (CD) (Optical Society of America, 2007), paper STuA4.

42. E. J. Gansen, K. Jarasiunas, and A. L. Smirl, “Femtosecond all-optical polarization switching based on the virtual excitation of spin-polarized excitons in quantum wells”, Appl. Phys. Lett. 80, 971 (2002).

43. E. J. Gansen and A. L. Smirl, “Ultrafast polarization modulation induced by the "virtual excitation" of spin-polarized excitons in quantum wells: Application to all-optical switching”, J. Appl. Phys. 95, 3907 (2004).

44. W. J. Johnston, M. Yildirim, J. P. Prineas, Arthur L. Smirl, H. M. Gibbs, G. Khitrova, “All-optical spin-dependent polarization switching in Bragg-spaced quantum well structures”, Appl. Phys. Lett. 87, 101113 (2005).

45. J. P. Prineas, J. Y. Zhou, J. Kuhl, H. M. Gibbs, G. Khitrova, S. W. Koch, A. Knorr, “Ultrafast AC Stark effect switching of the active photonic band gap from Bragg-periodic semiconductor quantum wells”, Appl. Phys. Lett. 81, 4332 (2002).

46. Z. S. Yang, N. H. Kwong, R. Binder, and A. L. Smirl, “Stopping, storing, and releasing light in quantum-well Bragg structures”, J. Opt. Soc. Am. B 22, 2144 (2005).

47. Z. S. Yang, N. H. Kwong, R. Binder, and A. L. Smirl, “Distortionless light pulse delay in quantum-well Bragg structures”, Opt. Lett. 30, 2790, (2005).

48. J. P. Prineas, C. Cao, M. Yildirim, W. Johnston, and M. Reddy. “Resonant photonic band gap structures realized from molecular-beam-epitaxially grownInGaAs/GaAs Bragg-spaced quantum wells”, Journal of Applied Physics, 100, 063101, (2006).

49. W.J. Johnston, J.P. Prineas, A.L. SmirlUltrafast all-optical switching in Bragg-spaced quantum wells at 80K J. of Appl. Phys. Communications 101, 046101 (2007).

50. W.J. Johnston, J.P. Prineas, A.L. Smirl Spin-dependent ultrafast optical nonlinearities in Bragg-spaced quantum wells Submitted J. of the Optical Society of America B.

51. R.J. Elliot, “Polarons and Excitons,” edited by C. G. Kuper and G. D. Whitfield, Plenum Press (1963).

52. H. Haug, S.W. Koch “Quantum theory of the optical and electronical properties of semiconductors,” World Scientific Publishing (2004).

53 R. W. Boyd, D. J. Gauthier, “Controlling the Velocity of Light Pulses” Science 326, 1074 (2009).

54 J. B. Khurgin, R. S. Tucker, “Slow Light: Science and Applications,” CRC Press, (2008).

55. B. Gu, N. H. Kwong, R. Binder, and Arthur L. Smirl, “Slow and fast light associated with polariton interference” Phys. Rev. B 82, 035313 (2010).

56. Gregory C. DeSalvo, Wen F. Tseng, and James Comas, “Etch Rates and Selectivities of Citric Acid/Hydrogen Peroxide on GaAs, $Al_{0.3}Ga_{0.7}As$, $In_{0.2}Ga_{0.8}As$, $In_{0.53}Ga_{0.47}As$, $In_{0.52}Al_{0.48}As$, and InP,” J. Electrochem. Soc. 139, 831 (1992).

57. C. Froehly, B. Colombeau, and M. Vampouille, “Progress in Optics,” edited by E. Wolf North-Holland, Vol. 20, pp. 65–153 (1983).

58. A. M. Weiner, “Femtosecond optical pulse shaping and processing,” Prog. Quantum Electron. 19, 161 (1995).

59. Franken, P. A., Hill, A. E., Peters, C.W., and Weinreich, G., "Generation of Optical Harmonics", Phys. Rev. Lett. 7, 118 (1961).

60. P. Y. Yu, M. Cardona “Fundamentals of Semiconductors - Physics and Materials Properties,“ Springer – Verlag (2001).

61 D. A. B. Miller, D. S. Chemla, T. C. Damen, A. C. Gossard, W. Wiegmann, T. H. Wood,
and C. A. Burrus, “Band-Edge Electroabsorption in Quantum Well Structures: The Quantum-Confined Stark Effect”, Phys. Rev. Lett. 53, 2173 (1984).

62. C. Cohen-Tannoudji, J. Dupont-Roc, G. Grynberg, “Atom-Photon interactions: Basic Processes and Applications,” Interscience (1992); J. Shah, Ultrafast Spectroscopy of Semiconductors and Semiconductor Nanostructures,” Springer (1996).

63. D. S. Chemla, W. H. Knox, D. A. B. Miller, S. Schmitt-Rink, J. B. Stark, R. Zimmerman, “The excitonic optical Stark effect in semiconductor quantum wells probed with femtosecond optical pulses”, Jour. of Luminescence 44, 233 (1989).

64. N. Peyghambarian, S. W. Koch, A. Mysyrowicz, “Introduction to Semiconductor Optics (Prentice Hall Series in Solid State Physical Electronics),” Prentice Hall (1993).

65 D. Frohlich, A. Nothe, K. Reimann, “Observation of the Resonant Optical Stark Effect in a Semiconductor”, Phys. Rev. Lett. 55, 1335 (1985).

66. D. Frohlich, R. Wille, W. Schlapp, G. Weimann, “Optical quantum-confined Stark effect in GaAs quantum wells”, Phys. Rev. Lett. 59, 1748 (1987)

67 A. Mysyrowicz, D. Hulin, A. Antonetti, A. Migus, W.T. Masselink, H. Morkoc, “"Dressed Excitons" in a Multiple-Quantum-Well Structure: Evidence for an Optical Stark Effect with Femtosecond Response Time”, Phys. Rev. Lett. 56, 2748 (1986).

68. A. Von Lehmen, D.S. Chemla, J.E. Zucker, J.P. Heritage, “Optical Stark effect on excitons in GaAs quantum wells”, Opt. Lett. 11, 609 (1986).

69. W.H.Knox, D.S. Chemla, D.A.B. Miller, J.B. Stark, S. Schmitt-Rink, “Femtosecond ac Stark effect in semiconductor quantum wells: Extreme low- and high-intensity limits,” Phys. Rev. Lett. 62, 1189 (1989).

70. N. Peyghambarian, S.W. Koch, M. Linderberg, B.D. Fluegel, M.Joffre,” Dynamic Stark effect of exciton and continuum states in CdS,” Phys. Rev. Let. 62, 1185 (1989).

71. R. Zimmermann, “On the Dynamical Stark Effect of Excitons. The Low-Field Limit,” Phys. Status Solidi B 146, 545 (1988); R. Zimmermann, “Transverse Relaxation and Polarization Specifics in the Dynamical Stark Effect,” Phys. Status Solidi B 159, 317 (1990).

72. R. Zimmermann, D. Frohlich, “Optics of Semiconductor Nanostructures,” Edited by H. Henneberger, S. Schmitt-Rink, E. O. Gobel, Akademie Verlag, pp. 51-74 (1993).

73. Y. Nishikawa, A. Tackeuchi, S. Nakamura, S. Muto, and N. Yokoyama, “All-optical picosecond switching of a quantum well etalon using spin-polarization relaxation”, Appl. Phys. Lett. 66, 839 (1995).

74. Y. Nishikawa, A. Tackeuchi, M. Yamaguchi, S. Muto, and O. Wada, “Ultrafast all-optical spin polarization switch using quantum-well etalon”, IEEE J. Selected Topics Quantum Electron. 2, 661 (1996).

75. J. T. Hyland, G. T. Kennedy, A. Miller, and C. C. Button, “Spin relaxation and all optical polarization switching at 1.52 micrometres in InGaAs(P)/InGaAsP multiple quantum wells”, Semicond. Sci. Technol. 14, 215 (1999).

76. D. Marshall and A. Miller, “Carrier transport, ultrafast spin dynamics and polarisation switching in InGaAsP multiple quantum wells”, Opt. Quantum Electron. 33, 1019 (2001).

77. T. Kawazoe, T. Mishina, and Y. Masumoto, “Highly Repetitive Picosecond Polarization Switching in Type-II AlGaAs/AlAs Multiple Quantum Well Structures”, Jpn. J. Appl. Phys., Part 2 32, L1756 (1993).

78. R. Takahashi, H. Itoh, and H. Iwamura, “Ultrafast high-contrast all-optical switching using spin polarization in low-temperature-grown multiple quantum wells”, Appl. Phys. Lett. 77, 2958 (2000).

79. I. Rumyantsev, N. H. Kwong, R. Binder, E. J. Gansen and A. L. Smirl, "$\chi^{(3)}$ analysis of all-optical polarization switching in semiconductor quantum wells", Phys. Rev. B 69, 235329 (2004).

80. K.K. Law, J. Maserjian, R.J. Simes, L.A. Coldren, A.C. Gossard, J.L. Merz, "Optically controlled reflection modulator using GaAs-AlGaAs n-i-p-i/multiple-quantum-well structures," Opt. Lett. 14, 230 (1989).

81. A. Larsson, J. Maserjian, "Optically addressed asymmetric Fabry-Perot modulator," Appl. Phys. Lett. 59, 3099 (1991).

82. P.F. Davies, C.C Phillips, C. Roberts, "All-optical reflection modulator using a nonlinear hetero-n-i-p-i structure within asymmetric Fabry-Perot optical cavity," Appl. Phys. Lett. 74, 3717 (1999).

83. M.B. Yairi, C.W. Coldren, D.A.B. Miller, J.S. Harris, "High-speed, optically controlled surface normal optical switch based on diffusive conduction," Appl. Phys. Lett. 75, 597 (1999).

84. D.S. Chemla, D.A.B. Miller, "Room-temperature excitonic nonlinear- optical effects in semiconductor quantum-well structures." J. of the Opt. Soc. of Amer. B 2, 1155 (1985).

85. M. Combescot and R. Combescot, "Excitonic Stark Shift: A Coupling to "Semivirtual" Biexcitons," Phys. Rev. Lett. 61, 117 (1988).

86. M. Combescot and R. Combescot, "Optical Stark effect of the exciton: Biexcitonic origin of the shift," Phys. Rev. B 40, 3788 (1989).

87. E.J. Gansen, "All-Optical Polarization Switching Techniques Based on the Coherent Many-Body Interactions and the Virtual Excitation of Spin-Polarized Carriers in Semiconductor Quantum Wells," Thesis adviser A.L. Smirl, U. Of Iowa (2004).

88. R. S. Britton, T. Grevatt, A. Malinowski, R. T. Harley, P. Perozzo, A. R. Cameron, and A. Miller, "Room temperature spin relaxation in GaAs/AlGaAs multiple quantum wells," Appl. Phys. Lett. 73, 2140 (1998).

89. A. Malinowski, R. S. Britton, T. Grevatt, R. T. Harley, D. A. Ritchie, and M. Y. Simmons, "Spin relaxation in $GaAs/Al_xGa_{1-x}As$ quantum wells," Phys. Rev. B 62, 13034 (2000).

90. N. Aközbek and S. John, "Self-induced transparency solitary waves in a doped nonlinear photonic band gap material," Phys. Rev. E 58, 3876 (1998).

91. S. John and M. Florescu, “Photonic bandgap materials: towards an all-optical micro-transistor,” J. Opt. A: Pure Appl. Opt. 3, S103 (2001).

92. A. Kozhekin and G. Kurizki, “Self-Induced Transparency in Bragg Reflectors: Gap Solitons near Absorption Resonances,” Phys. Rev. Lett. 74, 5020 (1995)

93. A.Kozhekin and G. Kurizki, “Standing and Moving Gap Solitons in Resonantly Absorbing Gratings,” Phys. Rev. Lett. 81, 3647 (1998).

94. M. F. Yanik, W. Suh, Z. Wang, and S. Fan, “Stopping Light in a Waveguide with an All-Optical Analog of Electromagnetically Induced Transparency”, Phys. Rev. Lett. 93, 233903 (2004).

95. P. Chak, P. E. Sipe, and S. Pereira, “Depositing light in a photonic stop gap by use of Kerr nonlinear microresonators,” Opt. Lett. 28, 1966 (2003).

96. W. N. Xiao, J. Y. Zhou, and J. P. Prineas, “Storage of ultrashort optical pulses in a resonantly absorbing Bragg reflector”, Opt. Express 11, 3277 (2003).

97. J. P. Prineas, W. J. Johnston, M. Yildirim, J. Zhao, and Arthur L. Smirl “Tunable slow light in Bragg-spaced quantum wells”, Applied Physics Letters, 89, 241106, 2006.

98. P. Chak, S. Pereira, and J.E. Sipe, “Coupled-mode theory for periodic side-coupled microcavity and photonic crystal structures”, Phys. Rev. B 73, 035105 (2006).

99. K. P. O'Donnell and X. Chen, “Temperature dependence of semiconductor band Gaps”, App. Phys. Lett. 58, 2924 (1991).

100. M.B. Panish, and H.C. Casey, Jr. , ”Temperature dependence of the energy gap in GaAs and GaP”, Jour. of App. Phys. 40, 163 (1969).

101. Charles Kittel, “Introduction to solid state physics,” Wiley (2005).

102. J.M. Luttinger, W. Kohn, “Motion of electron and holes in perturbed periodic fields”, Phys. Rev. **97**, 869 (1955).

103. P. K. Basu, “Theory of optical processes in semiconductors : bulk and microstructures,” Oxford University Press (1997).

104. C. F. Klingshirn, “Semiconductor Optics”, Springer-Verlag, Berlin, New York (1997)